University of Sussex

A new catalogue of XCS sources in the DES-Y3 region and its application to test gravity models using galaxy cluster profiles

Carlos Fernando Vergara-Cervantes

Submitted for the degree of Doctor of Philosophy

University of Sussex

September 2019

Declaration

I hereby declare that this thesis has not been and will not be submitted in whole or in part to another University for the award of any other degree.

Signature:

Carlos Fernando Vergara-Cervantes

UNIVERSITY OF SUSSEX

CARLOS FERNANDO VERGARA-CERVANTES, DOCTOR OF PHILOSOPHY

A NEW CATALOGUE OF XCS SOURCES IN THE DES-Y3 REGION AND ITS APPLICATION TO TEST GRAVITY MODELS USING GALAXY CLUSTER PROFILES

SUMMARY

Galaxy clusters are the largest gravitationally collapsed structures in the Universe. X-ray observations of clusters provide information on dark matter and the structure formation in the Universe over cosmological time. This can be used to constrain cosmological parameters that are complementary to other cosmological probes. Taking advantage of the potential galaxy clusters have, in combination with the most recent astronomical surveys for cluster finding, allows us to produce leading constraints on cosmological models.

The XCSDR2-DESY3 cluster catalogue, a subset of the XMM Cluster Survey (XCS) Data Release 2 within the Dark Energy Survey (DES) Year 3 footprint, constitutes approximately 722 optically-confirmed clusters. Most of these clusters have associated spectroscopic or photometric redshifts, reliable X-ray bolometric luminosities, and X-ray temperatures. The catalogue is split into samples for different research areas; e.g. high redshift clusters for galaxy evolution; clusters with spectroscopic redshifts for scaling relations and cosmology; and high temperature clusters for combined multi-wavelength studies. The aim of building this sample is to lay the groundwork for the next generation of wide-area and deep joint optical and X-ray galaxy cluster datasets.

Since gravity has a central role in galaxy cluster formation, clusters act as astrophysical laboratories to test modified theories of gravity models in the outskirts of galaxy clusters. By comparing X-ray and weak lensing profiles, it is possible to put constrains on such models, particularly those which rely on screening mechanisms or those that postulate an emergent gravity in the outskirts of clusters to substitute dark matter. By combining detected X-ray clusters with weak lensing data from DES, we were able to place constraints on these type of models. The results are found to be consistent with general relativity, i.e. they do not require gravity to be modified, and are in the same level of confidence as previous studies.

Acknowledgements

This thesis is dedicated to my parents who deserve my full admiration and devotion. Their encouragement and reassurance have been invaluable throughout the last four years, and their love has always been there with me, despite the distance.

First of all, I would like to thank my supervisor Prof. Kathy Romer for providing guidance and feedback throughout this research. I also acknowledge the contribution of several people from the XCS collaboration and the University of Portsmouth whose input and advice into this work was really valuable.

I would like to thank all the fantastic people at the University of Sussex, especially some of them whose insight and knowledge of the subject matter, along with their emotional support, steered me through this project. It has been a privilege and a priceless experience for me to share this space and time with such remarkable people. I would also like to thank all the wonderful people I have met in Brighton, who allowed me into their lives and gave me so much love. It has been a unique adventure living in such a marvellous town and get to live many memorable moments. I cannot forget to thank my brother and friends from Mexico for all the unconditional support and long distance chats during these very intense doctoral years.

I would also like to acknowledge the support from the Mexican National Council for Science and Technology (CONACyT) via the Overseas Doctoral Scholarship, Grant No. 480670. Being the first doctoral graduate among the last three generations in my family reminds me how much needs to be done in terms of education and science in our country.

Contents

List of Tables

List of Figures

Chapter 1

Introduction

Galaxy clusters are the largest gravitationally bound objects in the Universe (Voit, 2004). They encode information about the initial conditions, contents, and expansion history of the Universe. For example, their number density as a function of mass and redshift, can be used to constrain cosmological parameters (Allen, Evrard and Mantz, 2011).

The total gas fraction of galaxy clusters is about 16%, with about 13% in the hot intracluster medium (ICM) and 3% in stars in the cluster galaxies, the remaining 84% of the cluster mass is comprised of dark matter (Rosati, Borgani and Norman, 2002). This is illustrated in Figure 1.1 which shows the galaxy cluster MACS J0416.1-2403: in pink is the ICM distribution, in blue the reconstructed dark matter distribution, and in yellow the member galaxies. The gas in the ICM is gathered in the deep gravitational well of the galaxy cluster. The ICM can be observed through its bremsstrahlung X-ray emission (Mushotzky, 1984). The hot gas can also be detected through the distortion of the observations of photons coming from the Cosmic Microwave Background radiation (CMB) (Rephaeli, 2011) as a result of the Sunyaev–Zeldovich (SZ) effect (Sunyaev and Zeldovich, 1970). The relevance of observing galaxy clusters in the X-ray wavelength comes from their centrally concentrated surface-brightness profiles, which provide a good contrast against the various astrophysical and instrumental X-ray backgrounds (Longair, 2007). Also, cluster X-ray emission stretches over several hundreds of kiloparsecs. This means that, even at redshifts of unity and above, clusters can still be resolved by imaging X-ray telescopes as being extended (by comparison over 90% of other types of X-ray sources are point-like).

In this chapter I begin with the description of the main subject of study of this thesis, galaxy clusters, and introduce some of their astrophysical properties in Section 1.1 and the

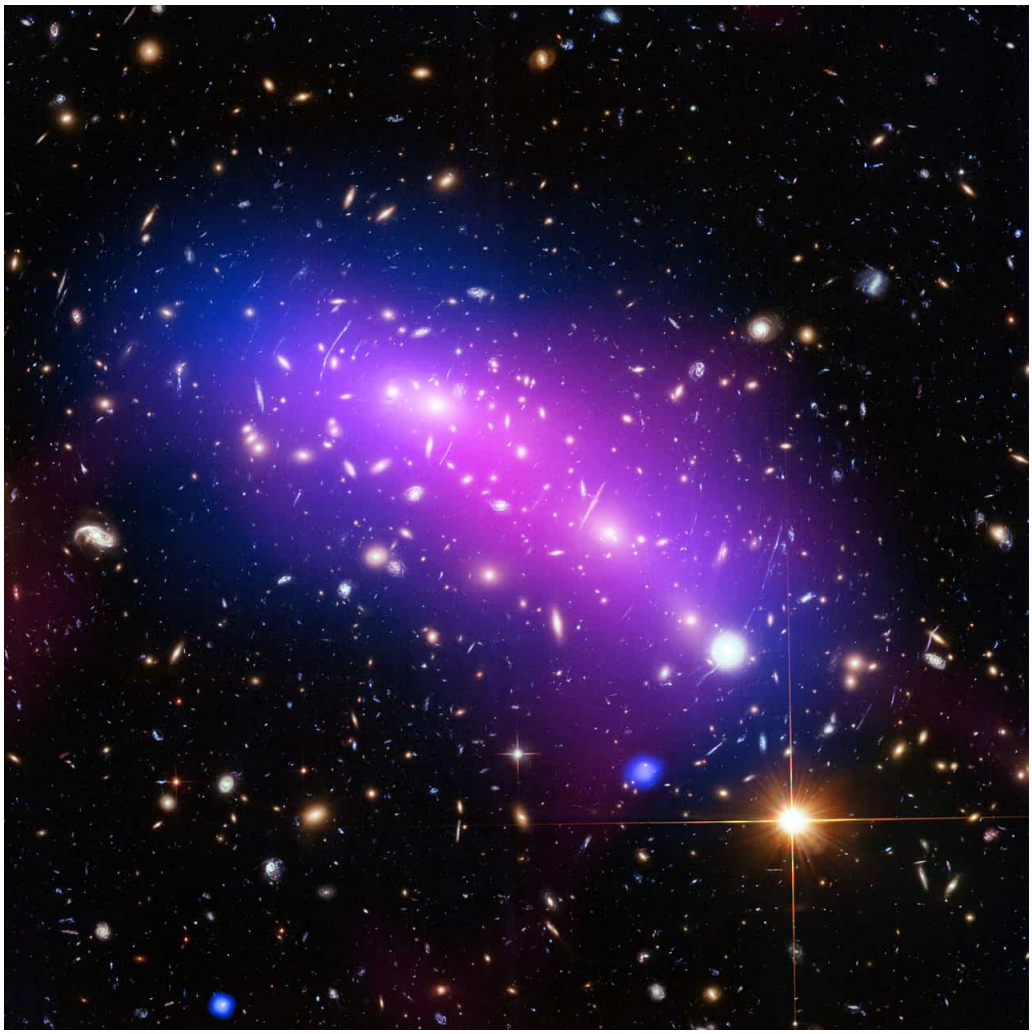

Figure 1.1: The galaxy cluster MACS J0416.1-2403 located at a redshift of $z = 0.397$ with a mass of 1.15×10^{15} solar masses out to a radius of Its mass out to a radius of 950 kpc. This system was discovered during the Massive Cluster Survey, MACS (Ebeling, Edge and Henry, 2001).

scaling relations they follow in Section 1.2. Clusters can be used to study the gravitational lensing, which is described in Section 1.3.1. A description of the basic concepts in General Relativity (GR) and Cosmology is presented in Section 1.4. This includes the observed acceleration expansion of the Universe, and an overview of the current state of cosmology. This chapter closes in Section 1.5 with a review of screening mechanisms within modified theories of gravity and how galaxy clusters can be used to test such type of theories. I focus on a widely used set of models which include a chameleon, $f(R)$, gravity. Throughout this thesis a cosmology with $\Omega_m = 0.27, \Omega_\Lambda = 0.73$, and $H_0 = 70 \mathrm{kms}^{-1}\mathrm{Mpc}^{-1}$ is adopted.

1.1 X-ray emission from galaxy clusters

The ICM emits in the X-rays primarily via thermal bremsstrahlung (or free–free) radiation (Mushotzky, 1984). This emission is produced by the acceleration of electrons in the Coulomb field of protons and atomic nuclei. Since an accelerated electrically charged particle emits radiation, such electron scattering processes result in the emission of photons (Mushotzky, 1984). A high energy photon generated via Bremsstrahlung can be classified depending on its energy as being soft (0.1 keV - 1.0 keV), hard (1.0 keV - 10.0 keV), or a gamma-ray (>1 MeV) (Mushotzky, 1984). The gas temperature in galaxy clusters can be determined from the spectral properties of this radiation. Clusters with a mass between $\sim 10^{13}$ and $\sim 10^{15}$ solar masses corresponds to a mean temperature in the range of $k_B T = 0.5 - 15\text{keV}$. The emissivity, ϵ_ν^{ff}, of bremsstrahlung is described by (Mushotzky, 1984)

$$\epsilon_\nu^{ff} = \frac{32\pi Z^2 e^6 n_e n_i}{3m_e c^3}\sqrt{\frac{2\pi}{3k_B T m_e}} e^{-h\nu/k_B T} g_{ff}(T,\nu), \tag{1.1}$$

where e denotes the elementary charge, n_e and n_i the number density of electrons and ions respectively, Z the charge of the ions, and m_e the electron mass. The function g_{ff} is called the Gaunt factor, and is given by

$$g_{ff} \approx \frac{3}{\sqrt{\pi}} \ln\left(\frac{9k_B T}{4h_p \nu}\right). \tag{1.2}$$

The spectrum described by Equation 1.1 and Equation 1.2 above is flat for $h\nu \ll k_B T$, and exponentially decreasing for $h\nu \geq k_B T$. The total emission for a thermal plasma with Solar abundances is given by

$$\epsilon^{ff} = \int_0^\infty \epsilon_\nu^{ff} d\nu \approx 3.0 \times 10^{-27} \sqrt{\frac{T}{1K}} \left(\frac{n_e}{1\text{cm}^{-3}}\right)^2 \text{erg} \cdot \text{cm}^{-3}\text{s}^{-1}. \tag{1.3}$$

The emission described by Equation 1.3 is $\propto T^{1/2}$, i.e. it decreases with temperature.

It is also clear from Equation 1.3, that the emissivity increases with the square of the plasma density. Therefore, if we want to use the X-ray luminosity to estimate the mass of the hot gas, then we need a model for the spatial distribution of the gas. In regular clusters, density decreases monotonically from the cluster centre. If the cluster is dynamically relaxed, the distribution of the gas can be modelled as an isothermal sphere in hydrostatic equilibrium (Mushotzky, 1984).

The requirement of hydrostatic equilibrium is that, at all points in the system, the attractive gravitational force acting on a mass element ρdV at radial distance r from the centre of the system is balanced by the pressure gradient at that point

$$\frac{1}{\rho_g}\frac{dP}{dr} = -\frac{d\phi}{dr} = -\frac{GM(r)}{r^2}, \tag{1.4}$$

where P denotes the gas pressure, ρ_g the gas density, $M(r)$ is the total mass contained within the radius r (i.e. not just the gas mass), and ϕ is the gravitational potential. Reordering Equation 1.4 and differentiating,

$$\frac{d}{dr}\left(\frac{r^2}{\rho_g}\frac{dP}{dr}\right) = -G\frac{dM(r)}{dr} \quad \Rightarrow \quad \frac{d}{dr}\left(\frac{r^2}{\rho_g}\frac{dP}{dr}\right) + 4\pi G r^2 \rho_g(r) = 0. \tag{1.5}$$

By inserting the equation of state for a perfect gas, $p = nk_BT = \rho_g(r)k_BT/\mu m_p$ into the last equation, the total gravitating mass within r, $M(r)$, can be expressed as

$$M(r) = -\frac{k_B r^2}{G\mu m_p \rho_g}\left(\rho_g\frac{dT}{dr} + T\frac{d\rho_g}{dr}\right) = -\frac{k_B r^2 T}{G\mu m_p}\left(\frac{d\ln\rho_g}{dr} + \frac{d\ln T}{dr}\right). \tag{1.6}$$

Thus, by measuring $T(r)$ and $\rho_g(r)$ (and their gradients), we can derive the total mass, i.e. including baryons and dark matter, $M(r)$ (Voit, 2004; Tozzi, 2007; Allen, Evrard and Mantz, 2011). These measurements are not easy to make though, $\rho_g(r)$ and $T(r)$ need to be determined from the X-ray luminosity and the spectral temperature using the bremsstrahlung emissivity given by Equation 1.1. They can be observed in the form of surface brightness at a projected radius R from the centre of the cluster

$$S_\nu(R) = \frac{1}{2\pi}\int_R^\infty \frac{\epsilon_\nu(r) r}{\sqrt{r^2 - R^2}} dr, \tag{1.7}$$

from which the emissivity, ϵ_ν (Eq. 1.1), and thus the density and the temperature, need to be derived by de-projection. From the radial profile of $S_\nu(r)$, the emissivity can be derived by inverting the last equation (Ettori, 2000)

$$\epsilon_\nu(r) = \frac{4}{r}\frac{d}{dr}\int_r^\infty \frac{S_\nu(R) R}{\sqrt{R^2 - r^2}} dR. \tag{1.8}$$

Since the spectral bremsstrahlung emissivity depends weakly on T for $h P\nu \ll k_BT$ (see Sec. 1.1), the radial profile of the gas density $\rho_g(r)$ can be derived from $\epsilon(r)$. Assuming that the gas temperature is constant within the same volume, so that $T(r) = T_g$ is an isothermal

gas distribution, Equation 1.6 simplifies (since $d \ln T_g / dr = 0$) and the mass profile of the cluster can be determined from the density profile of the gas only.

Taking the emissitivity from Equation 1.3 as

$$\epsilon_\nu = \sum_i n_i n_e \lambda_c(n_i, T_g) \tag{1.9}$$

where $\lambda_c(n_i, T_g)$ is the cooling function, which is a function of the ion and the temperature. The surface brightness can be rewritten by assuming that the gas within the ICM is dominated by hydrogen such that $n_i = n_e$ (Terukina et al., 2014)

$$S_\nu(r) = \frac{1}{4\pi(1+z)^4} \int n_e^2(\sqrt{r^2+z^2}) \lambda_c(T_g) dz, \tag{1.10}$$

where r is the projected distance from the cluster centre and z is the cluster redshift. This equation gives the surface brightness, S_ν, using the temperature and electron density dependent cooling function. The gas within the cluster follows a different profile due to the different physics it is being subjected to, this profile assumes a simple isothermal beta model (Ettori, 2000), while T_g is given by numerical simulations (Burns, Skillman and O'shea, 2010)

$$n_e = n_0 \left(1 + \frac{r}{r_0}\right)^{b_0}, \quad T_g = T_0 \left(1 + A\frac{r}{r_1}\right)^{b_1} \tag{1.11}$$

where n_0, r_0, b_0, T_0, A, r_1, and b_1 are free parameters. Equation 1.10 will be used later in Chapter 4 and Chapter 5 to compare stacked X-ray cluster profiles to a modified theory of gravity model.

1.2 Cluster scaling relations

Scaling relations are power law relations between galaxy cluster properties, such as the X-ray temperature $k_B T_x$, luminosity L_x, richness λ and the total cluster mass, and redshift. These relations provide information about the statistical properties of clusters. They are widely used as an ingredient when constraining cosmological parameters using cluster catalogues. They also tell us about the astrophysics of the cluster formation and evolution (Voit, 2004).

1.2.1 The self-similar model

When a galaxy cluster is described as "self-similar" it is meant that clusters are simply scaled up and down versions of each other (Gladders and Yee, 2000; Kaiser, 1986). Distant clusters are identical to local clusters if the factor for increasing density of Universe with redshift in taken into account. In summary;

- Strong self-similarity suggests that clusters of different masses are identical, scaled versions of each other.
- Weak self similarity means that as long as we account for the changing density of the Universe, a cluster at high redshift is identical to a cluster of the same mass at low redshift.

The self similar model is based on the assuming that

- Clusters form via a single gravitational collapse at z_{obs}.
- The only source of energy input into ICM is gravitational.

With these assumptions, it is possible to predict simple power law relationships between the different properties of galaxy clusters, e.g. (Giodini et al., 2013).

1.2.2 The Mass-Temperature relation

Under the assumption of self-similarity, and hydrostatic equilibrium, it is possible to deduce the existence of relations between cluster properties, e.g. mass, galaxy velocity dispersion, X-ray temperature, X-ray luminosity etc., (Mushotzky, 1984). In a dynamically relaxed galaxy cluster, the gas and galaxies are expected to be virialized

$$2K = -U, \tag{1.12}$$

where K is the kinetic energy and U is the potential energy. The total kinetic energy of the gas, K, can be written in terms of the number of particles, $K \propto nk_BT \propto M_g k_B T$. Which, under the assumption of self-similarity the mass can be re-written as $M_g \propto M_{vir}$, thus, the total mass within r_{vir} is expressed by $K \propto M_{vir} k_B T$. The potential energy of the system is given by $U \propto GM_{vir}^2/r_{vir}$. So the virial theorem can be re-written as

$$2M_{vir}T \propto M_{vir}^2/r_{vir} \quad \Longrightarrow \quad T \propto M_{vir}/r_{vir}. \tag{1.13}$$

The relation above is based on the Virial Theorem, where r_{vir} is chosen to be the radius within which the matter of the cluster is virialized. The virial radius is defined such that within a sphere of radius, the average mass density of the cluster is about $\delta_c \approx 200$ times as high as the critical density of the Universe (see Sec. 1.2.4). The mass within r_{vir} is called the virial mass M_{vir} which is, according to this definition,

$$M_{vir} \equiv M(< r_{vir}) = \frac{4\pi}{3}\delta_c \rho_c r_{vir}^3. \tag{1.14}$$

Combining the two relations, and using the Hubble parameter H (see Sec. 1.4.2), gives

$$T \propto \frac{M_{vir}}{r_{vir}} \propto r_{vir}^2 \propto M_{vir}^{2/3}. \tag{1.15}$$

For a particular overdensity δ_c (see Sec. 1.2.4) the evolution of the dark matter density (and thus the gas) varies with the critical density of the Universe as $\overline{\rho} \propto \overline{\rho}_{DM} = \delta_c \rho_{cr} \propto E(z)^2$, where $E(z)$ is the energy density (see Sec. 1.4.2), thus

$$T_X \propto M^{2/3} E(z) \tag{1.16}$$

This relation has been tested using observations of galaxy clusters with measured temperature and estimated mass (Mushotzky, 1984; Pacaud et al., 2007; Allen, Evrard and Mantz, 2011; Giodini et al., 2013; Mantz et al., 2014).

1.2.3 The Luminosity-Temperature relation

The total X-ray luminosity that is emitted via bremsstrahlung radiation is proportional to the squared gas density and the gas volume as shown by Equation 1.3, hence it should follow

$$L_X = \int \epsilon_\nu(T_g, n) dV, \tag{1.17}$$

where ϵ_ν is given by Equation 1.9. When the cluster is isothermal and the number density of ions and electrons is proportional to the total density of the cluster, then

$$L_X \propto \rho^2 T_g^{1/2} r_{vir}^3 \propto \rho T_g^{1/2} M_{vir}. \tag{1.18}$$

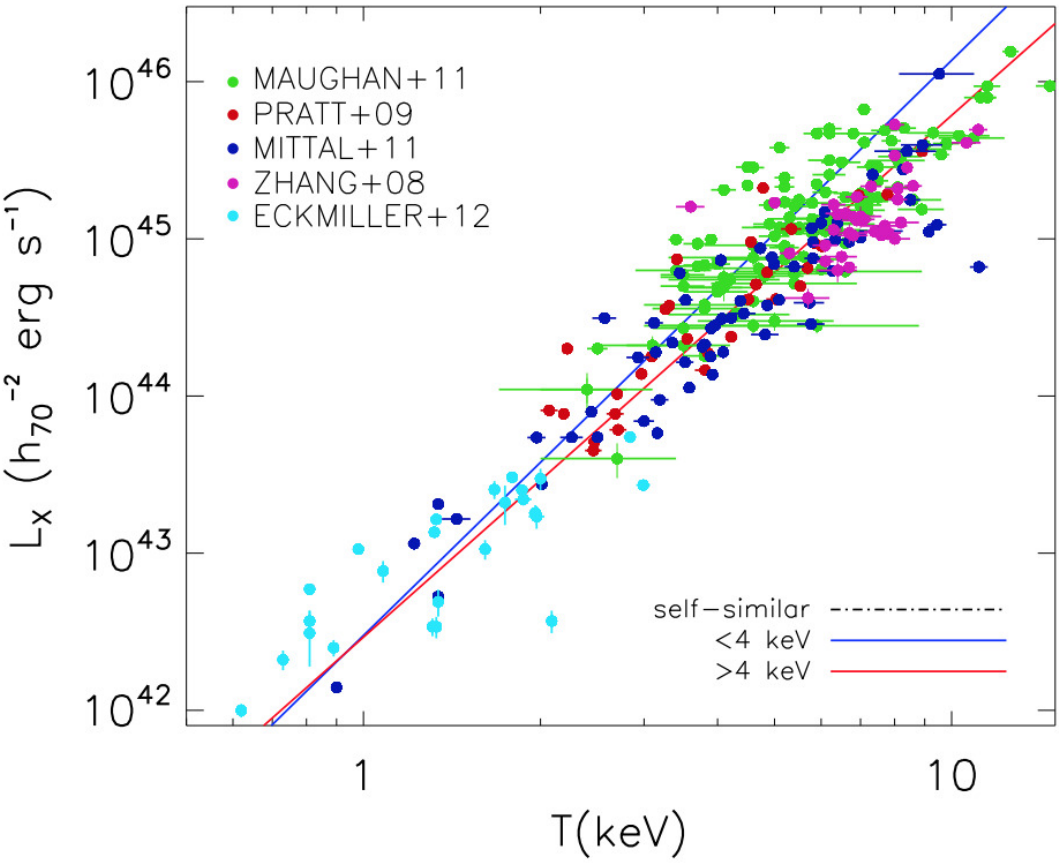

Figure 1.2: Recent measurements of the $L_X - T$ relation for different samples of groups and clusters as shown in (Giodini et al., 2013). Cyan circles mark measurements from the groups sample from (Eckmiller, Hudson and Reiprich, 2011), green circles from (Maughan et al., 2012). Blue circles show the HIFLUGCS massive clusters (Mittal et al., 2011), red circles mark the REXCESS clusters (Pratt et al., 2009) and pink circles are LoCuSS clusters (Zhang et al., 2008). All the parameters are calculated at R_{500}.

Similar to Section 1.2.2, the last equation can be rewritten in terms of the energy density

$$L_X \propto E(z)^2 T_g^{1/2} M_{vir} \propto E^2(z) T_g^2 \tag{1.19}$$

where ρ_{cr} is the critical density and $E(z)$ is the Energy density (see Sec. 1.4.2). There is an additional dependence on temperature in the observed $L_X - T_X$ relation compared with the predicted one. While the self-similar model predicts a scaling relation like the one given by Equation 1.19, observations suggest instead a steeper relation given by $L_X \propto T_X^{(2-3)}$ (Giodini et al., 2013). A possible explanation suggests the cluster can deviate from its equilibrium due to astrophysical processes such as AGN feedback (Gitti, Brighenti and McNamara, 2012).

The luminosity is related to the total mass by using Equation 1.16

$$L_X \propto E^{7/3}(z) M_{vir}^{4/3}. \tag{1.20}$$

The above equation shows the strong correlation between X-ray luminosity and mass in clusters and is used frequently because determining the luminosity (in a fixed energy range) is considered simple. However, in this thesis, the preferred method to measure the mass of a cluster will be when the temperature of the core is excised, since it favors the estimation of scaling relations. This method will be used broadly in Chapter 3 to study Equation 1.19. A compilation of different data for the correlation between temperature and luminosity is shown in Figure 1.2 as an example.

1.2.4 The Mass at different density contrasts

Numerical investigations have indicated the existence of a universal density profile for dark matter halos that results from the collapse of density fluctuations. Inside the virial radius (see Sec. 1.2.2), the Navarro, Frenk, and White (NFW) (Julio Navarro, 1995) profile appears to be a very good approximation of the radial mass distribution. Therefore, a dark matter halo can be described as a spherical region within which the average density is ~ 200 times the critical density (see Sec. 1.4.2) at the respective redshift, the mass M of the halo is related to its radius, r_{200}, by

$$M_{200} = \frac{4\pi}{3} 200 r_{200}^3 \rho_{cr}. \tag{1.21}$$

Since the critical density at redshift z is specified by $\rho_{cr}(z) = 3H_0^2(z)/(8\pi G)$ (see Sec. 1.4.2), the above equation can be written as

$$M_{200} = \frac{100 r_{200}^3 H^2(z)}{G}, \tag{1.22}$$

so that at each redshift a unique relation exists between the halo mass and its radius. A galaxy cluster mass profile averaged over a spherical shell is well described by the NFW profile (Julio Navarro, 1995)

$$\rho(r) = \frac{\rho_s}{(r/r_s)(1 + r/r_s)^2}, \tag{1.23}$$

where ρ_s is the amplitude of the density profile, usually referred as the overdensity (also written as $\delta_c = \rho_{cr}\rho_s$), and r_s specifies a characteristic radius. For $r \ll r_s$ we find $\rho \propto r^{-1}$, whereas for $r \gg r_s$, the profile follows $\rho \propto r^{-3}$. Therefore, r_s is the radius at which the slope of the density profile changes. ρ_s can be expressed in terms of r_s, since, according to the definition of r_{200},

$$\bar{\rho} = 200\rho_{cr}(z) = \frac{3}{4\pi r_{200}^3} \int_0^{r_{200}} 4\pi r^2 \rho(r) dr = 3\rho_s \int_0^1 \frac{x^2 dx}{cx(1 + cx)^2}. \tag{1.24}$$

Where in the last step the integration variable was changed to $x = r_{200}/r_s$, and the concentration index, $c \equiv r_{200}/r_s$, was introduced. The larger the value of c, the more strongly the mass is concentrated towards the inner regions will be. The last equation implies that ρ_s can be expressed in terms of $\rho_{cr}(z)$ and c, and performing the integration yields

$$\rho_s = \frac{200}{3}\rho_{cr}(z) \frac{c^3}{\ln(1 + c) - c/(1 + c)}. \tag{1.25}$$

Thus, for a given cosmology, the NFW profile is completely characterized by its mass, M, and its concentration index, c, or equivalently by r_s and ρ_s

$$r_s = \frac{1}{c} \left(\frac{3M_{200}}{4\pi\rho_s} \right)^{1/3} \tag{1.26}$$

The apparent generality of the NFW profile has been confirmed independently by a number of studies, for instance by Thomas et al. (1998), Bartelmann (1996) and Lewis1 et al. (1999) among others. However, there are a few controversial claims that the NFW prescription may fail at very small radii (Ghigna et al., 1998; Moore B et al., 1998). With the assumption of a NFW dark matter density profile of clusters, it is possible to derive an approximate, but

analytic, solution for the radial profile in modified gravity, more specifically, screening mechanisms, as it will be covered later in Section 1.5.

1.3 Galaxy clusters as gravitational lenses

As light travels from distant galaxies to Earth, it gets deflected by the gravitational field of mass concentrations along its path, distorting the observed light distribution of galaxies. Gravitational lensing is a powerful method that provides information about the mass distribution in clusters without assuming hydrostatic equilibrium (Rosati, Borgani and Norman, 2002). What follows below is a general outline of the main physical concepts of gravitational lensing by extended objects such as galaxy clusters, the derivations from (Schneider, Kochanek and Wambsganss, 2006; Bartelmann, 2010) were followed among others. These concepts, in combination with the theory in Section 1.5, will be used later Chapter 4 and Chapter 5 to derive the mass distribution in clusters to constrain gravity models.

1.3.1 Lensing by extended bbjects

The simplest lensing model of galaxy clusters is to approach them as a collection of point masses. This generalisation considers the deflection as an effect of all the mass within the lens. If the lens is considered compact compared with both, the distance to the lens, D_L, and the distance in between the lens and the source, D_{LS}, then the deflection depends only on the surface density $\Sigma(x)$ of the lens. In general, if $\mathbf{b}$ specifies the the light ray's closest approach to the cluster's centre, integrating over the cluster surface gives the deflection α written in terms of the lensing potential ψ

$$\alpha(\mathbf{b}) \equiv \nabla\psi(\mathbf{b}), \quad \text{where} \quad \psi(\mathbf{b}) = \frac{4G}{c^2}\int \Sigma(\mathbf{b'}) \ln|\mathbf{b} - \mathbf{b'}| dS' \tag{1.27}$$

For the case where the surface density depends on the projected distance R from the centre, the bending of a ray passing at radius b then depends only on the mass $M(< b)$ projected within that circle. By integrating Equation 1.27 over the cluster surface, the deflection vector α is related to the Newtonian prediction as

$$\alpha(b) = \frac{2}{c^2}\int_0^b \nabla\psi dl = \frac{4G}{bc^2}\int_0^b \Sigma(R) 2\pi R dR = \frac{4G}{c_0^2}\frac{M(< b)}{b}. \tag{1.28}$$

The above equation can be used to write the lens equation, which allows the mapping from the source plane to the image plane and ray-traces to reconstruct unlensed images from lensed ones (Schneider, Kochanek and Wambsganss, 2006). In terms of the critical surface mass density, Σ_{cr} (Wambsganss, 1998), the lens equation is given by

$$\beta = \theta \left[1 - \frac{1}{\Sigma_{cr}} \frac{M(< b)}{\pi b^2} \right], \quad \text{with} \quad \Sigma_{cr} \equiv \frac{c_0^2}{4\pi G} \left(\frac{D_S}{D_L D_{LS}} \right). \tag{1.29}$$

The quantity $M(< b)/(\pi b^2)$ is the average surface density within the radius b and D_S is the distance to the source. The significance of the critical surface density can be noted when rewriting it in terms of the critical cosmological density (given by Eq. 1.47)

$$\Sigma_{cr} \equiv \rho_{cr} \frac{c_0^2}{H_0^2} \left(\frac{D_S}{D_L D_{LS}} \right). \tag{1.30}$$

The radial dependence of the surface mass density of a spherically symmetric lens such as an NFW lens (see Sec. 1.2.4) is obtained by integrating the three dimensional density profile along the line of sight

$$\overline{\Sigma}(R) \equiv 2 \int \rho(R, z) dz, \tag{1.31}$$

with $R = d_A(\theta_1^2 + \theta_2^3)^{1/2}$ the projected radius relative to the centre of the lens.

1.3.2 The weak gravitational lens Effect

When the gravitational distortion is very small, stretching tangentially the surface brightness profile by an order of a few percent or less, it is referred to as Weak Gravitational Lensing (Schneider, Kochanek and Wambsganss, 2006). Weak lensing provides a powerful statistical tool for studying the distribution of mass in the Universe. However, in order to reach its full potential as a probe of dark matter and dark energy, the shear measurements must be extremely accurate (Wright and Brainerd, 1999). The shape noise due to the small ellipticities constitutes the primary statistical uncertainty for weak lensing measurements (Kneib and Natarajan, 2012). Nevertheless, by measuring the shapes of millions of galaxies, weak lensing surveys can expect to make precise measurements of the mean shear with fractional statistical uncertainties as low as 1%. Future surveys may reach 0.1%. This implies that systematic errors (i.e. biases) in the shape measurements need to be controlled at a level approximately 3 orders of magnitude smaller than the shape noise on each measurement.

The most direct way to measure weak lensing is to measure the ellipticity of distant galaxies. The effect of the intermediate gravitational fields on the light from a source is to shear it, coherently stretching the galaxies in a region in the same direction. The magnitude of this effect on a single galaxy is only a few percent, which is much smaller than either the intrinsic scatter in galaxy shapes or the atmospheric and optical image distortion. The intrinsic scatter means the requirement of large surveys to obtain as much statistical power as possible. The atmospheric and optical effects implies the necessity of careful optical design and precision modelling of the induced distortions. More information can be found in (Kneib and Natarajan, 2012; Schneider, Kochanek and Wambsganss, 2006; Oguri and Takada, 2011).

Weak lensing by galaxy clusters

The shear due to a galaxy cluster is computed directly from the coherent distortion pattern that it induces in the images of distant source galaxies (Bartelmann, 2010). In the realistic observational limit of weak shear and a finite number of lensed images, a measurement of the mean shear inside a radius x centered on the centre of mass of the lens is more easily determined than the differential radial dependence of the shear. Since the NFW density profile is spherically symmetric, the expression to fit a weak lensing shear profile inside a radius x can be written using Equation 1.25 and Equation 1.31, see full details in (Wright and Brainerd, 1999),

$$\gamma_{NFW}(x) = \begin{cases} ((r_s \delta_{cr} \rho_{cr})/\Sigma_{cr}) g_<(x) & x < 1, \\ ((r_s \delta_{cr} \rho_{cr})/\Sigma_{cr}) \left(10/3 + 4\ln(1/2)\right) & x = 1, \\ ((r_s \delta_{cr} \rho_{cr})/\Sigma_{cr}) g_>(x) & x > 1, \end{cases} \tag{1.32}$$

where $r_s = r_{200}/c$ is the scale radius (see Sec. 1.2.4) and the functions $g_<$ and $g_>$ depend only on the dimensionless radius x and are independent of the cosmology, as defined also in (Wright and Brainerd, 1999),

$$\begin{aligned} g_<(x) = & \frac{8\text{arctanh}\sqrt{(1-x)(1+x)}}{x^2\sqrt{1-x^2}} + \frac{4}{x^2}\ln\left(\frac{x}{2}\right) \\ & - \frac{2}{(x^2-1)} + \frac{4\text{arctanh},\sqrt{(x-1)(x+1)}}{(x^2-1)(1-x^2)^{1/2}} \end{aligned} \tag{1.33}$$

$$g_>(x) = \frac{8\arctan\sqrt{(x-1)(x+1)}}{x^2\sqrt{x^2-1}} + \frac{4}{x^2}\ln\left(\frac{x}{2}\right) - \frac{2}{(x^2-1)}, + \frac{4\arctan\sqrt{(x-1)(x+1)}}{(x^2-1)^{3/2}} \tag{1.34}$$

Employing the shear method for weak lensing relies on the shape measurements of faint galaxy images; where the noise due to the intrinsic ellipticity dispersion (σ_ϵ) is $\propto \sigma_\epsilon/\sqrt{n}$, therefore, requiring a high number density n. However, in order to increase the number density of galaxies it is necessary to observe to fainter magnitudes.

Equation 1.32 describes the shape of the main dark matter halo and the baryons associated with it. This profile is commonly known as the 1-halo term, as it arises from the presence of a single halo. However clusters are not isolated from the Universe, forming at the meeting points of filaments. This correlated matter can lead to a modification of the cluster profile known as the 2-halo term (Oguri and Hamana, 2011). The tangential shear profile due to the 2-halo term is given by

$$\gamma_{t,2h}(\theta; M, z) = \int \frac{l}{2\pi} J_2(l\theta) \frac{\bar{\rho}_m(z) b_h(M; z)}{(1+z)^3 \Sigma_{cr} d_A^2(z)} P_m(k_l; z) dl, \tag{1.35}$$

where $\bar{\rho}_m$ is the mass density, d_A the angular diameter distance (see Sec. 1.4.4), b_h is the halo bias, Σ_{cr} is the critical mass density (1.31), P_m is the linear power spectrum, $k_l \equiv l/((1+z) + D_A(z))$, and J_2 is the second order Bessel function. The total shear profile of the cluster is then given by the sum of Equation 1.32 and Equation 1.35, i.e.

$$\gamma = \gamma_{t,2h} + \gamma_{NFW} \tag{1.36}$$

Subsequently, the tangential shear, γ_t, and cross shear, γ_x can be calculated as a function of their position relative to the cluster position using the angle ϕ between the cluster's X-ray centroid and the galaxy from a baseline of zero declination using the following set of equations (Hoekstra, 2013).

$$\begin{aligned} \gamma_t &= -(\gamma_1 \cos(2\phi) + \gamma_2 \sin(2\phi)), \\ \gamma_x &= -\gamma_1 \sin(2\phi) + \gamma_2 \cos(2\phi). \end{aligned} \tag{1.37}$$

The tangential shear is a measure of the orientation of the lensed ellipticity of a source galaxy that is exactly tangential to the centre of the lensing mass. The relevance of the tangential

shear is because such quantity corresponds to a measurement of the lensing signal. On the other side, the cross shear is defined at 45 degrees to the tangential shear. A cluster can only be a perfect lens if it produces a tangential signal in the shear exclusively. Therefore, the cross shear should average out to zero around a given point, making it useful to estimate the noise on the measurement of the tangential shear. Equation 1.32 and Equation 1.37 will be used in Chapter 4 and Chapter 5 to test stacked lensing cluster profiles and to compare them to a modified theory of gravity model.

1.4 Basic concepts of general relativity and cosmology

Gravitation is the fundamental force in the Universe. Only gravitational forces and electromagnetic forces can act over large distances. Since cosmic matter is electrically neutral on average, electromagnetic forces do not play any significant role on large scales, so that gravity is considered to be the driving force in the Universe (Weinberg et al., 2013). The laws of gravity are described by the theory of General Relativity (GR) (Einstein, 1916). It contains Newton's theory of gravitation as a special case for weak gravitational fields and small spatial scales, which correctly describes the major aspects of a relativistic cosmology, although it is not complete on its own.

1.4.1 The Einstein field equations

The only way to preserve the homogeneity and isotropy of space and yet incorporate time evolution is to allow the curvature scale, characterized by a, to be dependent on time. In GR, there is no absolute time, and spatial distances are not invariant with respect to coordinate transformations. Instead, the infinitesimal spacetime interval between events is invariant. Following the derivation found in (Mukhanov, 2005), the interval takes the form

$$ds^2 = dt^2 - dl^2 = dt^2 - a^2(t)\left(\frac{dr^2}{1-kr^2} + r^2 d\Omega^2\right) \equiv g_{\alpha\beta} dx^\alpha dx^\beta, \tag{1.38}$$

where $g_{\alpha\beta}$ is the metric of spacetime and $x^\alpha \equiv (t, r, \theta, \phi)$ are the coordinate system. Equation 1.38 is called the *Friedmann-Lemaitre-Robertson-Walker* metric. These spatial coordinates are comoving; which means that every object with zero peculiar velocity has constant coordinates r, θ, ϕ. The time coordinate t is the proper time measured by a comoving observer, with the distance between two comoving observers at a particular time given by

$$\int \sqrt{-ds^2_{t=const}} \propto a(t), \tag{1.39}$$

which increases or decreases in proportion to the scale factor. In GR, the dynamical variables characterizing the gravitational field are the components of the metric $g_{\alpha\beta}(x^\gamma)$ and they follow the Einstein equations

$$G^\alpha_\beta \equiv R^\alpha_\beta - \frac{1}{2}\delta^\alpha_\beta R - \Lambda\delta^\alpha_\beta = 8\pi G T^\alpha_\beta, \tag{1.40}$$

where the symbol δ^α_β denotes the unit tensor, it takes the value of 1 when $\alpha = \beta$ and 0 otherwise; $R = R^\alpha_\alpha$ is the scalar curvature, and $\Lambda =$ const. is the cosmological term. Also, the Ricci tensor, which describes the local curvature of space-time is given by

$$R^\alpha_\beta = g^{\alpha\gamma}\left(\frac{\partial\Gamma^\delta_{\gamma\beta}}{\partial x^\delta} - \frac{\partial\Gamma^\delta_{\gamma\beta}}{\partial x^\beta} + \Gamma^\delta_{\gamma\beta}\Gamma^\sigma_{\delta\sigma} - \Gamma^\sigma_{\gamma\delta}\Gamma^\delta_{\beta\sigma}\right), \tag{1.41}$$

which is expressed in terms of the inverse metric $g^{\alpha\gamma}$ defined via $g^{\alpha\gamma}g_{\gamma\beta} = \delta^\alpha_\beta$, and the Chrystoffel symbols

$$\Gamma^\alpha_\beta = \frac{1}{2}g^{\alpha\delta}\left(\frac{\partial g_{\gamma\delta}}{\partial x^\beta} + \frac{\partial g_{\delta\beta}}{\partial x^\gamma} - \frac{\partial g_{\gamma\beta}}{\partial x^\delta}\right). \tag{1.42}$$

Matter is incorporated in Einstein's equations through the energy– momentum tensor

$$T^\alpha_\beta = (\rho + p)u^\alpha u_\beta - p\delta^\alpha_\beta. \tag{1.43}$$

where matter can be approximated as a perfect fluid characterized by energy density on large scales. In Equation 1.43, the equation of state $p = p(\rho)$ depends on the properties of matter and must be specified. For example, if the Universe is composed of ultra-relativistic gas, the equation of state is $p = \rho/3$. In many cosmologically interesting cases $p = w\rho$, where w is constant. From this, the conservation of energy and momentum is determined by the condition that the equations

$$\frac{\partial T_{\alpha\beta}}{\partial x^\beta} = 0. \tag{1.44}$$

1.4.2 The Friedmann equations

The relativistic equations of cosmological evolution are obtained by substituting the metric (Eq. 1.38) and energy–momentum tensor (Eq. 1.43) into the Einstein equations (Eq. 1.40). The

resulting equations are called the Friedmann equations (Friedmann, 1922) and they determine the two unknown functions: $a = a(t)$ and $\rho = \rho(t)$. The most important of the two is the acceleration equation, known as the Friedmann equation, which describes the accelerated expansion of the Universe

$$\ddot{a} = -\frac{4\pi G}{3}(\rho + 3p)a + \frac{\Lambda}{3}. \tag{1.45}$$

The equation above can be rewritten in terms of the Hubble parameter, $H = H(t)$, which is used to describe the rate of change of the scale factor, $H(t) = \dot{a}/a$, and measures the expansion rate, with the overdot denoting a time derivative. By multiplying Equation 1.45 by $\dot{a}$, using $\dot{\rho} = -3H(\rho + p)$ to express p in terms of ρ and H, and integrating, the second Friedmann equation is obtained

$$H^2 + \frac{k}{a^2} = \frac{8\pi G}{3}\rho + \frac{\Lambda}{3}, \tag{1.46}$$

with Λ the cosmological constant. The Einstein equations (Eq. 1.40) tell us that the constant k in Equation 1.46 is exactly the curvature introduced in Equation 1.38, that is, $k = \pm 1$ or 0. For $k = \pm 1$, the magnitude of the scale factor a has a geometrical interpretation as the radius of curvature. Thus, in GR, the value of the cosmological parameter $\Omega = \rho/\rho_{cr}$ determines the geometry of the Universe. Figure 1.3 shows the dynamics of of the classical Friedmann models with $\Omega_\Lambda = 0$ characterized by the density parameter; if $\Omega > 1$, the Universe is closed and has the geometry of a three-dimensional sphere $(k = +1)$, where the matter content is enough to halt and recollapse; $\Omega = 1$ corresponds to a flat universe $(k = 0)$; and in the case of $\Omega < 1$, the Universe is open and has hyperbolic geometry $(k = -1)$, where there is no enough matter to stop the expansion. The combination of Equation 1.46 and either the conservation law for $\dot{\rho}$ or the acceleration equation (Eq. 1.45), supplemented by the equation of state $p = p(\rho)$, forms a complete system of equations that determines the two unknown functions a and ρ. The solutions depend not only on the geometry but also on the equation of state. The current critical density for the case of a flat Universe can be inferred from Equation 1.46

$$\rho_{cr} = \frac{3H_0^2}{8\pi G} = 1.88 \times 10^{-29} h^2 \mathrm{g/cm^3}, \tag{1.47}$$

where h is the Hubble constant in units of $100 \mathrm{kms^{-1}Mpc^{-1}}$, with the best current measure-

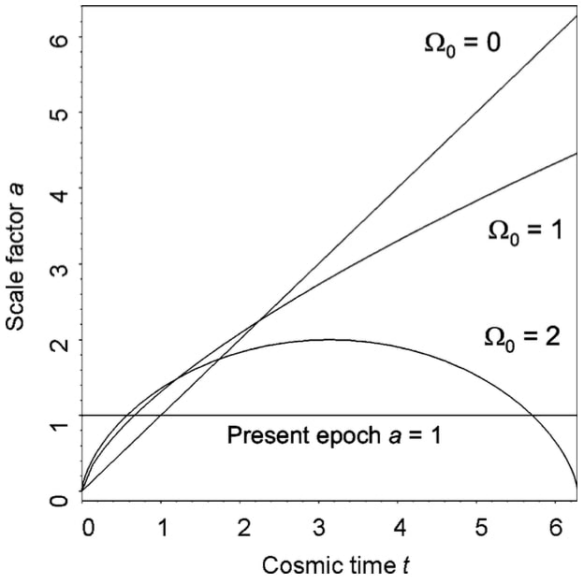

Figure 1.3: The dynamics of the classical Friedman models with $\Omega_\Lambda = 0$ characterised by the density parameter $\Omega_0 = \rho_0/\rho_{cr}$. If $\Omega_0 > 1$, the Universe collapses to $a = 0$; if $\Omega_0 < 1$, the Universe expands to infinity and has a finite velocity of expansion as a tends to infinity. In the case $\Omega_0 = 1, a = (t/t_0)^{2/3}$ where $t_0 = (2/3)H^{-1}$. The time axis is given in 0 terms of the dimensionless time $H_0 t$. At the present epoch $a = 1$ and in this presentation, the three curves have the same slope of 1 at $a = 1$, corresponding to a fixed value of Hubble's constant at the present day. If t_0 is the present age of the Universe, then $H_0 t_0 = 1$ for $\Omega_0 = 0, H_0 t_0 = 2/3$ for $\Omega_0 = 1$ and $H_0 t_0 = 0.57$ for $\Omega_0 = 2$. Image taken from (Longair, 2007).

ments suggesting $h = 0.678 \pm 0.009$ (Ade et al., 2016).

The dimensionless density parameters for matter, radiation, and vacuum are defined by

$$\Omega_m = \frac{\rho_m}{\rho_{cr}}, \quad \Omega_r = \frac{\rho_r}{\rho_{cr}}, \quad \Omega_\Lambda = \frac{\rho_V}{\rho_{cr}}, \tag{1.48}$$

so that $\Omega_{Tot} = \Omega_m + \Omega_r + \Omega_\Lambda$ is the total energy density. These quantities allow us to write an expression for the expansion rate of the Universe (Eq. 1.46) as a function of its constituents

$$H^2 = H_0^2 \left(a^{-4}\Omega_r + a^{-3}\Omega_m - a^{-2}\frac{k}{H_0^2} + \Omega_\Lambda \right). \tag{1.49}$$

Evaluating this equation at the present epoch, with $H(t_0) = H_0$ and $a(t_0) = 1$, yields the value of the constant $k = H_0^2(\Omega_m + \Omega_\Lambda - 1)$. Finally, the expansion equation becomes

$$H^2 = H_0^2 \left(a^{-4}\Omega_r + a^{-3}\Omega_m - a^{-2}(1 - \Omega_m - \Omega_\Lambda) + \Omega_\Lambda \right). \tag{1.50}$$

Assuming an energy density of that of a LCDM Universe and by defining $E(z) = H(z)/H_0$ and $\Omega_k = 1 - \Omega_m - \Omega_\Lambda$, Equation 1.50 can be rewritten as

$$E^2(z) = \Omega_m(1+z)^3 + \Omega_k(1+z)^2 + \Omega_\Lambda. \tag{1.51}$$

The exponents of each term in Equation 1.50 indicate how each component affects the expansion rate as time goes by. For a very small value of a, the first term in Equation 1.50 stands out and the Universe is dominated by radiation. For a slightly larger $a > a_{eq}$, the matter term dominates. If $k \neq 0$, the third term, dominates for larger values of a. For very large a, the cosmological constant dominates as long as it is different from zero. Measurements of the angular peaks of the CMB suggest a spatially flat Universe. The results from the Planck Collaboration on cosmological parameters have measured a value of $|\Omega_k| < 0.005$. This implies that the total density of the Universe has a value of $\Omega = 1$ (Ade et al., 2016). Additional observations from the baryon acoustic oscillations, type Ia Supernovae, and the large scale distribution of galaxies have constrained the total matter density in the Universe to $\Omega_m \approx 0.3$ (see Sec. 1.4.5).

1.4.3 The cosmological redshift

The cosmological redshift is the shift of spectral lines to longer wavelengths associated with the isotropic expansion of the system of galaxies. If λ_e is the wavelength of the emitted line and λ_0 is the observed wavelength, the redshift z is defined as

$$z = \frac{\lambda_0 - \lambda_e}{\lambda_e} = \frac{\lambda_0}{\lambda_e} - 1. \tag{1.52}$$

Consider a wave packet with wavelength λ_e emitted at the time t_e from a distant source, and received by an observer at the present epoch at time t_0. The signal propagates along null cones, $ds^2 = 0$, and so, considering radial propagation from source to observer (i.e. $d\theta = 0$ and $d\phi = 0$), from the metric given by Equation 1.38

$$dt = -\frac{a(t)}{c} dr \quad \Rightarrow \quad \int_{t_e}^{t_0} \frac{cdt}{a(t)} = -\int_r^0 dr, \tag{1.53}$$

with $a(t)dr$ the interval of proper distance at cosmic time t. Integrating the last equation leads to the expression

$$\frac{dt_0}{a(t_0)} = \frac{dt_e}{a(t_e)}. \tag{1.54}$$

This is the cosmological expression for the phenomenon of time dilation and also provides an equation for the redshift. If $\Delta t_e = \nu_e^{-1}$ is the period of the emitted waves and $\Delta t_0 = \nu_0^{-1}$ the oberved period, then $\nu_0 = \nu_e a(t_e)$ which in terms of the redshift z is

$$1 + z = \frac{\nu_e}{\nu_o} = \frac{a(t_0)}{a(t_e)} \tag{1.55}$$

Therefore, the redshift is a measure of the scale factor of the Universe when radiation was emitted by a source.

1.4.4 Distances in cosmology

Two ways to measure the distance to a distant extragalactic object from astronomical observations are, the luminosity distance d_L and the angular diameter distance d_A. These measures are the apparent distances that an object appears to have based on its luminosity/size at a specific moment of cosmological time. Both distances are dependent on the underlying cosmology of the Universe. For an object of size D its observable properties are the angular size θ subtended by the object with a measured flux, F, and known intrinsic luminosity, L,

$$d_A = \frac{D}{\theta}, \qquad d_L = \left(\frac{L}{4\pi F}\right)^{1/2}. \tag{1.56}$$

An expression for d_A in a Robertson–Walker metric can be obtained from the value of the proper size D, given by the integral of dl in Equation 1.38 over the transverse direction

$$D = \int a(t_e) r(z) d\theta = \frac{a(t_0) r(z)}{1+z}\theta, \tag{1.57}$$

where $r(z)$ is the proper distance to the object at redshift z. It then follows from Equation 1.55 and Equation 1.56

$$d_A = \frac{a(t_0) r(z)}{1+z} = a(t_e) r(z). \tag{1.58}$$

To get an expression for dL, if A is the proper area that subtends a solid angle, ω, at the object. By definition of the angular-diameter distance d_A, such a solid angle corresponds to a proper area ωd_A^2 at the position of the object. For a non-static Universe, the proper area subtended by a fixed solid angle at a given object is stretched by a factor of $a^2(t)$, so $A = \omega d_A^2 (a(t_0)/a(t_e))^2 = (a(t_0) r(z))^2 \omega$. Then the flux F is

$$F = \frac{\omega}{4\pi}\frac{L}{A}\left(\frac{a(t_e)}{a(t_0)}\right)^2 = \frac{L}{4\pi (a(t_0) r(z)(1+z))^2}. \tag{1.59}$$

With this last equation the luminosity distance, d_L, defined in Equation 1.56 can be rewritten as

$$d_L = a(t_0)r(z)(1+z). \tag{1.60}$$

The distance measures described above are relevant when making cosmological inferences from observations of galaxy clusters. Being able to observe the flux, angular size and luminosity precisely, allows to make constraints on the cosmological models arising from the calculated luminosity/angular diameter distance. The angular diameter distance given by Equation 1.58 will be used repeatedly to crossmatch different cluster samples in Chapter 3.

1.4.5 Cosmological probes

There exist several pieces of observational evidence which indicate that the Universe is currently undergoing a period of accelerated expansion (Weinberg et al., 2013). Several methods can be used to measure cosmological parameters and quantify the presence of dark energy in the cosmos (Frieman, Turner and Huterer, 2008).

- **Type 1a Supernovae** (SN Ia) are very likely to be the explosions of white dwarfs in binary systems after exceeding their mass limit as a result of the accretion of mass from the companion star. Since the initial conditions are probably very homogeneous across all SN Ia, their luminosity peak is approximately the same. Therefore, SN Ia are standardisable candles. With the use of SN Ia, cosmological parameters can be constrained by comparing distances to low and high redshift, to study the presence of Dark Energy and measure its properties (Howell, 2011).

- **Baryon Acoustic Oscillations** (BAO) are the imprints left by sound waves in the early Universe which result in a feature of known size in the late time clustering of matter and galaxies. The early Universe consisted of a concentration of primordial plasma caught between gravity and radiation pressure, which exhibits an oscillatory behaviour. By measuring this acoustic scale at different redshifts, one can infer $d_A(z)$ and $H(z)$ and probe the cosmic expansion (Dalton, 2009).

- The **Cosmic Microwave Background** (CMB) provides an image of the Universe at epoch of recombination, i.e. $z \approx 1,100$. At that time, Dark Energy contributed only a small part of the total energy density.) The CMB anisotropy spectrum has been measured to high precision and can be accurately predicted for a given cosmological model.

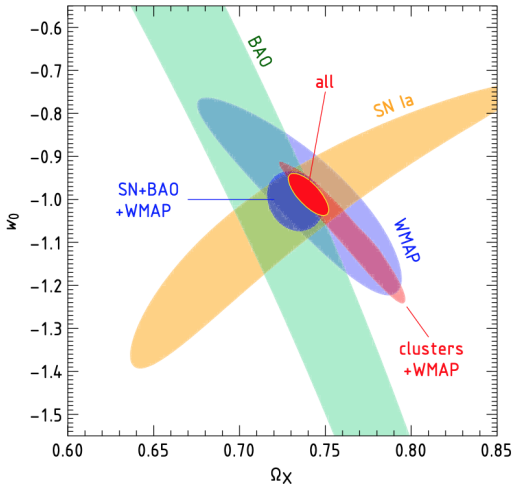

Figure 1.4: Constraints on cosmological parameters combining various cosmic probes as found in (Vikhlinin et al., 2009). Individual probes cannot constrain all parameters, for example, as seen above, BAO analysis is not informative about the value of w_0, and using SN Ia does not strongly constrain w_0 (marked as Ω_λ in this figure). However, combining several methods leads to the much tighter constraints given by the red field marked *all*.

The CMB plays a critical supporting role by determining other cosmological parameters, such as the spatial curvature and matter density to high precision (Hu, 2002). Recent studies from the Planck satellite (Ade et al., 2016) have put tight constraints on a range of cosmological parameters that are all consistent with the Standard Model of Cosmology.

Cosmological constraints from galaxy clusters

Because galaxy clusters are the largest collapsed objects in the Universe, there are various methods by which cosmological parameters can be determined from their observations. Cosmology with clusters can be brought down to two key tests: calculating the gas mass fraction and counting the number of clusters as a function of their mass over redshift.

- **Cluster Counts and Clustering**. A method sensitive to the growth of structure formation, cosmological model, and dark energy equation of state is to measure the number of galaxy clusters expected to be seen as a function of their mass and redshift (Allen, Evrard and Mantz, 2011). The cluster mass function describes the number of clusters with a given mass inside a unit of comoving volume which corresponds to a density. Assuming galaxy clusters formed via spherical collapse of matter around large peaks in the density field, the abundance of clusters will depend on properties of structure formation. This in turn affects the cosmological parameter values derived from these assumptions.

The halo number density can be compared to the model predictions using X-rays cluster catalogues (Allen, Evrard and Mantz, 2011). In order to perform this comparison, the masses of clusters need to be determined from Equation 1.20. For a given survey, the expected number of clusters $N_{a,i}$ within a mass bin a and redshift bin i can be characterized as

$$N_{a,i} = \frac{\Delta\omega_i}{4\pi} \int_{z_i}^{z_{i+1}} dz \frac{dV}{dz} \int_{M_a}^{\ln M_{a+i}} d\ln M \frac{dN}{d\ln M} \tag{1.61}$$

where ω is the solid angle and the cosmology information is included through the mass function and the volume element dV/dz. In order to apply this approach to constrain cosmology, the equation above needs to be corrected to add information from redshift uncertainties and possible counting errors from incompleteness and impurities on the survey. The comparison of the number density of observed clusters to the halo density in cosmological models as a function of redshift, constraints the amplitude of linear density perturbations at $z \approx 0$, usually expressed in terms of the σ_8 parameter (the normalization of the power spectrum) for a given matter density parameter. With sufficiently small statistical and systematic errors in the σ_8 measurement, the ratio of σ_8 and the amplitude of the CMB fluctuations power spectrum provides a measure of the total growth of perturbations between $z \approx 1000$ and $z = 0$, a powerful dark energy constraint (Vikhlinin et al., 2009). For a more complete review, also see Mantz et al. (2010), Mantz et al. (2014) and Costanzi et al. (2018)

- **The Gas Mass Fraction**. Studies have shown that the baryon content of galaxy clusters does not seem to vary from cluster to cluster but to have a uniform value. Therefore the existence of a common observed baryon fraction is to be expected (Chernin et al., 2012). Assuming the baryon fraction, f_b, in clusters to be representative of the Universe, the density parameter of the Universe can be determined since the cosmic baryon density is known from primordial nucleosynthesis. If $n_b(M_b)$ is the baryonic mass function and $n(M)$ the total mass function according to (White et al., 1993) is

$$n_b(M_b) = n\left(\frac{\Omega_m}{\Omega_b} M_b\right) = n\left(\frac{M_b}{f_b}\right) \approx 0.3. \tag{1.62}$$

Once $n_b(M_b)$ and Ω_b are known from observations, the total mass function can be computed as a function of Ω_m, thereby treated as a fitting parameter. Studies (Voevodkin

and Vikhlinin, 2003) that have applied this method have found $\sigma_8 = 0.72 \pm 0.04$ with $\Omega_m h = 0.13 \pm 0.07$. Other analysis of a set of clusters observed with Chandra to obtain constraints on parameters such as Ω_m and Ω_Λ, found a matter density $\Omega_m = 0.27 \pm 0.04$, and dark energy density of $\Omega_\Lambda = 0.65 \pm 0.17$. (Vikhlinin et al., 2003).

Each of the methods summarized in Section 1.4.5 exhibit various strengths and weaknesses, constraining some cosmological parameters better than others. However, by combining the results from multiple probes some information can be drawn about the nature of expansion of the Universe more precisely than without any one method. Figure 1.4 shows recent measurements of cosmological parameters through the combination of several probes, as depicted in Vikhlinin et al. (2009). More detailed reviews of observational cosmology include Weinberg et al. (2013) and Huterer and Shafer (2018).

1.4.6 The success of the Standard Model of Cosmology

The Standard Model of Cosmology assumes GR as the theory to describe gravity on all scales. Over the last century experimental tests of this theory have been proven successful. The cosmic expansion equations together with the energy density equation described in Section 1.4.2 imply a number of consequences which makes the Standard Model of Cosmology extremely successful in several ways (Cervantes-Cota and Smoot, 2011), broadly

- It predicts a helium content of $\sim$ 25% by mass of metal-poor gas in agreement with observations.
- It predicts that objects at lower redshift are closer to us than objects at higher redshifts.
- It predicts the existence of the CMB, which has been already discovered.
- It predicts the correct number of neutrino families, which was confirmed in laboratory experiments.

Despite these achievements, the late time acceleration of the Universe may require the revision (Joyce et al., 2015) of the theory of gravity on cosmological scales and the standard model of cosmology based on GR (see Sec. 1.5). Astronomical surveys are improving the measurements of cosmic expansion and of the large scale structure of the Universe, providing the opportunity to test gravity on astrophysical and cosmological scales.

1.5 Basic concepts of modified gravity

One explanation for the observed cosmic acceleration is new physics within the gravitational theory itself. There has been significant progress in developing modified gravity theories that act as an alternative to dark energy (Koyama, 2016). However, one of the main challenges for modifying gravity models is to satisfy local measurements, such as on Solar System scales, that closely match the predictions of GR. Screening mechanisms have therefore been developed to hide modifications to GR gravity on small scales, whilst allowing the possibility that there are such modifications on larger scales.

1.5.1 Screening mechanisms

An accepted approach to modify GR's field equations (Eq. 1.40) is to add a component to the energy-momentum tensor via dark energy or to the Einstein tensor by modifying gravity (Jain et al., 2013). The second option usually involves coupling a scalar field to the matter components of the Universe, giving rise to a fifth force (Khoury and Weltman, 2004). This force, if it exists, must be negligible at Solar System scales, therefore it is required to be suppressed (or screened). The chameleon gravity model (Khoury and Weltman, 2004) postulates the existence of a fifth force, which would influence the hot X-ray gas filling the potential wells of galaxy clusters. However, the weak lensing signal from the cluster would remain unaffected. Therefore, by comparing X-ray and weak lensing profiles, it is possible to place upper limits on the strength of such force. The impact of modified theories of gravity on clusters will be covered in Section 1.5.3.

The field equation of the chameleon field ϕ is given by (Khoury and Weltman, 2004)

$$\nabla^2\phi = \frac{\partial V}{\partial \phi} + \frac{\beta}{M_{Pl}}\rho \exp\left(\beta\phi/M_{Pl}\right), \tag{1.63}$$

where ρ is the matter density, V is the scalar field potential, β is the coupling between the scalar field and matter when it is not screened, and $M_{Pl} \equiv (8\pi G)^{-1/2}$ is the Planck mass. In this case, the potential is assumed to be a simple monotonic function of the scalar field, in the above equation the dynamics of the chameleon are not governed by the $V(\phi)$ but by the effective potential

$$V_{eff} \equiv V(\phi) + \rho \exp\left(\beta\phi/M_{Pl}\right) \tag{1.64}$$

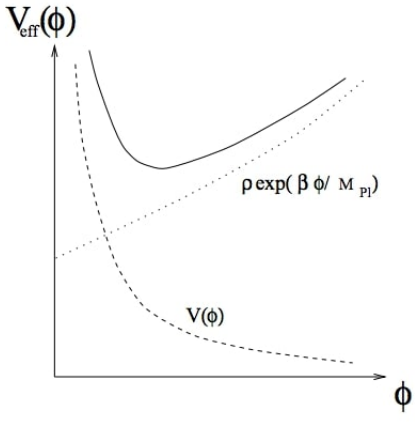

Figure 1.5: The chameleon effective potential V_{eff} (solid curve), as seen in (Khoury and Weltman, 2004), is the sum of the scalar potential $V(\phi)$ (dashed curve) and a density dependent term (dotted curve)

with V_{eff} having a minimum if $\beta > 0$. The value of ϕ at the minimum as shown in Figure 1.5, ϕ_{min}, and the mass of small fluctuations about the minimum, m_{min}, both depend on ρ. More precisely, ϕ_{min} and m_{min} are decreasing and increasing functions of ρ, respectively. That is, the larger the density of the environment, the larger the mass of the chameleon.

The chameleon fifth force, derived from the chameleon field, is

$$F_\phi = -\frac{\beta}{M_{Pl}}\nabla\phi. \tag{1.65}$$

In the model, the baryonic and dark matter are coupled to the chameleon field. Therefore, both matter components are subject to the gravitational force and the chameleon force F_ϕ.

1.5.2 $f(r)$ models

A modification to gravity which can exhibit the chameleon screening is the $f(R)$ gravity (Sotiriou and Faraoni, 2010). These type of models are generalised forms of GR, where the Ricci scalar in the Einstein–Hilbert action is replaced by an arbitrary function of the Ricci scalar in the gravitational part of the action. The action Einstein-Hilbert action is given by

$$S = \int d^4x\sqrt{-g}\left[\frac{R + f(R)}{2\kappa^2} + L_m\right] \tag{1.66}$$

where R is the Ricci scalar, $\kappa^2 \equiv 8\pi G$, and L_m is the matter Lagrangian. Note that the constant f is equivalent to the cosmological constant that takes account of the expansion of the Universe. The Einstein equations (Eq. 1.40) are derived from this action by setting to zero with respect to the metric (Buchdahl, 1970)

$$G_{\alpha\beta} + f_R R_{\alpha\beta} - \left(\frac{f}{2} - \partial^{\alpha}\partial_{\alpha} f_R\right) g_{\alpha\beta} - \nabla_{\alpha}\nabla_{\beta} f_R = 8\pi G T_{\alpha\beta}, \tag{1.67}$$

above $G_{\alpha\beta}$ is the Einstein tensor and $f_R \equiv df/dR$. In order for models to be compatible with observational constraints it is required that $|f_R| \ll 1$. The time derivatives can be neglected in the above equation for small scales in a quasi-static approximation as done by (Oyaizu, 2008). Together, the field equation is simplified as

$$\nabla^2 f_R = (1/3)(\delta R - 8\pi G \delta\rho), \tag{1.68}$$

where δR and $\delta\rho$ denote the perturbations in the scalar and matter density respectively. By applying the Newtonian limit to Equation (1.67), a modified Poisson equation for the gravitational potential is obtained as in (Hu and Sawicki, 2007)

$$\nabla^2\phi = \frac{16\pi G}{3}\delta\rho - \frac{1}{6}\delta R. \tag{1.69}$$

The last two sets of partial differential equations need to be solved in order to follow cosmic structure formation. However, it is necessary for $f(R)$ to satisfy certain observational properties first. The cosmology should reproduce that of the standard model in the high-redshift regime. It should take into account the accelerated expansion at low redshift. There should be enough degrees of freedom in the parametrization to cover a range of low-redshift phenomena. It should include as a limiting case the phenomenology of the standard model. All of these concerns can be satisfied by the following conditions (Hu and Sawicki, 2007)

$$\lim_{R\to\infty} f(R) = \text{const.}, \qquad \lim_{R\to 0} f(R) = 0. \tag{1.70}$$

These conditions are satisfied by the class of models that exhibit a chameleon mechanism

$$f(R) = -m^2 \frac{c_1 (R/m^2)^n}{c_2 (R/m^2)^n + 1}, \tag{1.71}$$

with $n > 0$ is the scaling index that modulates the scalar field amplitude, and c_1 and c_2 are integration constants, and the mass scale

$$m^2 \equiv \frac{\kappa^2\bar{\rho}}{3} = (8315 Mpc)^{-2}\left(\frac{\Omega_m h^2}{0.13}\right), \tag{1.72}$$

the sign of $f(R)$ is also defined as $d^2f/dR^2 > 0$ for $R \ll m^2$. Equation 1.71 is free from a cosmological constant. However when the value m^2 is comparable with that of the curvature R, $f(R)$ may be expanded as

$$\lim_{(m^2/R)\to 0} f(R) \approx -\frac{c_1}{c_2}m^2 + \frac{c_1}{c_2^2}m^2\left(\frac{m^2}{R}\right)^n. \tag{1.73}$$

In the equation above, the term c_1/c_2 accounts for the cosmological constant in the limit $c_1/c_2 \to 0$. Furthermore, for finite values of c_1/c_2^2 the curvature has a fixed value and stops decreasing with the matter density, reproducing the accelerating property of the standard model.

The approximation of the expansion history with a cosmological constant $\tilde{\Omega}_\Lambda$ and matter density $\tilde{\Omega}_m$ with respect to a critical value is given by setting

$$\frac{c_1}{c_2} \approx 6\frac{\tilde{\Omega}_\Lambda}{\tilde{\Omega}_m}. \tag{1.74}$$

Larger values of n reproduces the standard model until the late expansion history while a smaller value of c_1/c_2^2 resembles it more accurately. Since the critical density and Hubble parameter depend on the f_R modification, $\tilde{\Omega}_m$ is only the true value in the limit when $c_1/c_2^2 \to 0$ then $\tilde{\Omega}_m = \Omega_m$.

For the flat standard model expansion history

$$R \approx 3m^2\left(a^{-3} + 4\frac{\tilde{\Omega}_\Lambda}{\tilde{\Omega}_m}\right), \tag{1.75}$$

and the field equation is given by

$$f_R = -n\left(\frac{c_1}{c_2^2}\right)\left(\frac{m^2}{R}\right)^{n+1}, \tag{1.76}$$

In $f(R)$ models, the fifth force is mediated by an additional degree of freedom called a scalaron, characterised by $f_R = df/dR$, where the value at the current epoch is f_{R0}. $f(R)$ gravity can be related to the effectiveness of the screening mechanism, ϕ_∞ (Eq. 1.81), via the equation found in (Joyce et al., 2015)

$$f_R(z) = -\sqrt{\frac{2}{3}}\frac{\phi_\infty}{M_{Pl}}. \tag{1.77}$$

Solar System tests require a value of $|f_{R0}| < 10^{-6}$ (Hu and Sawicki, 2007). While for dwarf galaxies, which are unscreened due to their low masses, demands $|f_{R0}| < 4 \times 10^{-7}$ at the

scale of kiloparsec (Jain, Vikram and Sakstein, 2012). CMB measurements at the scale of megaparsec contraints are of the order of $|f_{R0}| < 10^{-3}$ (Raveri et al., 2014), while using cluster abundance constraints are $|f_{R0}| < 2.6 \times 10^{-5}$ (Cataneo et al., 2014). This work aims to tighten the constraints on $|f_{R0}|$ using clusters at the scale of megaparsec in Chapter 4 and Chapter 5. Where the fifth force would be screened in the dense cluster core but not in the outskirts.

1.5.3 Impact of modified theories of gravity on clusters

An analytical solution of the chameleon field given by Equation 1.65 can be derived by assuming a NFW profile (see Sec. 1.2.4) of a galaxy cluster in hydrostatic equilibrium. The analytic solution (Terukina et al., 2014) is given by connecting the interior solution ϕ_{int} and the outer solution ϕ_{ext}. The interior solution is obtained when the scalar field is at the minimum of the effective potential V_{eff}, which corresponds to $\nabla^2\phi = 0$ in the chameleon field equation (Eq. 1.63), then

$$\phi_{int} \equiv \phi_s \left(\frac{r}{r_s}\right)\left(1+\frac{r}{r_s}\right)^2 \quad \text{for} \quad (r < r_c), \tag{1.78}$$

which represents the regime where the chameleon field is suppressed and the fifth force is not being considered. On the other hand, the outer solution is obtained when the contribution of the scalar field potential in Equation 1.63 is dominated by the matter density so $\nabla^2\phi \gg \partial V/\partial\phi$, therefore

$$\phi_{out} \equiv \left(\frac{\beta\rho_s r_s^2}{M_{Pl}}\right)\frac{\ln(1+r/r_s)}{r/r_s} - \frac{C}{r/r_s} + \phi_\infty, \quad \text{for} \quad (r > r_c), \tag{1.79}$$

in this case the chameleon field mediates the fifth-force. However, the matter density is still large compared to the background and the scalar field is not settled in the minimum of the effective potential. For these last equations C is an integration constant, r_c is the transition scale, ρ_s is the overdensity (Eq. 1.25), and $\phi_s = (n\Lambda^{n+4}M_{Pl}/\beta\rho_s)$ represents the value of the chameleon field in the interior region of the cluster and the parameter ϕ_∞, the values of the scalar field at a large distance from the cluster. The integration constant C and the transition scale, r_c, are determined from the conditions $\phi_{int}(r_c) = \phi_{out}(r_c)$ and $\phi'_{int}(r_c) = \phi'_{out}(r_c)$ yielding the approximate solution found in (Terukina et al., 2014)

$$-\frac{\beta\rho_s r_s^2}{M_{Pl}}\ln\left(1+\frac{r_c}{r_s}\right)+\phi_\infty\left(\frac{r_c}{r_s}\right)\simeq C \tag{1.80}$$

$$\phi_\infty-\frac{\beta\rho_s r_s^2}{M_{Pl}}\left(1+\frac{r_c}{r_s}\right)^{-1}\simeq 0 \tag{1.81}$$

The above solutions together with the hydrostatic equilibrium equation (Eq. 1.82) produce an analytic model that can be fit to the X-ray surface brightness profiles of a galaxy cluster. For this approximation, the transition equations above do not depend on the parameters of the scalar field potential, Λ and n, since ϕ_∞ is the degree of freedom of the model, which, depending on the environment of a cluster, may be different from the cosmological background value of the scalar field. In Equation 1.81, the case where the chameleon field is screened, the critical radius r_c is determined by the term $\beta M_{Pl}/\phi_\infty$. This implies that the smaller ϕ_∞ at fixed β, the larger the critical radius becomes. As a consequence, the entire cluster can be screened. The smaller β, the smaller the strength of the fifth force becomes and the Newtonian gravity regime is recovered in each of the limits $\beta=0$ and $\phi_\infty=0$. This makes the coupling of the scalar field to matter, β, and the range of the fifth force, ϕ, key parameters to be probed by astrophysical tests (see (Jain, Vikram and Sakstein, 2012)).

In the presence of the chameleon field, the hydrostatic equilibrium equation (Eq. 1.4) is modified by the introduction of an extra force on the right-hand side of the equation, yielding

$$\frac{1}{\rho(r)}\frac{dP(r)}{dr}=-\frac{GM(r)}{r^2}-\frac{\beta}{M_{Pl}}\frac{d\phi(r)}{dr}. \tag{1.82}$$

Assuming that the equation of state for the gas is given by $P=n_g kT_g$ and integrating

$$P(r)=P_0+\mu m_p\int_0^r n_e(r)\left(-\frac{GM(r)}{r^2}-\frac{\beta}{M_{Pl}}\frac{d\phi(r)}{dr}\right)dr, \tag{1.83}$$

where n_e is given by Equation 1.11, P_0 is the gas pressure at $r=0$, i.e. $P_0=n_{g,0}kT_0$ with $n_{g,0}$, and T_0 being the gas number density and the gas temperature at $r=0$, respectively.

Thus, the chameleon force only modifies the mass inferred from hydrostatic equilibrium

$$M_{total}(<r)=M_{hydro}(r)+M_\phi(r), \tag{1.84}$$

where $M_{hydro}(r)$ is given by Equation 1.6 and the last term is defined as

$$M_\phi(r)\equiv-\frac{r^2}{G}\frac{\beta}{M_{Pl}}\frac{d\phi(r)}{dr}, \tag{1.85}$$

which is the mass associated with the enhanced gravitational force due to the chameleon field.

As discussed in Section 1.1, the mass distribution of a cluster can be determined by its gas density, temperature, and pressure, which can be measured in X-ray observations. This mass distribution, given by Equation 1.6, can be compared directly with the lensing mass. By adopting the Newtonian gauge in GR and assuming for simplicity a spatially flat background, the gravitational lensing is given by (Arnold, Puchwein and Springel, 2014)

$$\phi_L = \frac{\phi + \psi}{2}, \tag{1.86}$$

where ϕ is the modified gravitational potential for the Newtonian approximation (Eq. 1.69), which satisfies the Poisson equation. While ψ is given by

$$\nabla^2 \psi = \frac{8\pi G}{3}\delta\rho + \frac{1}{6}\delta R, \tag{1.87}$$

which helps to understand that

$$\nabla^2 \phi_L = \frac{1}{2}\left(\frac{16\pi G}{3}\delta\rho - \frac{1}{6}\delta R + \frac{8\pi G}{3}\delta\rho + \frac{1}{6}\delta R\right) = 4\pi G\delta\rho = \nabla^2\phi_N, \tag{1.88}$$

this means that $\nabla^2\phi_L$ satisfies the same standard Poisson equation as the Newtonian gravitational potential, $\nabla^2\phi_N$, from GR. This result implies that the deflection angle of light by matter along the line of sight stays unchanged, and so are the weak lensing mass estimates which are not affected by $f(R)$ gravity. Therefore, a method to measure the underlying mass distribution assuming hydrostatic equilibrium is given by

$$M_{hydro} + M_\phi \equiv M_{WL}, \tag{1.89}$$

with M_{WL} the mass recovered from the weak lensing measurement. Assuming that the dark matter component dominates over the baryionic contribution in the cluster and the matter density of the cluster ρ is well described by a NFW profile (see Sec. 1.2.4). The mass of the dark matter within the radius r is then given by solving Equation 1.4

$$M_{WL} = \int_0^r 4\pi r^2 \rho_g(r) dr = 4\pi\rho_s r_s^3 \left(\log(1 + r/r_s) - \frac{r/r_s}{1 + r/r_s}\right), \tag{1.90}$$

with ρ_s and r_s are given by Equation 1.25 and Equation 1.26 respectively.

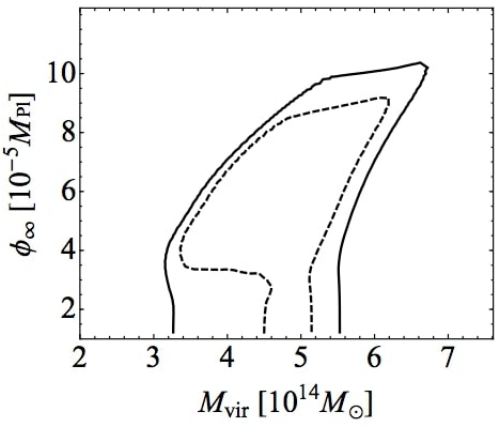

Figure 1.6: The contours of $\Delta\chi^2$ on the parameter plane $\phi_\infty - M_{vir}$, fitting to the temperature profile of the cluster Hydra A with fixed $\beta = 1$. The contour levels of the dashed and solid curves are the 90% and the 99% confidence levels respectively. This figures shows how a useful constraint on a model parameter can be obtained depending on the value of the coupling constant. Image taken from Terukina and Yamamoto (2012).

The hydrostatic equilibrium equation for a gas coupled with the chameleon field was first solved analytically by Terukina and Yamamoto (2012). The authors investigated the influence of the chameleon force on the gas density, temperature, and pressure profiles in a dark matter halo. They found that, due to the addition of the chameleon field, the gas distribution becomes compacted because a larger pressure gradient is necessary. By comparing the theoretical prediction with the temperature profile of the Hydra A cluster, using X-ray observations out to the virial radius, the authors demonstrated the possibility of obtaining a useful constraint on a model parameter depending on the value of the coupling constant. In the case of the upper bound of the background value of chameleon field, a value of $\phi_\infty < 10^{-4} M_{Pl}$ was obtained in the case $\beta = 1$. However, for the case of $\beta = \sqrt{1/6}$, which corresponds to the case of a $f(R)$ gravity, no constraints were obtained. Figure 1.6 from (Terukina and Yamamoto, 2012) shows the likelihood region of the $\phi_\infty - M_{vir}$ plane for the temperature profile of the Hydra A cluster.

1.5.4 Probes of screening mechanisms in clusters

Section 1.5.3 described the effect that $f(R)$ would have on the X-ray surface brightness and weak lensing galaxy cluster profiles. More specifically, the shape the X-ray surface brightness profile, given by Equation 1.10, would have in the presence of the chameleon field depends on Equation 1.82. Without this extra force, the relativistic case would be recovered, using Equation 1.4 instead, when solving Equation 1.10. On the other hand, the equation to measure weak lensing profiles is given by Equation 1.32, which was discussed in Section

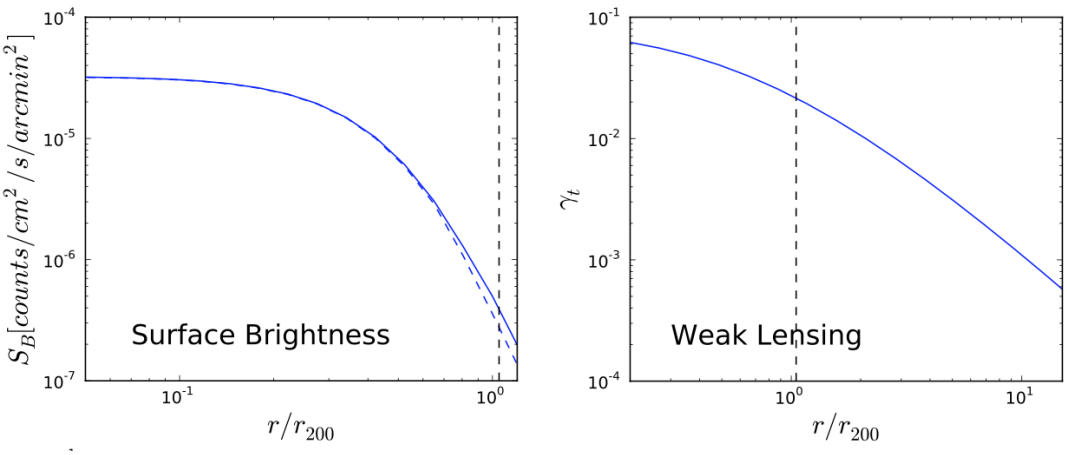

Figure 1.7: The X-ray surface brightness and the weak lensing profiles against radius for the same cluster under the influence of $f(R)$ gravity. In both plots, the solid line is the cluster under GR, while the dotted line is the cluster under the presence of $f(R)$ gravity. In each case the dotted vertical line corresponds to r_c given by Eq. 1.81.

1.3.2. With the use of these profiles it is possible to constrain $f(R)$ gravity, which is shown in Chapter 4 and Chapter 5 with different cluster samples.

Figure 1.7 shows the analytical prediction for these profiles for a galaxy cluster, showing how they behave under GR alone and under the presence of modified gravity. The left plot shows the X-ray surface brightness against radius. The solid blue line is the cluster under the influence of GR, while the dashed blue line corresponds to the cluster under the effect of the chameleon field, as described by Equation 1.82. The image shows that in the presence of the chameleon field, the surface brightness profile is compressed at the outskirts of the cluster. The dashed black vertical line in the figure is r_c given in Equation 1.81. The right plot of Fig. 1.7 shows the weak lensing profile for the same cluster. The solid blue line, for GR, and the dashed blue line, for modified gravity, lie on top of each other in this profile since it is not altered by the chameleon field, as shown by Equation 1.88. Again, the dashed line corresponds to r_c. It is important to notice that the strongest deviations away from the prediction of GR (beyond r_c, where $f(R)$ is no longer screened) occur at or outside r_{200}. This implicates a strong dependence upon the NFW profile.

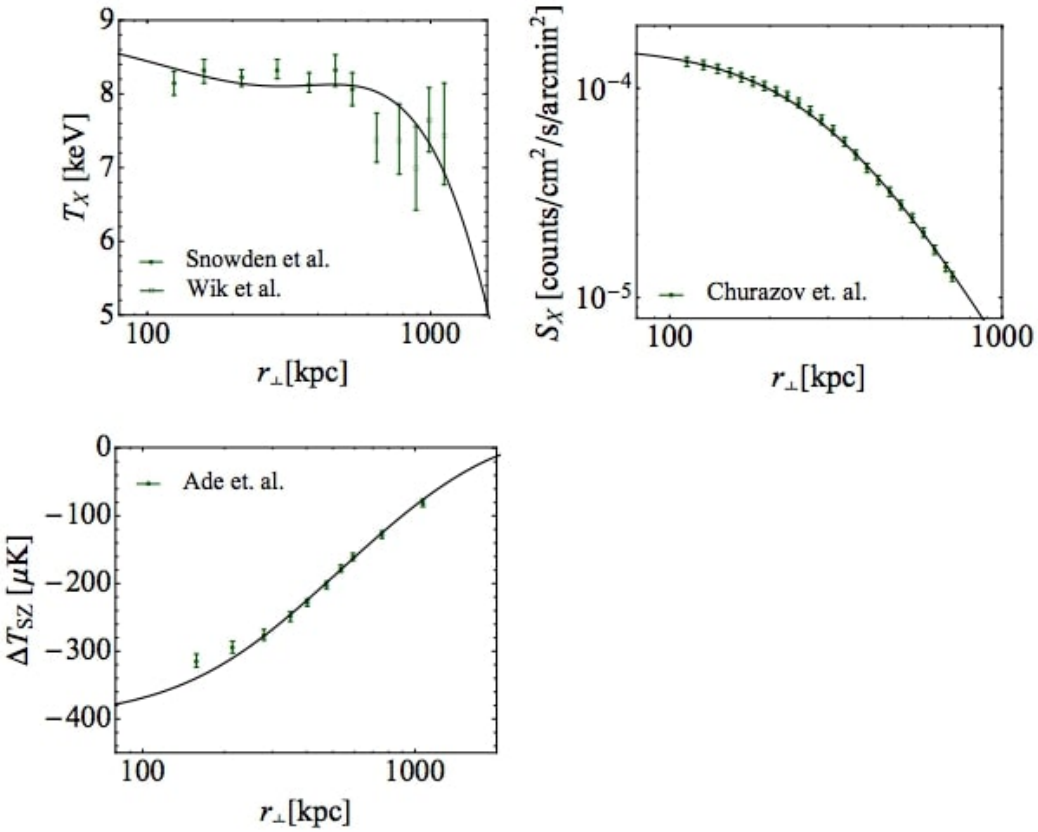

Figure 1.8: X-ray temperature (top-left), surface brightness (top-right), and SZ effect (bottom) profiles for the Coma cluster. The best-fit values of the chameleon model parameters are shown in black. Note that the best-fits of the Newtonian and chameleon cases almost overlap. Figure from (Terukina et al., 2014)

1.5.5 Former uses of this method

Previous works have used the method described in the previous sections using observations to constrain $f(R)$ gravity models in clusters using a combination of X-ray surface brightness, lensing shear, and in some cases using X-ray temperature and SZ profiles as well. After the work in (Terukina and Yamamoto, 2012), Terukina et al. (2014) built these profiles for the Coma cluster (a massive cluster at $z = 0.02$) to perform an MCMC analysis of the parameter space used to describe the cluster profiles in the modified gravity regime under the assumption of hydrostatic equilibrium. In their results they obtained constraints on $f(R)$ models of $|f_{R_0}| < 6 \times 10^{-5}$.

It is known that the Coma cluster is not at hydrostatic equilibrium, i.e. it doesn't have a spherical geometry (Kim Kwang Tae, 1995). Moreover, its low redshift produces a small

weak lensing signal. These aspects motivated Wilcox et al. (2015) to reproduce and apply Terukina et al. (2014) method to a sample of 58 X-ray selected clusters at a redshift range of ($0.1 < z < 1.2$) instead of a single cluster. All clusters were assumed to be in hydrostatic equilibrium, with no significant additional non-thermal pressure affecting their profiles. At the same time the dark matter haloes were described by an NFW profile which works well in chameleon gravity. Stacking the X-ray surface brightness and shear profiles of the cluster sample allowed them to produce a higher signal to noise weak lensing shear profile and an average spherical cluster shape of the whole sample (see Figure 1.9). The X-ray data was taken from the XMM Cluster Survey (XCS) (Romer et al., 2000; Lloyd-Davies et al., 2011) while the weak lensing data came from the Canada France Hawaii Telescope Lensing Survey (Heymans et al., 2012). The results from (Wilcox et al., 2015) set an upper limit on the background field amplitude today of $f(R)$ models of $|f_{R_0}| < 6 \times 10^{-5}$ (95% confidence level) when the value of β is fixed to $\sqrt{1/6}$. Which is in the same level of constraint as (Terukina et al., 2014), demonstrating the effectiveness of the stacking method.

In a following publication Wilcox et al. (2018) tested the methodology and some of the assumptions presented in (Wilcox et al., 2015). These were done with the use of two types of simulations; one using LCDM+GR simulation and a second one including a modified gravity component given by $|f_{R0}| = 10^{-5}$. The simulations presented in (Wilcox et al., 2018) generated accurate stacked X-ray surface brightness and weak lensing profiles. The work demonstrated again that the stacking process created representative, spherically symmetrical profiles, thus reducing a possible bias caused by any ellipticity in an individual cluster. Also, it was shown that dark matter haloes in chameleon gravity are well described by NFW profiles used in LCDM. Finding no difference between the fitted NFW parameters for both $f(R)$ and LCDM simulated stacks, confirmed by previous studies too in (Lubini et al., 2011; Arnold, Puchwein and Springel, 2014), as shown in Figure 1.10. To test the methodology of (Wilcox et al., 2015), the simulations were compared against the analytical predictions. The results show an overall agreement between the analytical and the numerical values, a small deviation from LCDM was found for the same value of $|f_{R0}| = 10^{-5}$. This deviation suggests that the constraints in (Wilcox et al., 2015) were maybe under-estimated and a correction to the analytical model could be determined using the simulations. Finally, the full MCMC analysis from the authors previous work was applied to the simulated X-ray and lensing profiles, which provided consistent constraints on the modified gravity parameters

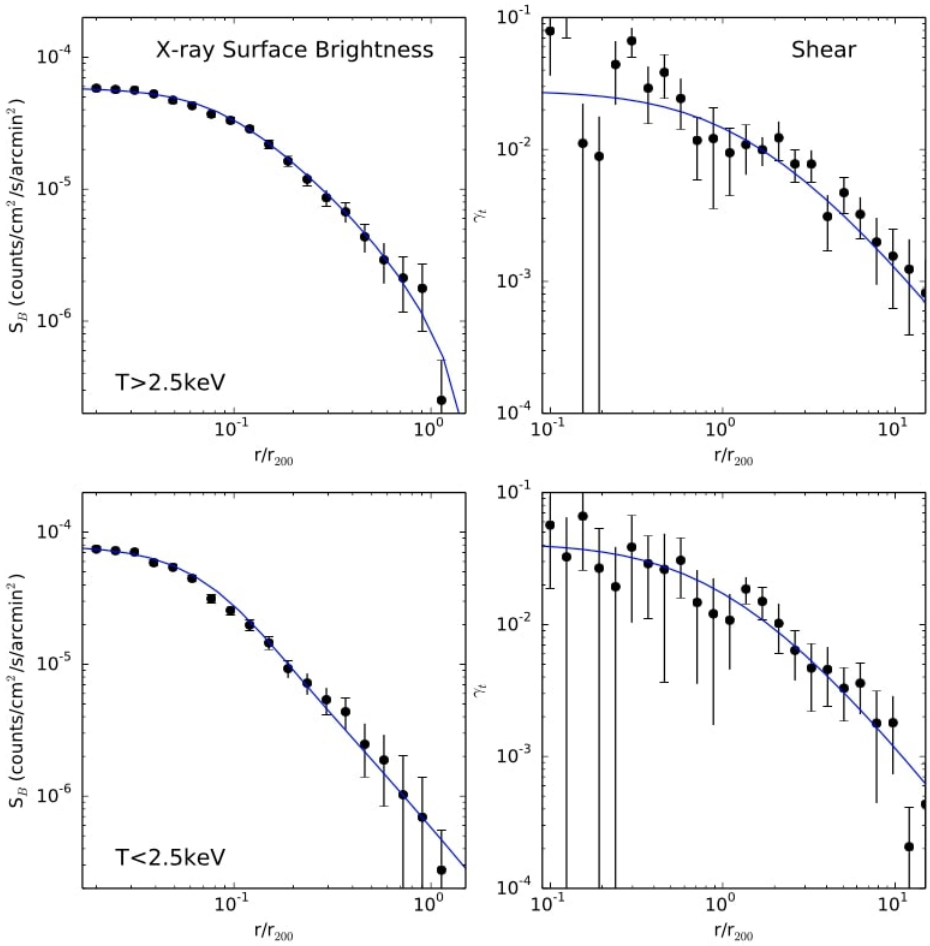

Figure 1.9: X-ray surface brightness profiles (left) and weak lensing (right) for the two bins of X-ray temperature: T < 2.5keV (top) and T > 2.5keV (bottom), against radial distance normalised by r_{200}. Image taken from (Wilcox et al., 2015).

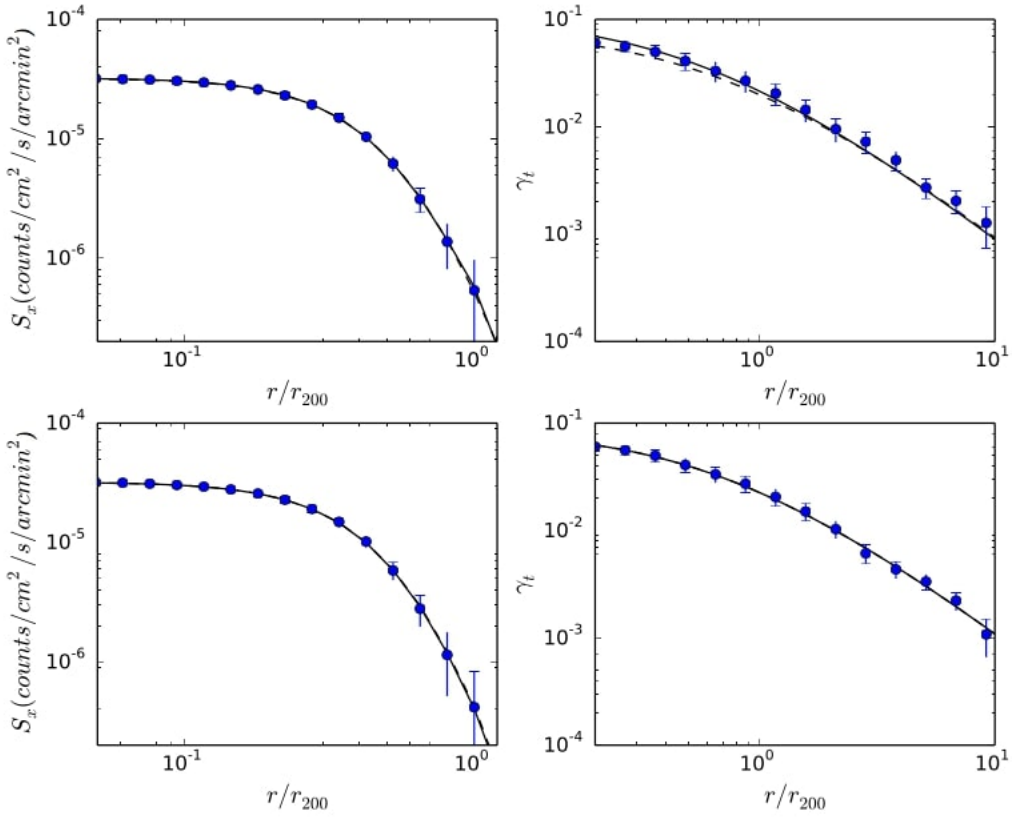

Figure 1.10: The X-ray surface brightness (left) and weak lensing (right) profiles for the two simulations: LCDM+GR (top) and f(R) (bottom). For each profile, the best-fit analytical model with (dashed line), and without (solid line), the additional non-thermal pressure component. Figure taken from (Wilcox et al., 2018)

as those from the sample with observational data from clusters. For the LCDM simulation $|f_{R0}| < 8.3 \times 10^{-5}$ (95% confidence level) which is in agreement with the measurement mentioned above. Overall, these tests confirm the power of the methodology which can now be applied to larger cluster samples available with the latest surveys.

In (Tamosiunas et al., 2019) Verlinde's theory of Emergent Gravity (EG)(Verlinde, 2016) is tested using the same method and data from (Terukina et al., 2014) and (Wilcox et al., 2015) for the Coma cluster and for 58 stacked galaxy clusters . Once more, the X-ray surface brightness profiles and the weak lensing shear profiles were used to test this theory. The authors found that the simultaneous EG fits of both the X-ray and weak lensing profiles are significantly worse than those provided by LCDM+GR as shown in Figure 1.11. For the Coma cluster, the predictions from EG and GR agree within the range of 250 - 700 kpc, however at 1 Mpc scales, EG total mass predictions are larger by a factor of 2. In the case of

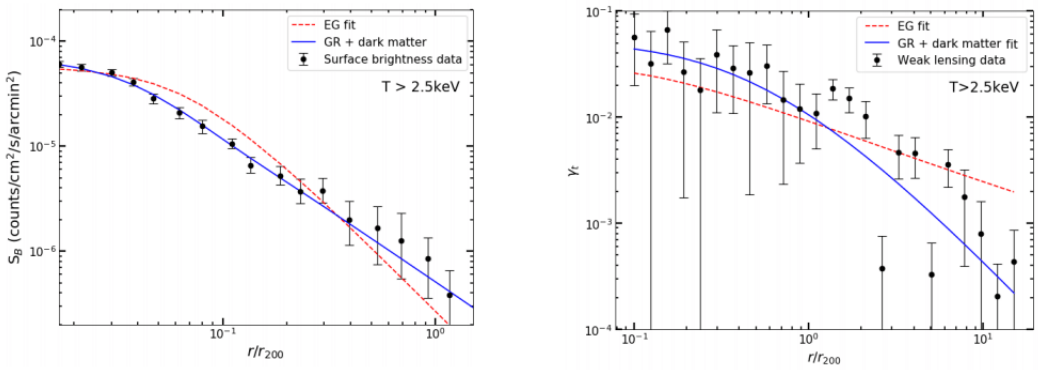

Figure 1.11: Comparison of the Emergent Gravity and LCDM for the $T_X > 2.5$ keV temperature Figure (a) shows the surface brightness fit for both models. Figure (b) shows the weak lensing (tangential shear) fit for both models. Image taken from (Tamosiunas et al., 2019).

the cluster stack the predictions are only in good agreement at around the 1 - 2 Mpc scales, while for larger radii EG is in strong tension with the data. A Bayesian analysis showed a preference for GR in all the tested datasets.

These publications motivated this PhD project; using existing space-based X-ray observations of thousands clusters (from the ESA XMM-Newton satellite) and ground-based observations of gravitational lensing for these clusters (from the Dark Energy Survey) to constrain the nature of gravity, by comparing the radial profile of both sets of observations with gravity model predictions. The resulting constraints on gravity will either confirm GR on cluster scales (a major new constraint on the theory); or will lead to important new gravitational physics. Either way, the scientific community will be provided with valuable catalogues with X-ray and lensing properties, and tools for testing gravity with future ESA space missions (e.g. Euclid and Athena).

1.5.6 Other probes of screening mechanisms

The publications summarized in the previous section postulate the existence of an additional fifth force that can be screened in the outskirts of groups and clusters of galaxies, leading to an observed difference between the X-ray and gravitational weak lensing profiles of the clusters. Moreover, according to the MG theory that has been described so far, it is expected that on small scales this fifth force that arises in MG, affects certain astronomical bodies but not others (Jain et al., 2013). Galaxies and their components respond differently to the fifth force because they can be screened at different levels. Recent work using observations of

stars, black holes, and galaxies has become relevant to do tests at this regime, which covers different astrophysical environments and combines multi-wavelength data. Again, the β and ϕ parameters of MG theories (see Eq. 1.81) are probed by these type of astrophysical test.

Some of the signatures left by screening mechanisms in different settings include

- Enhanced velocities of unscreened galaxies of an order of tens of km/s are expected (given that typical peculiar velocities are a few hundred km/s).
- In MG theories the gas and stellar components respond differently to the external forces in these type of theories.
- The stellar disk may rotate more slowly than the gas disk in MG theories.
- The stellar evolution is altered, with giant stars in particular moving more rapidly through their evolutionary tracks in MG theories.

For further information see (Will, 2006; Jain et al., 2013) along with their bibliography.

1.6 Summary

In this chapter I have given a summary of the current knowledge of the nature of galaxy clusters and gave a general overview of two of the observables of clusters which I used to constrain gravity on cosmological scales. I started with X-rays, discussing the emission mechanisms presented in clusters and the scaling relations that can be derived from them. I then talked about gravitational lensing, showing some of the fundamental equations and their impact on clusters. I also have a given an overview of the current state of cosmology, the observed accelerated expansion of the Universe, and how it is explained with either the addition of dark energy or by modifying GR. I described how one of these modifications to gravity might be presented in clusters, specifically in the difference between X-ray and lensing cluster profiles. Finally, I ended this chapter by reviewing some of the recent research of modified gravity using clusters at a range of cosmological scales to put this later work into context. This thesis continues with Chapter 2, which provides information about the X-ray, optical, and lensing surveys used throughout this work. Chapter 3 covers the building of a new X-ray selected cluster catalogue with the use of the aforementioned surveys and the

study of its properties. Chapter 4 and Chapter 5 comprise the modified tests of gravity. This thesis ends with the conclusions in Chapter 6.

Chapter 2

Data Description

2.1 Overview

This chapter presents the optical and X-ray surveys used in this thesis. Section 2.2 describes the XMM-Newton Cluster Survey (XCS). The section explains how the X-ray data are collected and reduced, how images are generated, and how sources are detected and then assembled into a sample of cluster candidates. The methods use to extract the X-ray properties of XCS clusters are also explained. Section 2.3 describes the Dark Energy Survey (DES), which is a ground-based wide-area optical and near infrared imaging survey. The section explains how DES collects, processes, and calibrates high quality data products. Section 2.3.3 goes on to describe how weak lensing information is extracted from DES. Section 2.4 briefly reviews the salient aspects of the Sloan Digital Sky Survey (SDSS), in particular SDSS data release 13 and Stripe 82. This chapter continues with a discussion of the redMaPPer cluster finder algorithm which has been applied to both, DES and SDSS (Section 2.5). This chapter ends with Section 2.6, where the CFHT Lensing Survey (CFHTLenS) is reviewed.

2.2 The XMM Cluster Survey

The XMM Cluster Survey (XCS) (Romer et al., 2000) collaboration searches for serendipitous detections of galaxy clusters in X-ray observations available from the XMM-Newton Science Archive. The primary goals of XCS are to measure cosmological parameters, to measure the evolution of the X-ray scaling relations (in particular the luminosity-temperature relation), to study galaxy properties in clusters at all redshifts, and to provide high quality, homogen-

eously selected X-ray cluster samples.

2.2.1 The XMM-Newton Space Observatory

The XMM-Newton Space Observatory mission, undertaken by the European Space Agency (ESA) and launched on December of 1999, consists of three separate X-ray telescopes mounted on the same spacecraft (XMM-Newton Community Support Team, 2018). This configuration allows the three cameras to be illuminated simultaneously, meaning that most XMM exposures generate data with potential for serendipitous cluster finding.

The European Photon Imaging Camera (EPIC) mounted on XMM consists of three separate cameras (MOS1, MOS2, and PN), each in the focal plane of a separate X-ray telescope. Each camera consists of an array of charge coupled devices (CCDs) in different configurations. These CCDs are sensitive to the energy of incoming photons, allowing users to produce spectra of detected sources with one entry per received event (event lists). Both MOS1 and 2 cameras and the more sensitive PN camera are capable to perform imaging observations over a field of view of 30 arcminutes within the energy range of (0.15 - 15 keV) with an angular resolution of 6.6 arcsec.

2.2.2 XMM data reduction

The public XMM data archive by now contains thousands of public observations that can be exploited by XCS. This large volume of data is mainly processed automatically in a fully consistent and systematic manner, leaving the optical inspection, and quality control to be handled manually. The XMM observations are downloaded via command line access to the XMM-Newton Science Archive[1]. The observations analyzed include all areas suitable for cluster searching, excluding areas such as the Milky Way ($|b| < 20^o$) and the Magellanic clouds. Resulting in 10,742 observations (at the time the work presented in Chapter 3 was developed) with data from at least two of the three cameras (see Sec. 2.2.1), each one with an associated Observation ID (ObsID) to it, across the whole sky. The data has been calibrated and treated for background flares extensively in the same manner as (Lloyd-Davies et al., 2011) with updated algorithms. After this process, co-added images are generated and flux conversion factors calculated. For regular (i.e. not mosaic mode) XMM observations the

[1] http://nxsa.esac.esa.int/nxsa-web/home

image generation used for this work is an improved version of the original XCS methodology depicted in (Lloyd-Davies et al., 2011). The changes mainly related to software updates.

2.2.3 Detecting sources in XMM

Images and exposure maps were produced with a 4.35 arcsec pixel size, a size smaller than the XMM point spread function (PSF), in the soft ($0.5 - 2$ keV) and hard ($2 - 10$ keV) X-ray bands. The individual images and exposure maps were merged to create a single image per ObsID. Next, the energy conversion factors (ECFs) are calculated, these depend upon an absorbed power-law model and are affected by the source, instrument properties, and the H_I column along the line of sight. Once the images are generated, they are passed to the XCS Automated Pipeline Algorithm (XAPA) to detect X-ray sources. XAPA is based on the source detection package `WaVdetect` (Freeman et al., 2001), a multiscale wavelet algorithm that first detects sources to later classify them compared to the position dependent PSF, as extended, or point-like. XAPA was run for all candidates in areas suitable for cluster finding (see Sec. 2.2.2). For a detailed explanation on how the XAPA routine works see (Lloyd-Davies et al., 2011).

XAPA produces an individual source list from each of the science exposures. These individual lists are then concatenated, with repeats removed into a single Master Source List (MSL). The work presented in this thesis makes use of XAPA outputs from 9,860 ObsID's, which resulted in a MSL comprising 275,498 point and 34,198 extended sources (see Sec. 3.2).

Not all XAPA extended sources are galaxy clusters. This is mainly due to the comparison of the source extent to the poorly understood PSF of XMM. The PSF describes how a point source of light in the sky is mapped into a two dimensional profile on the image, it depends on the projected distance of the object from the centre of the observation (or "off-axis angle") and the number of photon counts. Figure 2.1 shows examples of XAPA detections of several sources misclassified as extended. From left to right, the figure includes: foreground galaxies and stars; a low-redshift extended sources split into two; the components of a point source emission split into multiple; an Active Galactic Nuclei (AGN) detected as an extended source; and the gap between chips in the XMM fov. Therefore, it is necessary to carry a visual inspection to confirm if the extended sources classified by XAPA are indeed clusters, specially those flagged as PSF-sized. An example of this type of inspection is described in detail in Chapter 3.

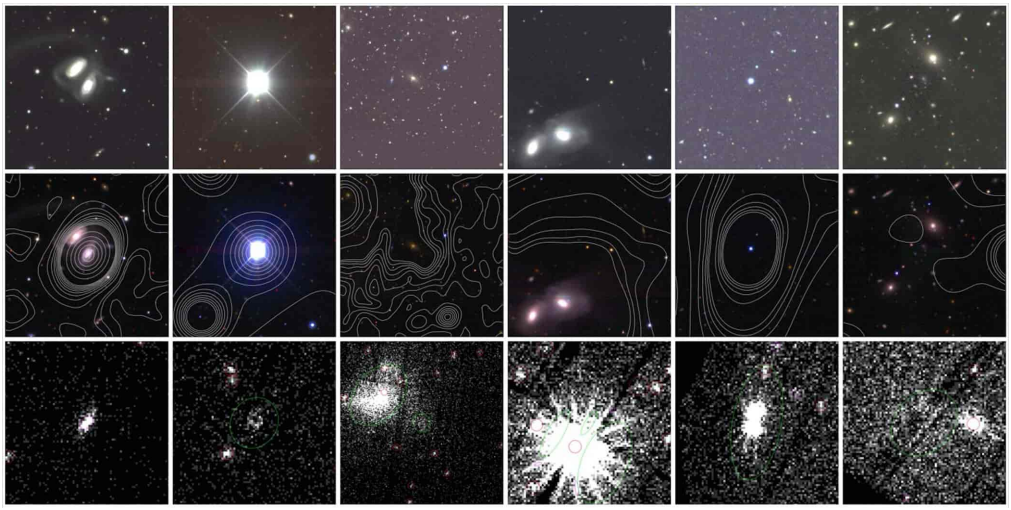

Figure 2.1: Examples of XAPA false detections. For each example, the images shown are (from top to bottom): the NCSA DES tiff (see Sec. 2.3.1), the optical with X-ray contours, the X-ray with XAPA detected sources, and the X-ray in false colours. From left to right: a spiral galaxy classified as a PSF source, a point source classified as an extended source, low-redshift galaxy cluster split into two extended sources, a point source emission components split into multiple extended sources, an AGN emission detected as an extended source, and a chip gap also classified as an extended source.

2.2.4 X-ray properties

The XCS Post Processing Pipeline (XCS3P) was used to derive the X-ray spectral properties of galaxy clusters, namely their X-ray temperature (T_X) and Luminosity (L_X). The cluster spectra is extracted and fit using the `XSPEC` (Arnaud, 1996) package. The fits were performed in the 0.3 - 7.9 keV band with an absorbed MeKaL model (Mewe, Lemen and Oord, 1986) (`wabs`$\times$`mekal`) using the c-statistic method. The `wabs` component accounts for photoelectric absorption by neutral hydrogen along the line of sight to the cluster, and the `mekal` component models the X-ray emission from a hot diffuse gas enriched with various elements. The redshift is fixed, leaving only the `mekal` temperature and normalization as free parameters. An pdated version of XCS3P was used for this thesis in comparison to the version of Lloyd-Davies et al. (2011), the changes and a more detailed explanation of this procedure can be found on P. Giles et al. (in prep.).

An aperture region for the spectral extraction is performed to derive the X-ray temperature. This is done by fitting an elliptical aperture using the length of the XAPA defined major axis. The spectral extraction region has been updated to extract spectral properties within the radius at which the density of the cluster is δ_c times the critical density of the Universe at

the cluster redshift (see Sec. 1.2.4 and Sec. 1.4.2). The radii considered for the analysis are r_{500} and r_{2500} which are commonly used in the literature. Then, based on (Arnaud, Pointecouteau and Pratt, 2005)

$$E(z)r_{500} = 1.104 \left(\frac{T_X}{5\text{keV}} \right)^{0.57}, \tag{2.1}$$

where $E(z)$ is the energy density of the Universe given by Equation 1.51. An initial temperature T_X is computed using XAPA's estimate of the source region to determine a first guess of r_{500} using Equation 2.1. Once the first T_X is obtained, a second values is defined within this circle, which is used now to define a new value of r_{500}. The process is done in a iterative manner until r_{500} converges with the ratio of the new to the old value of r_{500} defined to be < 0.9 and < 1.1. The background is accounted for by applying a local annulus centered in the cluster, using an inner and outer radius of $1.05 \times r_{500}$ and $1.5 \times r_{500}$ respectively. If r_{2500} is being used instead, the same procedure can be applied. A variation coeficient (Chernoff and Djorgovski, 1989), defined as the ratio of the standard deviation, σ, to the mean, μ, given by $C_v = \sigma(T_X)/\mu(T_X)$, is calculated during each iteration. For this work, a value of $C_v < 0.25$ was adopted as an indicator of a reliable measurement. The bolometric luminosity is derived from the X-ray temperature with the use of up to date estimations of Equation 1.19. I measured cluster temperatures and luminosities for different samples in Chapter 3, Chapter 4, and Chapter 5, as well as a contribution for different publications (see Appendix A).

2.2.5 XCS data releases

Previous XCS catalogues include the first and second data releases,

- **XCS-DR1**. The first data release of XCS (XCS-DR1) (Mehrtens et al., 2012) contains 503 optically confirmed serendipitously detected X-ray clusters. The optical confirmation was carried out by visual inspection of optical images. A search for photometric and spectroscopic redshifts was made for each of the clusters in the sample, using several literature sources, together with follow-up optical observations. Of the 463 clusters with redshifts (within $0.06 < z < 1.46$), a total of 401 clusters have associated X-ray temperatures within $0.4 < T_x < 14.7$ keV.

- **XCSDR2-SDSS**. The XCSDR2-SDSS catalogue (Manolopoulou et al., 2017), a subset of XCS second data release, comprises 1,255 optically-confirmed clusters within the SDSS

DR13 footprint, with 903 of these being serendipitous detections, making it the largest cluster sample derived from XMM observations to date. A visual classification process was made following the method covered in Section 3.4.1. After assigning redshifts to the cluster sample, 1,143 have associated X-ray temperatures within $0.22 < T_x < 14$ keV (median 2.6 keV), within a redshift range of $0 < z < 1.18$ (median 0.28). A more thorough description of this sample and my contribution to its development can be found in Section 3.8.2.

2.3 The Dark Energy Survey

The Dark Energy Survey[2] (DES) is an optical and near-infrared imaging survey of 5,000 square degrees of the southern sky. The survey began operations on August, 2013, using a 570 megapixel camera (DECam) with a 3 square degrees field of view on the Cerro Tololo Inter-American Observatory (CTIO) 4m Blanco telescope in Chile (Honscheid et al., 2008). The main goal of DES is to determine the dark energy equation of state $w(z)$, among other cosmological parameters, using several probes that include; the counts of galaxy clusters, weak gravitational lensing, and galaxy power spectra (see (Abbott et al., 2016) for more details). Due to the large area, depth and image quality of DES, the data supports optical identification of a large number of galaxy clusters and groups up to redshift $z \sim 1$.

The target footprint of the DES wide-area and supernova surveys are shown in Figure 2.2. The wide-area footprint shape was selected by the collaboration to obtain a large overlap with the South Pole Telescope survey (SPT)(Carlstrom et al., 2011) and Stripe 82 from SDSS (Gunn et al., 2006). Given the scientific goals of the survey, DES avoids the Galactic plane to minimize stellar foregrounds and contamination from interstellar dust. The images taken were processed with the DES Data Management (DESDM) system (Mohr et al., 2012), and its outputs validated and filtered to produce the high-quality catalogues.

2.3.1 Image processing

A basic event in an astronomical observation of DES is the exposure. During an event, the DECam camera is exposed to the night sky, generating a file that is written in FITS format. During the first three years of data collection (the Y1-Y3 period) a total 61,828 ex-

[2]https://www.darkenergysurvey.org/

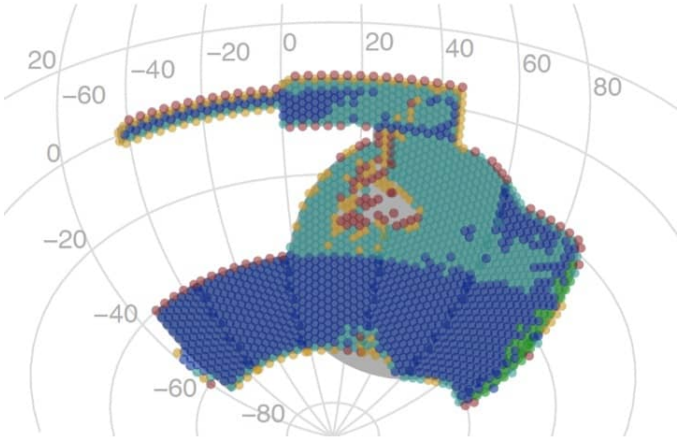

Figure 2.2: The footprint of the Dark Energy Survey. The coloured dots show the area observed by DES in its first year of operation. The grey colour shows the unobserved survey area, while areas covered by 1, 2, 3, 4, or 5+ observations are shown by red, orange, light blue, dark blue, and green dots, respectively. The survey uses large dithers to minimize the impact of any systematic errors related to the location on the field of view. Image taken from the Australian Astronomical Optics site (`http://www.aao.gov.au`).

posures, containing data in five filters: g, r, i, z, and Y, were produced. The images were corrected for instrumental effects as well as calibrated for the absolute position (astrometry) and absolute flux (photometry). Then, DES uses the Source Extractor software package (SExtractor)(Bertin and Arnouts, 1996) to optimally detect, deblend, measure, and classify sources from the astronomical images.

In order to enhance the signal to noise of real sources in an image, it is necessary to perform a process called image coaddition. As the name suggests, this step involves the combination of multiple overlapping single exposure images. The PSF of DES is defined as a circular Moffat function with a Full Width at Half-Maximum (Abbott et al., 2018), which is the median of the seeing distribution in the whole set of images contributing to a coadd. A caveat of the DECam PSF is that it changes within an image and from one image to another. This is due to the varying conditions of the exposure and quality of the sky during an observation. Transient effects such as satellite trails or cosmic rays are also eliminated during this step. The size of each coadded image is $10,000 \times 10,000$ pixels with a pixel scale of 0.263 arcseconds, for further details about this process see Sevilla et al. (2011).

2.3.2 Optical catalogue

The final step of the image processing consists in transforming the coadded images (in their different filters) into single entries in a catalogue, for its release. The SExtractor pipeline is applied in this step too, detecting the sources location and extracting the relevant information from the coadded images. The catalogued information includes: the coordinates for the objects, the morphological object information, several different photometric and non-photometric measurements and its associated uncertainties (Sevilla et al., 2011). The coadd source extraction process detected and catalogued 399,263,026 distinct objects during the Y1-Y3 period (Abbott et al., 2018).

Access to the DES data releases is provided mainly through the National Center for Supercomputing Applications (NCSA) at the University of Illinois at Urbana-Champaign in the United States. DESaccess[3] provides the user with an interface to submit synchronized jobs to perform SQL queries against an Oracle DB that contains the different DES catalogues, and to generate cutouts from a given list of positions from the coadded images.

The main service used for this work was the cutout server[4], which allows the user to generate cutouts up to 10 arcminutes on a side centered on a given set of positions. Each of the output files contains cutouts in all five bands, a cutout in the detection image and a color image using the (g, r, i) bands. It is important to notice that no stitching is performed for a submitted position near the edge of a tile. Up to the date this work was made there have been three DES releases, these are summarized in the following section.

Releases

To the date this work was completed, three major releases were done by DES.

- **Science Verification**. Before the main survey started, a small Science Verification (SV) survey consisting of 858 coadd tiles over $\sim$ 250 square degrees was conducted from November 2012 to February 2013. The goal was to simulate the full five year DES survey, in terms of number of visits and image depth, by observing 10 different epochs of the SV area. In order to accomplish this, each tiling was observed on different nights to vary the observing conditions as much as possible. This caused significant depth

[3] https://des.ncsa.illinois.edu/easyweb
[4] https://descut.cosmology.illinois.edu/

variations in the SV data due to weather, issues with the telescope, and no data quality checks to ensure uniformity (Leistedt et al., 2015). The SVA1 Gold Catalogue[5] includes at least one observation in each of the (g, r, i, z) bands.

- **Year 1 Data Release**. The first public data release (Abbott et al., 2018) consists of reduced single-epoch images, coadded images, coadded source catalogues, and associated products and services assembled over the first three years of DES science operations. It covers approximately 5,000 square degrees of the southern Galactic cap in five broad photometric bands (g, r, i, z, Y). It has a median delivered PSF of $g = 1.12, r = 0.96, i = 0.88, z = 0.84$, and $Y = 0.90$ arseconds. DES DR1 includes nearly 400M distinct astronomical objects detected in $\sim 10,000$ coadd tiles produced from $\sim 39,000$ individual exposures.

- **Year 3 Data Release**. The Y3A2 COADD catalogue (hereafter DES Y3) used for this work was also built from the first three seasons of DES operations, covering about more than ten times the area of SV. It contains CCD coadded data in the (g, r, i, z, Y) filters, consisting of 61,828 exposures with exactly the same median delivered PSF of that of DES DR1. The DES multi-epoch pipeline from the DESDM reduced the coadded images as explained in the previously.

2.3.3 Lensing survey

DES is the largest ongoing lensing survey designed to obtain as much statistical power with a well thought optical design and a precision modelling to measure weak lensing by computing the ellipticity of distant galaxies. It is part of the current "Stage III" group of lensing surveys along with KiDS (Hildebrandt et al., 2016) and HSC (Aihara et al., 2014), which together with DES are surveys that cover over 1,000 square degrees and will obtain cosmological constraints comparable in power to other cosmological data. In comparison Stage II surveys, which included (among others) CFHTLenS (see Sec. 2.6) and the Science Verification (SV) of DES, have deep and wide survey, up to hundreds of square degrees that allowed them to obtain significant cosmological constraints. Upcoming surveys (Stage IV surveys),

[5] https://des.ncsa.illinois.edu/releases/sva1

like Euclid[6], LSST[7], WFIRST[8], and SKA[9], will measure the dark energy equation of state with 1% precision when combined with data from the CMB. Up to this date, DES has made two major releases: the Science Verification shear catalogue (SV) (Jarvis et al., 2015) and the Year 1 (Y1) (Zuntz et al., 2018a) shape catalogues which were used for this thesis. The process of creating these catalogues will be covered in the following sections.

Data

The DES Y1 shape catalogues cover an area of $\sim 1,500$ square degrees with a median redshift of 0.59. In comparison, the SV catalogues covered $\sim$ 139 square degrees but with a higher integrated exposure time than Y1. However, due to a more rigorous image quality assessment carried for the image collection, the quality of the Y1 imaging is superior than the one taken in SV. Objects in the Y1 catalogues were limited to have photo-z point estimates within the redshift range (0.2 – 1.3), and to fall within Stripe 82 (see Sec. 2.4.1) and the southern portion of the DES footprint (dec <-35), which overlaps with the SPT (Carlstrom et al., 2011) footprint. The data was reduced by DESDM (Mohr et al., 2012), resulting in calibrated and background-subtracted images. The object catalogues were produced using SExtractor (see Sec. 2.3.1) and all the overlapping single-epoch images were combined into a coadd image. These coadd images were used for weak lensing for object detection, deblending, fluxes, and for determining good sets of galaxies to be used for shear measurement.

Multi-Epoch Data Structures (MEDS) were created to collect all available relevant information for a given object into one easy to handle file. Each MEDS file contains the associated cutout images for each observation of every object in the coadd along with its corresponding weight maps, segmentation maps, and other significant data.

The object catalogue that was created excluded regions with bad data due to imaging artifacts, scattered light, failed observations, etc. The selection criteria required objects; to have been observed at least once in each of the i, g, r, and z bands; to avoid the Large Magellanic Cloud and R Doradus; to remove regions with a high density of objects with large range of colours; to remove regions with a density less than 3σ below the mean density; to remove regions near bright stars; and to remove regions with a concentration of objects with large

[6]https://www.euclid-ec.org/
[7]https://www.vro.org/
[8]https://www.nasa.gov/content/goddard/about-nancy-grace-roman-space-telescope
[9]https://www.skatelescope.org/

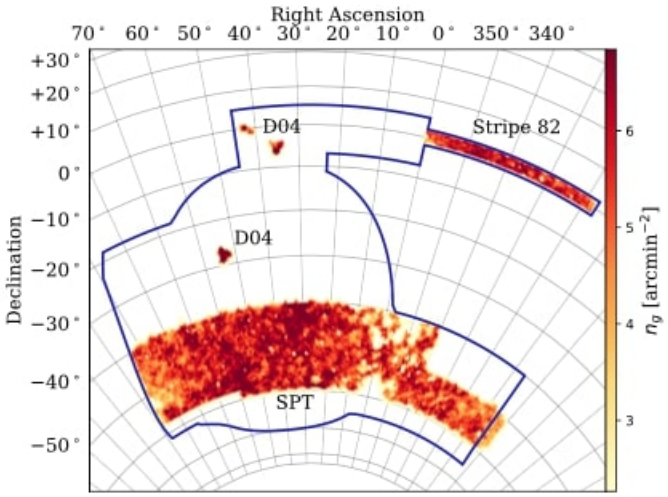

Figure 2.3: The DES Y1 shear catalogue footprint with galaxy density of the METACALIBRATION catalogue shown with the 5-year DES footprint outline overlayed, taken from (Zuntz et al., 2018a). IM3SHAPE is qualitatively similar, but slightly shallower. Three fields are defined in this image: (i) The large, southern field overlapping with SPT. (ii) The long equatorial strip overlapping with SDSS Stripe 82. 3) The disjoint supernovae and spectroscopic-overlap fields.

centroid shifts between bandpasses. Images within 30 pixels of the edge of a CCD were removed to avoid growing-edge effects. Images with poor astrometric solutions, poor PSF solutions, and blacklisted CCDs were not taken into consideration when the catalogue was being made. The outputs of these previous steps are run through the shape measurements pipelines which are described below.

Systematic errors

There are many potential sources of systematic errors coming from the image processing that can bias the shape measurements used for estimating shears. Some examples include; blurred and smeared galaxy images due to the atmosphere; stretched images by distortion; variable PSF due to the telescope optics or its detector; images with various sources of noise from artifacts; and the flux from nearby galaxies or stars. All of these issues are dealt with in the analysis at very high accuracy, as detailed in (Jarvis et al., 2015; Zuntz et al., 2018a).

Shear measurement

The shear pipelines employed by DES to measure galaxy shapes use Model-fitting methods (Massey and Refregier, 2005; Nakajima and Bernstein, 2007; Miller et al., 2011), which involve fitting a PSF convolved galaxy model to the data. The shape measurement of the Y1 catalogues was done using two shear algorithms: METACALIBRATION and IM3SHAPE. The associated data products are documented by Jarvis et al. (2015) and Zuntz et al. (2018a) in the weak lensing shear catalogues papers.

METACALIBRATION (Huff and Mandelbaum, 2017; Sheldon and Huff, 2017) computes shear measurements by deriving shear calibrations directly from available imaging data. An advantage of this pipeline is that it doesn't require significant prior information about galaxy properties or calibration from image simulations, reducing noise and model biases. METACALIBRATION was tested using an extensive set of simulations by Huff and Mandelbaum (2017), and proved to be umbiased for galaxy images and was shown to be robust to the presence of stars in the sample if the PSF is well determined. METACALIBRATION was the primary shear catalogue from the Y1 release.

IM3SHAPE (Zuntz et al., 2018b) uses a Levenberg-Marquadt minimization to find the maximum likelihood fit of two Sersic models, with power-law indices $n = 1$ and $n = 4$, to all the exposures of each galaxy simultaneously. Each galaxy is then identified as a bulge or a disc, depending on which model returned the superior likelihood. This code remained largely unchanged from that used for the SV catalogue (Zuntz et al., 2018a). Noise, model, and selection biases on the galaxy shapes are calibrated using a series of simulations designed to reflect real data. IM3SHAPE was applied only to r band images, yielding a smaller catalogue.

Due to the difficulty of comparing two shear measurement methods in a robust way, both pipelines were developed without direct comparison to the other and used different subsets of the Y1 data, different measurement techniques, and different calibration strategies. This was because any joint selection of the data may bias both methods (see (Zuntz et al., 2018a) for further details).

The METACALIBRATION and IM3SHAPE pipelines produced up to 34.8M objects and 21.9M objects respectively. During this process the pipelines measured galaxy ellipticities with two quantitites e_1 and e_2, and the ensemble shear in terms of either γ_1 and γ_2 or the reduced shears g_1 and g_2. Both catalogues show a non-zero mean ellipticity over the entire Y1 survey.

The data from these catalogues comprises only 20% of the full potential of DES, however the subsequent two years (year 4 and year 5) of data analysis have already begun. Both of them pass a multitude of tests for systematics, making them suitable for cosmological analyses. The shape catalogues from the pipelines were blinded before their usage in any of the DES science papers. This was done to avoid the experimenter bias effect towards their own preconceptions by preventing them from knowing their final result until the analysis is complete (Klein and Roodman, 2005).

Weak lensing shear catalogues

The final shear catalogues were made at NERSC and are publicly available on the DESDM releases web pages[10]. DES recommends to do further cuts to the final shear catalogues. The quality cuts are based on runs of the pipelines on simulations, in order to remove unreliable results. The most relevant pointed by Jarvis et al. (2015) are

- The parameter `error flag` marks objects where the shape pipeline failed to converge, when the object is too large or too faint to be resolved, etc.
- While the the `info dat` removes objects that are; too small, flagged by SExtractor, or without proper measured photometry, etc. Also, source galaxies with incomplete noise-bias calibrations were not included.
- $(S/N)_w > 15$ removes objects with low SNR. $(S/N)_w$ measures the SNR of a galaxy by taking a weighted average of the SNR values of all pixels in the galaxy.
- $R_{gp}/R_p > 1.2$ removes dim objects for which the photometry might not be too reliable.

The final METACALIBRATION shear catalogues have a number density of 6.38 galaxies per square arcminute, it was used as the default weak lensing catalogue for Y1.

2.4 The Sloan Digital Sky Survey

The Sloan Digital Sky Survey (SDSS) is a major multi-spectral imaging and spectroscopic redshift survey using a 2.5m wide-angle optical telescope, with a focal ratio of f/5 located at the Apache Point Observatory in New Mexico, United States (Gunn et al., 2006). The

[10] http://des.ncsa.illinois.edu/releases

telescope uses a multiband large format mosaic CCD camera to image the sky in five optical bands, and a pair of fiber-fed double spectrographs to obtain the spectra of about 1 million galaxies and 100,000 quasars (York et al., 2000). Since operations started in the year 2000, there have been thirteen public data releases. All these data releases are cumulative, re-releasing the best reduction of all previously taken data. The most recent of these is the Data Release 13 (Collaboration, Albareti and Prieto, 2016). From the first generation of SDSS (SDSS-I) to the fourth generation (SDSS-IV) 14,555 square degrees have been imaged in the five filters, which represents just over 35% of the full sky. Most of the sky was surveyed once or twice, but regions in Stripe 82 were observed between 70 and 90 times.

2.4.1 Stripe 82

The SDSS Stripe 82 is a $\sim$ 300 square degrees field near the celestial equator ranging from $-50 < \alpha < 60$ deg. and $-1.25 < \delta < 1.25$ deg. that has been imaged repeatedly (between 20 and 40 times) by the SDSS telescope (Collaboration, Albareti and Prieto, 2016) and coincides with the Northern portion of DES. The repeated observations of the region allows deeper coadded images to be made, which are $\sim$ 2 magnitudes fainter than a single SDSS pointing. All runs covering Stripe 82 were made available as part of the Stripe82 database, which is structured like the runs database.

2.5 The redMaPPer cluster finding algorithm

The red-sequence Matched-filter Probabilistic Percolation (redMaPPer) cluster finding algorithm is an algorithm specifically designed to identify clusters as an overdensity of red-sequence galaxies (Rykoff et al., 2014). It relies on iteratively self-training a model of the red-sequence as a function of redshift, based on the red galaxies with known spectroscopic redshifts. The red sequence technique consists in detecting galaxy clusters not by observing a visual overdensity of galaxies, but an overdensity of galaxies at approximately the same redshift (Gladders and Yee, 2000). This model is used on photometric data to assign membership probabilities to galaxies with luminosities $> 0.2L$ in the cluster vicinity. redMaPPer estimates cluster richness, λ, as the sum of the membership probabilities of the galaxies within a radius R_λ which scales with richness as $R_\lambda = (\lambda/100)^{0.2} h^{-1}$ Mpc. The individual photometric redshift of the clusters is evaluated by simultaneously fitting all high probab-

ility cluster members with a single red sequence model, with an accuracy of $0.005 - 0.01$. Where the cluster centre lies on the central galaxy chosen with a probabilistic approach that weights not just galaxy luminosity, but also local galaxy density, as well as the consistency to cluster redshift.

2.5.1 Photometric redshifts

Using the red-sequence model, Rykoff et al. (2014) has derived two red-sequence based photometric redshifts. The first z_{red}, is a red-sequence template based photometric redshift, designed to generate a first 'acceptable' estimation of the redshift in each cluster. Proved to be a good estimator compared to existing photometric redshifts, z_{red} has the advantage of requiring fewer spectroscopic training galaxies. The second, z_λ, is obtained from z_{red} to estimate the cluster richness and determine the high probability cluster members. Then, all cluster members are simultaneously fit to the red sequence model to derive an improved redshift approximation. This process is iterated until it converges, getting a final value for z_λ.

2.5.2 Catalogues

Up to this date redMaPPer has released three catalogues:

- The first redMaPPer cluster catalogue included 26,111 clusters identified from SDSS DR8 (Rykoff et al., 2014), with photometric redshifts within the range $0.08 < z < 0.60$ (volume-limited in $z < 0.35$) covering nearly 10000 square degrees of the sky. The completeness of the sample is 99% at $\lambda > 30$ and $z < 0.3$, and the purity is $> 95\%$ at all richness and redshift.

- An updated version of the algorithm was applied to 150 square degrees of the DES-SV data (Rykoff et al., 2016). The catalogue is locally volume limited, and contains 786 clusters with richness $\lambda > 20$ and $0.2 < z < 0.9$. A reliable cluster characterization of richness, photometric redshift, and centering probability was produced by making use of Chandra and XMM X-ray and South Pole Telescope Sunyaev-Zeldovich data.

- The redMaPPer algorithm was also applied to the DES-Y1 data (Mcclintock et al., 2017). The 6.4.21 version which contains 559,126 clusters, of which 51,821 have richness > 20 and $0.10 < z < 0.95$.

2.6 The Canada-France-Hawaii Telescope

The Canada-France-Hawaii Telescope (CFHT) is a 3.6 meter optical and infrared telescope (Boulade et al., 2003). The observatory is located atop the summit of Mauna Kea in Hawaii at an altitude of 4,200 meters. The CFH Telescope became operational in 1979 and has 4 instruments which can be used with the telescope: (i) the Megacam, a 340 megapixel optical and near infrared camera with a field of view of 1 degree; (ii) a 16 megapixel infrared detector with a field of view of 20 arcminutes; (iii) a high-resolution echelle spectrograph and spectropolarimeter; and (iv) a wide field optical integral field unit.

The Canada-France-Hawaii Telescope Legacy Survey (CFHTLS) (Hudelot et al., 2012) is a multi-component optical survey conducted over more than 2,300 hours in a 5 year span ($\sim$ 450 nights) using MegaCam (Boulade et al., 2003) on the MegaPrime imaging system of CFHT. The wide survey is composed of four patches ranging from 27 - 72 square degrees, together totalling an effective survey area of $\sim$ 154 square degrees. The data was acquired in the (u^*, g', r', i', z') filters and has a 5σ point source $i'-$band limiting magnitude of 24.5.

Cluster catalogue

The most complete cluster catalogue using the CFHTLS deep fields was made with the 3D-Matched-Filter (3D-MF) (Milkeraitis et al., 2018). This cluster finder uses galaxy cluster radial profiles, luminosity functions and redshift information to detect galaxy clusters in optical surveys. This cluster finder implements redshift slicing of the data to significantly reduce line-of-sight projections and related false positives. The reliability of the statistical approach of this method was tested using mock data from the Millennium Simulation (Kitzbichler and White, 2006).

When applied to the CFHTLS deep fields, 3D-MF found $\sim$ 170 galaxy clusters per square degree in the $0.2 < z < 1.0$ redshift range, which is in agreement with the Millenium Simulation cluster number densities. 3D-MF also found over 400% more clusters, with a much lower false detection rate and higher accurate measured redshifts for true clusters, than any other CFHTLS deep field cluster finder using two-dimensional matched-filter methods. The catalogue was made public and can be accessed from the CFHTLS site[11]. Additional background and details on the algorithm can be found in (Milkeraitis et al., 2018).

[11] http://www.cfhtlens.org/

2.6.1 Lensing survey

The Canada–France–Hawaii Telescope Lensing Survey (hereby CFHTLenS) reduced the deep CFHTLS-Wide data and measured 7.6 million galaxy shapes, completing observations in 2009 for weak lensing science applications (Heymans et al., 2012). The CFHTLenS data span four distinct contiguous wide fields: W1 ($\sim$ 63.8 sq. deg), W2 ($\sim$ 22.6 sq. deg), W3 ($\sim$ 44.2 sq. deg) and W4 ($\sim$ 23.3 sq. deg) in the five optical bands of CFHTLS. The data is available at the Canadian Astronomical Data Centre (CADC) through a web interface[12]. The catalogues can be accessed with a sky-coordinate query form with filter options on all catalogue entries.

2.7 Summary

In this chapter I discussed the X-ray, optical, and weak lensing data, namely the XCS MSL, DES Y3 data release, DES Y1 shape catalogues, SDSS-DR13, redMaPPer, 3D-MF, and CFHTLenS that will be used through the rest of this thesis. All the X-ray cluster candidates and images in this thesis were selected from the latest (when this work was being developed) XCS MSL ran by XAPA. All the X-ray features of the clusters used throughout this work were computed using the XCS3P pipeline of XCS. All the optical imaging from DES was processed, calibrated and provided by DESDM. Optical images (mainly from the Y3 release) for the (g, r, i) bands were downloaded using the cutout server developed by DESDM for Chapter 3. The SDSS-DR13 was used to build an XCS cluster catalogue of the north hemisphere of the sky (see Sec. 3.8.2). The redMaPPer Y1A2 catalogue version 6.4.21 was used to assign redshifts to the clusters in the sample of Chapter 3. The DES Y1A1 Gold catalogue and the CFHTLenS shear catalogue were used to extract galactic ellipticities around our cluster samples in order to build shear profiles in Chapter 4 and Chapter 5.

[12] `http://www.cadc-ccda.hia-iha.nrc-cnrc.gc.ca/community/CFHTLens/query.html`

Chapter 3

The Second XCS Data Release in the DES Y3 footprint

3.1 Overview

The optical wavelength allows us to efficiently develop large cluster samples, up to several hundred thousand objects with the latest generation of surveys, such as DES (see Sec. 2.3.1). However, optical selection methods will always suffer from projection effects. To alleviate this problem, multi-band photometric data is now broadly used to build cluster samples. Examples of cluster samples that have been built this way include: SDSS (Koester et al., 2007; Hao et al., 2010; Szabo et al., 2011; Rykoff et al., 2014; Wen, Han and Liu, 2012), CFTHLS (see Sec. 2.6), the Blanco Cosmology Survey (Bleem et al., 2014), the Hyper-Suprime Cam survey using the CAMIRA algorithm (Miyazaki et al., 2012; Oguri et al., 2018; Miyazaki et al., 2015; Murata et al., 2020), and DES (see Sec. 2.5). X-ray selected clusters play an important role in the validation and parameterisation of optical cluster catalogues (Andreon et al., 2016).

This Chapter presents, in detail, the compilation of a new X-ray selected sample of clusters. This makes use of the XMM archive, as processed by the XCS collaboration, and the optical data available in DES Y3 footprint (DES-XCS hereby). I present the data products used, the methodologies employed, and an analysis of the catalogue that has been produced. Unlike the first data release of XCS (see Sec. 2.2.5) which used heterogeneous imaging data, reducing the number of potential candidates that could have been added to the final catalogue, this work intends to build a well selected X-ray cluster sample with better measured X-ray

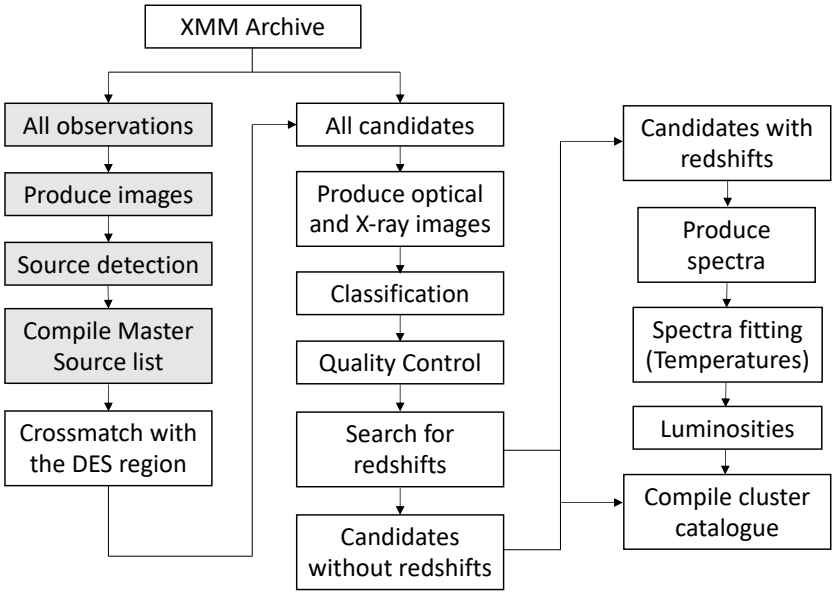

Figure 3.1: Flow chart showing an overview of the DES-XCS analysis methodology. The figure illustrates the sequence by which data from the XMM archive are used to create a catalogue of galaxy clusters. The boxes filled in grey correspond to automated steps done by the XCS pipeline (see Sec. 2.2.3).

properties from updated pipelines (see Sec. 2.2.3) taking advantage of the wide coverage and depth of DES (see Sec. 2.3.1). A simple schematic of the processes used to develop the catalogue is shown in Figure 3.1. Section 3.2 describes the X-ray selected cluster candidate list generated by XAPA. Section 3.3 describes the production of optical images using the (g, r, i) bands of DES combined with the X-ray images from XCS. Section 3.4 explains how the visual inspection was carried. Section 3.6 covers the process by which redshifts were assigned to the clusters. Section 3.7 presents the XCS3P determined X-ray temperatures and luminosities (see Sec. 2.2.4). Section 3.8 summarizes the properties of the sample and makes some comparisons with other catalogues produced by XCS. Section 3.8.2 describes the second XCS data release in the SDSS DR13 footprint, a parallel work to this study which followed the same methodology and analysis presented here and for which I provided a significant input. This chapter ends with the study of X-ray scaling relations.

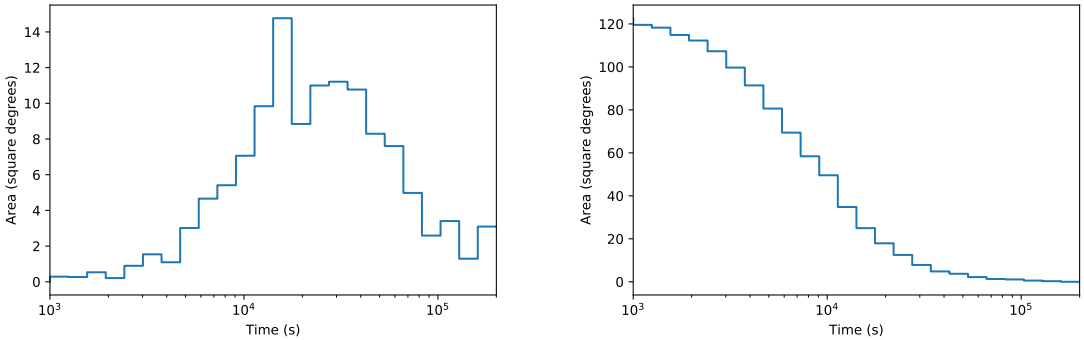

Figure 3.2: Histogram (left) of the area of the sky covered as a function of cleaned exposure time and cumulative histogram (right) of sky covered by XCS within the footprint of DES as a function of the exposure time.

3.2 Selection of X-ray cluster candidates

Being able to quantify the joint X-ray and optical area is the initial step in creating a well characterized sample for cosmological and statistical applications. Nevertheless, combining both data sets is complicated, particularly due to the heterogeneous sky coverage and depths of both surveys. I used different methods to exclude bad or non-reliable data in order to have a trustworthy flux limit in the resulting catalogue. To create a cluster candidate list with X-ray data and their optical counterpart from DES, I first selected sources already classified as extended by XAPA in the latest MSL from XCS (see Sec. 2.2.3). These extended sources had to also come without any warning flags, which are associated to sources that are more extended than the instrument PSF or extended sources with internal point sources. Secondly, I chose candidates detected with more than 200 X-ray background subtracted photon counts in the $(0.5 - 2.0\text{keV})$ range. This lower limit was set in order to ensure reliable X-ray temperatures and luminosities (avoiding large errors in T_X measurements as shown in Figure 17 in (Lloyd-Davies et al., 2011)). However, a cut on photon counts may exclude cluster candidates at higher redshifts, or cool clusters/groups. For candidates that were detected in multiple observations, the observation with the highest recorded counts for the respective XAPA extended source was used. The area of the DES Y3 footprint (see Fig. 2.2) covered by XCS, as a function of XMM exposure time, is displayed in a histogram in Fig. 3.2 (left), while the cumulative plot of the same data is shown in Fig. 3.2 (right).

Of the $\sim 300,000$ sources in the latest MSL from XCS, 34,198 sources were classified as

Stage	No. of candidates
Extended sources in the MSL	34,198
Candidates with counts over 200	13,443
Candidates in the DES Y3 footprint	2,082
Candidates after the PSF sized flag cut	1,682
Sample to be visually inspected	1,551

Table 3.1: Steps made during the selection of X-ray candidates.

extended by XAPA, with 13,443 of them having over 200 counts. Only 2,082 of these cluster candidates were in the DES Y3 footprint. Of these, 566 candidates had a PSF size flag (see paragraph above). For these 566, the XCS PI and project scientist (K. Romer and P. Giles) made an initial eye-ball inspection to determine if the source was genuinely extended and not an artifact (see Sec. 3.4.1). Most of these 566, 400 in all, were removed by this initial inspection, reducing the candidate list to 1,682 sources. Next, I inspected the preliminary optical images and the off-axis angle information of the candidates, (see Sec. 3.5). As a result, 131 further sources were discarded for being erroneous detections by XAPA (see Fig. 2.1). This further reduced the candidate list to 1,551 sources. Table 3.1 summarizes the number of candidates obtained in each of the steps described above. I then made optical images with X-ray overlays for each of the 1,551 candidates and visually classified them in a systematic fashion (see Sec. 3.4.1). The process of creating the optical images is described in detail in the next section.

3.3 Image production

Due to the low resolution of the images provided by the cutout service of DES (see Sec. 2.3.2), I decided to make my own optical images using the (g, r, i) band images from DES and the software package STIFF ('STIFF v2.2 User's guide'). In summary, STIFF reads three input FITS images for each of the primary colours, red (r-band), green (g-band), and blue (i-band), to convert them into a TIFF format (or any other format). Once the colour images are generated for each of the cluster candidates, the corresponding XMM data is overlaid as contours on the optical image. An example of an optical image made with STIFF and X-ray contours overlayed is shown in Figure 3.3.

Figure 3.3: An example of an optical image made with STIFF using the colour-band files form DES with X-ray contours overlayed. The image displayed corresponds to the source XMMXCSJ210418.5-412037.2 (DESJ210418.6-412037.2).

3.4 Optical inspection

After taking advantage of the DES imaging coverage and depth to create optical images (see Sec. 2.3.1), I decided to visually inspect the X-ray selected cluster candidates obtained in Section 2.2.4 in order to verify their status as clusters. For this, I initiated a cluster classification project in Zooniverse[1], and invited members of the XCS and DES collaborations to classify my cluster candidate sample.

3.4.1 DES-XCS Zoo

Zooniverse offers a suitable environment for scientist-crowd-sourced analyses, offering options for various applications on images, discussion forums and different sets of subjects to be analyzed, available as public or private projects. I created a workflow as the project manager, which in the case of the DES-XCS Zoo project was a question of whether the object being classified is a galaxy cluster or not. A list of cluster candidates was then uploaded by the project manager to be classified under this workflow. For each subject, I showed three sets of four images: the DES NCSA colour image, the optical image with overlaid X-ray contours, the XMM observation, and the soft-colour false XMM image, each of these in a 3×3, 6×6 and 12×12 arcmin field of view. The classifier then had to choose one of the four options for each subject:

1. Cluster. An object with an X-ray extended source coincident with an overdensity of galaxies.

2. Possible cluster. An object with an X-ray extended source coincident with a moderate overdensity of galaxies or an object with an overdensity of galaxies coincident with an acceptable extended X-ray source.

3. Probably something else. An object that cannot be confirmed to be a cluster with the given data, or

4. Definitely something else. A false-detection given as a foreground galaxy, a star, a source next to the edge of an observation, or next to a very bright X-ray source.

[1] www.zooniverse.org

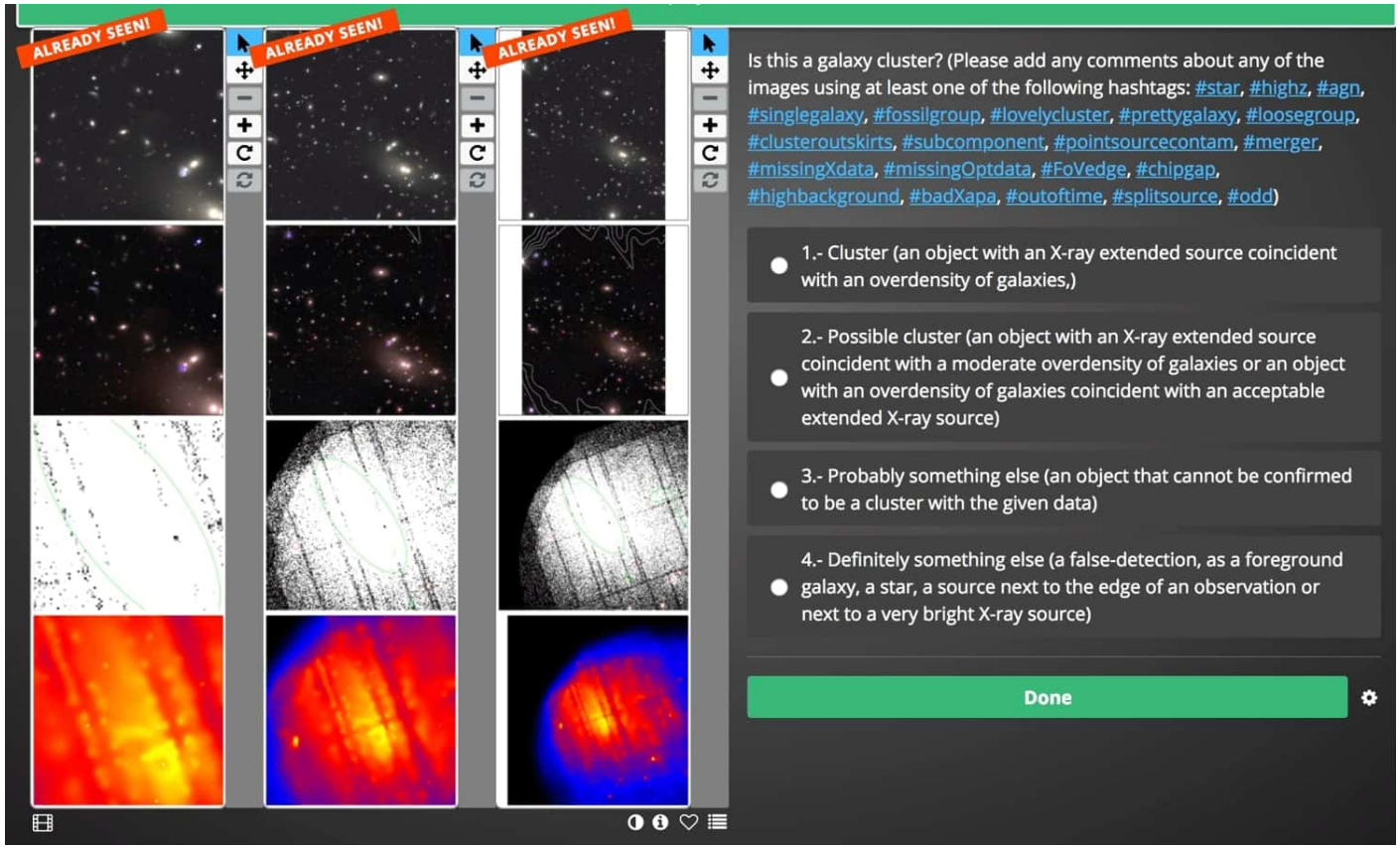

Figure 3.4: Screenshot of the display of the DES-XCS Zoo project. Each of the cluster candidates is presented in different sets with: the DES NCSA colour image, the optical image with overlaid X-ray contours, the X-ray image, and the soft-colour false X-ray image in 3×3, 6×6, and 9×9 sizes. The display of the images can be changed with the buttons at the bottom. The four classification options are on the right. The hashtags correspond to different extra features that could be found in the images for their discussion.

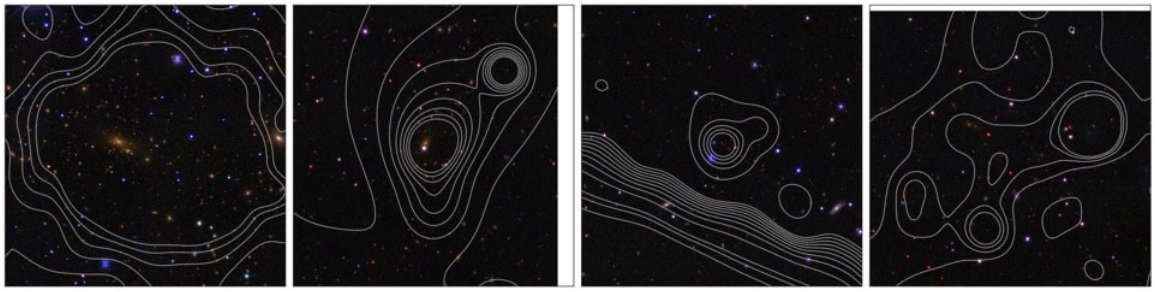

Figure 3.5: Examples of four sources classified in the DES-XCS Zoo exercise, from left to right: cluster, possible cluster, probably something else, and definitely something else. The sources from left to right correspond to: XMMXCS J212939.7+000516.9 with a classification score of 3.0, XMMXCS J231529.4-530348.6 with a score of 2.5, XMMXCS J012325.3-584213.3 with a score of 1.33, and XMMXCS J033416.2-360426.2 with a score of 0.0.

Figure 3.4 shows an example of the display in the Zooniverse website, featuring the different images and classifying options. Each cluster candidate was classified at least three times by three different members of the collaboration. A discussion board through the use of hashtags was made available for any comments on a specific subject by the participants. Examples of sources with different classifications are shown in Figure 3.5, from left to right: cluster, possible cluster, probably something else, and definitely something else.

Concerning the PSF-sized objects mentioned in Section 3.2, a first visual inspection of these objects was done before the DES-XCS Zoo project. Having an identical structure as the main project, this project featured the question of whether the subject in display should be added to the main candidate list, accompanied by the same set of images as the main project for each subject. The resulting approved subjects of PSF Zoo project were included into the DES-XCS Zoo.

In total, 22 collaborators from XCS and DES entered the project and classified at least one of the subjects. At the end of the classification process, every candidate had a set of at least three classification numbers associated to them; option (1) gave 3 points to the candidate, option (2) gave 2 points, option (3) gave 1 point, and option (4) gave 0 points. I took the mean of the classifications as the total score for each of the subjects excluding subjects with a score bellow 1.5 and eyeballed again subjects with scores between 1.5 and 2 before adding them to the final sample. This allowed me to dismiss misclassifications by members of the collaboration. The total number of optically confirmed clusters obtained from this exercise is summarized in the next section.

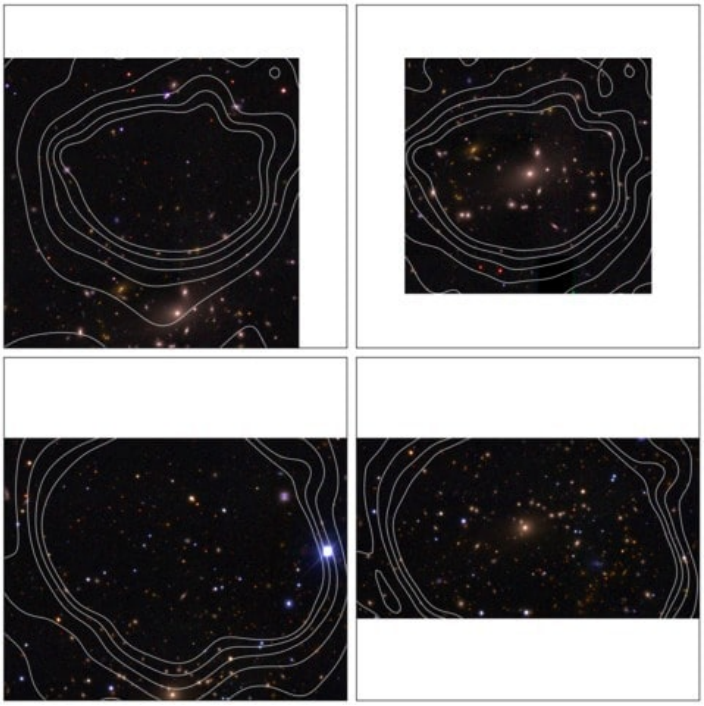

Figure 3.6: Examples of images with an offset. On the top left XMMXCS J021125.0-401728.6 with an offset of 1.425 arcminutes on the top and 1.3125 arcminutes on the right, on the top left is the corrected image. On the bottom left XMMXCS J060553.7-351808.5 with an offset of 2.025 arcminutes on the top, on the bottom right is the corrected image.

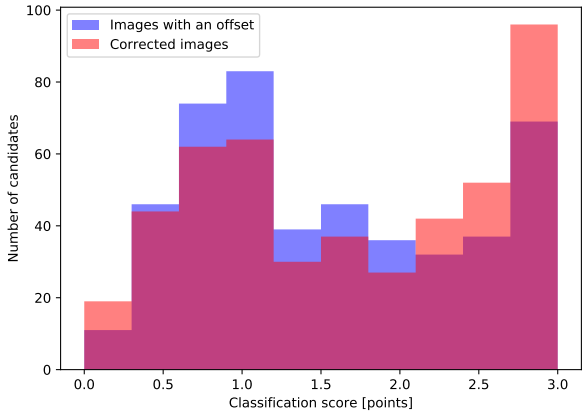

Figure 3.7: Classification scores for the main Zoo exercise which contained optical images with an offset (in blue), compared to the to the same images with the offset correction (in red).

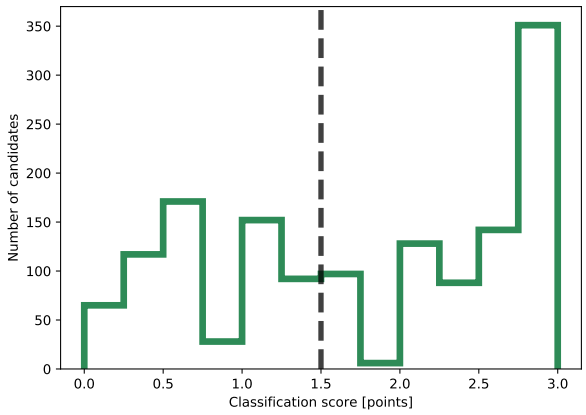

Figure 3.8: Final classification scores for the total DES-XCS Zoo exercise. Only candidates with a classification score higher than 1.5 (black dashed line) were included in the next step of the analysis.

During the Zoo exercise, I found that the optical images of subjects near the edge of a DES tile were offset from their true positions. For example, if the position of a subject was one arcminute from the edge of the DES tile (on any direction), the cutout server would produce fits images (for each of the bands) with an offset of one arcminute from the true position in the direction to the edge of the tile (see for example Fig. 3.6). This offset was found in 473 images and led to confusion among the participants, who based their classification on the X-ray information only. This issue was rectified by DESDM, by making stripes rather than co-adding across tiles. As a consequence, a new Zoo project using these new images was made for the 473 affected sources. Figure 3.7 shows a comparison between the the classification scores of the same images with (blue) and without (red) the offset, demonstrating how determinant is the use of the optical image when classifying cluster candidates. The scores from this second Zoo sub-exercise were taken into account for this set of objects.

3.4.2 Results and final inspection

Recalling Section 3.2, more specifically Table 3.1, the total number of XCS DR2 cluster candidates in the DES Y3 area with more than 200 photon counts in the X-ray soft band (0.5 - 2.5 keV) was 2,082 candidates, with 566 of them having been classified as extended but with a PSF-size flag. Of these 566 candidates with PSF flags that went through this first inspection, only 166 ($\sim$ 11.35%) were approved and included to the final classification exercise. Also, 131 further sources were discarded for being erroneous detections by XAPA. In total, 1,551

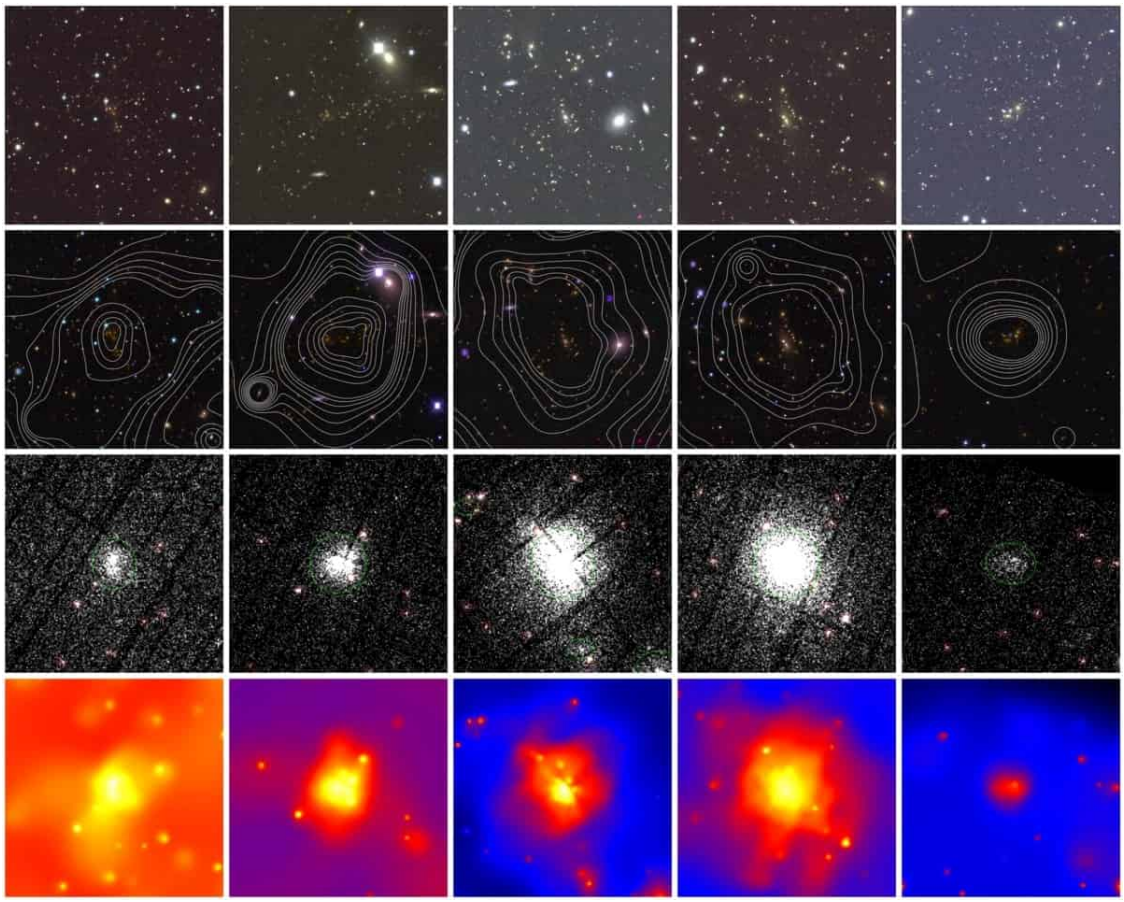

Figure 3.9: Examples of subjects classified definitely as clusters with a score of 3.0 during the Zoo exercise. From left to right: XMMXCS J202208.8-632400.1, XMMXCS J003426.9+022523.1, XMMXCS J022553.4-415448.4, XMMXCS J210418.5-412037.2, XMMXCS J021529.0-044052.8.

candidates entered the main DES-XCS Zoo project resulting in;

- 493 candidates with a score in the range (2.5 - 3.0),
- 216 candidates with a score in the range (2.0 - 2.5), and
- 103 candidates with a score in the range (1.5 - 2.0).

Obtaining in total 812 candidates from the Zoo exercise as shown in Figure 3.8. After this, a final inspection was made by myself and K. Romer. For this process, another Zoo project was made, with the central question being if a subject should or should not be removed from the definite cluster sample (together with the same set of images as the previous Zoo). This resulted in a further 103 objects being rejected, leaving a final sample of 709 from the classification stage. To this final sample were added 13 clusters that did not pass the Zoo exercise but are optically confirmed clusters in other catalogues: 2 from the Planck Collaboration (Ade et al., 2016), 3 from XXL (Pacaud et al., 2015), 3 from the South Pole Telescope (Bleem et al., 2014), and 5 from XCS-DR1 (Mehrtens et al., 2012). The final catalogue contains 722 optically confirmed XCS clusters in the DES Y3 footprint. A density map of the positions of these clusters is shown in Figure 3.10.

The final numbers of the Zoo exercise revealed two things. The percentage of objects included in the sample, out of the total number of objects that exist in other catalogues and should have been included given the selection criteria, was 98.2% according to the numbers above. However, the percentage of objects in the sample that were mistakenly included, given the selection criteria, is 12.6%. This means that (roughly), one in ten clusters was classified incorrectly in the Zoo exercise. This means that the Zoo exercise resulted in a sample with a high estimated level of completeness but with a certain amount of contamination. In comparison, the XCS-SDSS catalogue (see Sec. 3.8.2) has a lower estimated level of completeness (94.3%) but with a lower amount of contamination (4.6%). Since the classification method was tested and considered reliable (see Sec. 3.8.2), the difference in the contamination percentages can be attributed to the people involved in the classification process. The contamination percentage could be reduced by increasing the number of classifications, specially for subjects near the 1.5 threshold in Figure 3.8. I consider this exercise to be successful nonetheless.

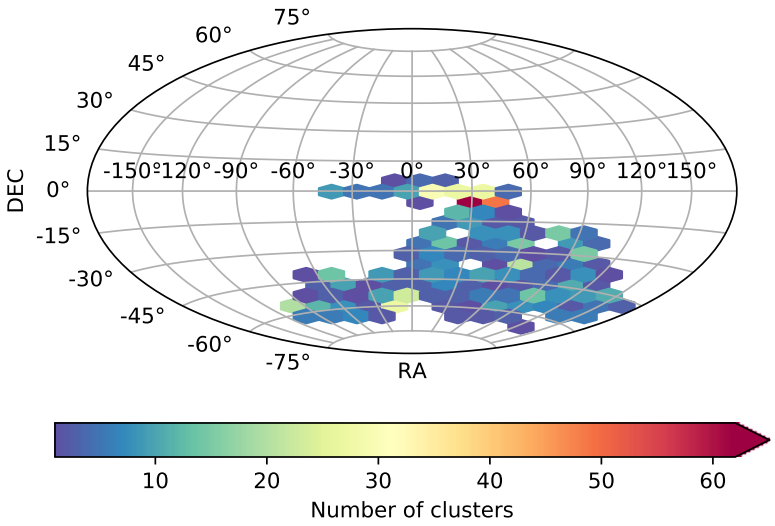

Figure 3.10: The Hammer projection of the DES-XCS density distribution clusters in the sky.

3.5 Serendipitous detections in XCS

Is important to mention that the vast majority of clusters within the XMM observations are serendipitous. For the most part, clusters are found in the outskirts of these observations rather than being the intended target of the ObsID (see Fig. 3.11). A threshold was applied to find the number of serendipitous clusters in the DES-XCS sample. To do this, I calculated the distance from the XAPA centre to the nominal aim-point position and separated the clusters into two groups provisionally: targets if ($< 3'$) or serendipitous if ($> 3'$). Subsequently, a visual check of the objects was necessary to; (i) exclude highly extended clusters at low-redshift; (ii) identify cases of extended sources that are physically associated with a target source, e.g if both bodies belong to the same system. These type of objects are common examples of non-serendipitous cases that have an off-axis angle $> 3'$. Other target filters for the sample included the inspection of each object's position against the ObsID file header and automated queries in the NASA/IPAC Extragalactic Database (NED)[2]. The sample contained 246 clusters with off-axis $< 3'$, with 164 of these happening to be targets. Conversely, 606 clusters had off-axis $> 3'$ with 32 of them being targets. Therefore, I found that in total, 534 of the 722 clusters in XCS-DES sample were serendipitously detected by XCS.

[2]https://ned.ipac.caltech.edu/

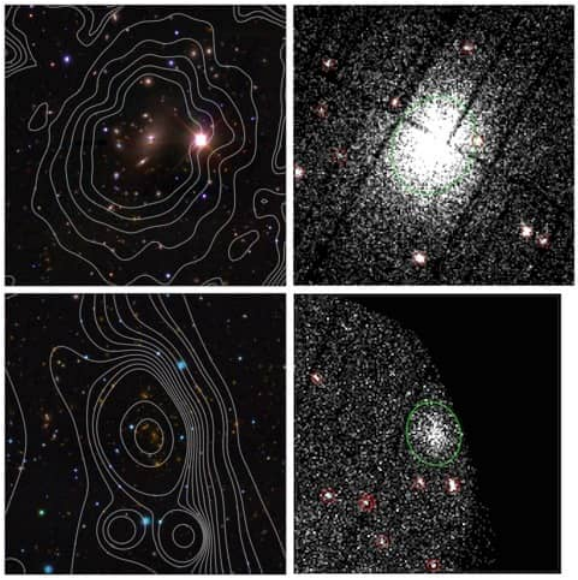

Figure 3.11: On the top row, the optical and X-ray images of an example of the target cluster XMMXCS J023142.5-045254.5. On the bottomm the optical and X-ray images of the serendipitous cluster XMMXCSJ203827.5-561443.3 found in an XMM observation.

3.6 Assigning cluster redshifts

Most of the redshifts for the DES-XCS clusters were acquired from the redMaPPer catalogue, more specifically the Y1A2 catalogue version 6.4.21 (see Sec. 2.5). I cross-matched the redMaPPer catalogue with my DES-XCS cluster sample. I assumed that all physical matches would occur within 1.5 Mpc of the redMaPPer centre and the X-ray source was at the redMaPPer redshift. The cross-matching procedure resulted in 398 matches between both surveys. Some of the DES-XCS clusters had already assigned redshifts in other cluster samples known to my research group: 69 from XCS-DR1 (Mehrtens et al., 2016), 55 from the South Pole Telescope (Bleem et al., 2014), 47 from XXL (Pacaud et al., 2015), 34 from the Planck Collaboration, and 9 from the multiband photometric redshift estimator, `zCluster` (Hilton et al., 2017).

In addition, to using RM redshifts, all 722 DES-XCS cluster positions were checked against the NED repository in order to mine redshifts from the literature. Literature redshifts were available for a small fraction of the candidates, but were nonetheless useful for comparison to other redshift sources, e.g. RM. In an initial search, I extracted all sources, classified as either a galaxy or a cluster, within a 30-arcsec search radius of the candidate centroid using the large batch query. In total, 335 of the clusters were found in NED, of which 147 had redshifts cat-

Cluster Catalogue (Reference)	No. of clusters
redMaPPer (Rykoff et al., 2016)	398
XCS-DR1 (Mehrtens et al., 2012)	69
NED (https://ned.ipac.caltech.edu/)	60
South Pole Telescope (Bleem et al., 2014)	55
XXL100 (Pacaud et al., 2015)	47
Planck Collaboration (Ade et al., 2014)	34
`zCluster` (Hilton et al., 2017)	9
Total	672

Table 3.2: Number of clusters with assigned redshifts from different literature sources.

egorized as photometric or spectroscopic in this database. However I found, through visual inspections of the associated X-ray observations, that some matches were wrong, i.e. the selected NED object and/or its corresponding redshift was not physically associated with the DES-XCS cluster. This happened to be especially true at low NED redshifts, where the allowed matching radius is larger. Other redshifts were obtained from other literature sources using a similar process. Table 3.2 shows the number of clusters with redshifts from different public catalogues, these redshifts are distinct with no repeats between the samples. In total, 672 clusters from DES-XCS have associated redshifts (93% of the whole sample).

3.6.1 redMaPPer clusters left out of DES-XCS

Not all of the redMapper clusters are expected to have counterparts in my DES-XCS sample, regardless of being in overlapping footprints, because of one of these reasons (i) the different cluster finding methodologies employed by both surveys, (ii) the respective DES-XCS cluster having a low XMM exposure time and/or high background, (iii) the redMaPPer cluster falling on the edge of the field of view of the XMM observation and/or in an EPIC chip gap, (iv) XAPA failing to detect a high S/N extended source (in this case, a second XAPA run usually correctly identifies the source), or (v) the redMaPPer cluster was identified as a point source by XAPA.

There are $\simeq$500 DES Y3 redMaPPer clusters in the XCS footprint that did not pass the various cuts described in Section 3.2 and Section 3.4.1. However, only 71 (14%) of these

sources have high enough richness ($\lambda > 20$) to be included in the volume limited sample (Rykoff et al., 2014). As explained in Section 2.5, the richness estimate λ is the sum over the membership probabilities of all galaxies within a predefined projected radius. A low value of λ implies a lower probability that the observed colour-distribution of likely members matches the self-calibrated red-sequence model of redMaPPer. Thus, a lower probability that the source is actually a cluster, as confirmed by a follow-up optical inspection of the 500 objects.

3.7 Measurement of X-ray properties

The XCS3P pipeline (see Sec. 2.2.4) was applied to all clusters with an associated redshift. Reliable (i.e with $C_v < 0.25$) T_X's and L_X's were this measured for 576 clusters. The rest of the clusters either did not have a very good signal-to-noise XMM detection or a very high signal-to-noise XMM detection but very low redshift. The latter are problematic because XAPA often breaks single clusters into multiple sources, which then have background regions that fall inside the cluster itself. The L_X and T_X distributions are plotted in Figure 3.12 with redshift for the DES-XCS sample. The selection function of XCS is evident in the right panel of Figure 3.12, i.e. its ability to detect low luminosity clusters (particularly above the XCS minimum count detection threshold) decreases with increasing redshift.

3.8 The DES-XCS catalogue

The DES-XCS cluster catalogue, a subset of the second data release from XCS in the DES footprint, contains 722 optically confirmed galaxy cluster 672 of them have associated redshifts, and 576 have calculated T_X and L_X using the latest version of XCS3P. The redshift mean is 0.3761, the temperatures and luminosities measured according to these redshifts are within the range (0.45 - 11.53 keV) with a median of 3.68 keV and $(5.4 \times 10^{-4} - 2.41 \times 10^{2}) \times 10^{44}$ erg/s with a mean of 5.26×10^{44} erg/s respectively. Further characterization of the catalogue can be found in Table 3.3 for different redshift ranges.

Redshift range	N	$\langle z \rangle$	$\langle T_X \rangle$ [keV]	$\langle L_X \rangle [10^{44} \mathrm{erg/s}]$	$\langle$counts$\rangle$
[0.00762 - 0.1]	50	0.05	3.16	1.10	26,919
(0.1 - 0.2]	106	0.14	3.03	1.62	23,325
(0.2 - 0.4]	197	0.22	3.35	3.44	15,432
(0.4 - 0.8]	174	0.54	4.06	6.53	4,571
(0.8 - 1.53]	49	0.93	4.66	13.77	4,179

Table 3.3: Characterization of the DES-XCS catalogue, the number of clusters, average redshift, average X-ray temperature, average X-ray luminosity, and average photon counts are given for each redshift bin.

3.8.1 High temperature and high redshift clusters

- **High T_X clusters**. Mehrtens et al. (2012) defines high temperature clusters to those that have $T_X > 5$ keV. These type of clusters can be detected through the SZ effect using the current generation of instruments. The DES-XCS sample contains 130 (24%) high temperature clusters in the redshift range ($0.0442 \leq z \leq 1.322$). With X-ray temperatures of $5 \leq T_X \leq 13.18$ keV and luminosities of $0.015 \leq L_X \leq 241.45 \times 10^{44}$ erg/s. In comparison to other XCS releases (see Sec. 2.2.5), this sub-set is similar in size to that of XCS-DR1 (128 clusters with $T_X > 5$ keV), but smaller to that of XCS-SDSS (194 clusters with $T_X > 5$ keV).

- **High redshift clusters**. Mehrtens et al. (2012) defines objects with $z \geq 0.8$ to be "high-redshift". Clusters at this distance are particularly useful for studies of galaxy evolution in clusters. In total, there are 49 (9%) clusters in the redshift range ($0.8 \leq z \leq 1.53$). With $(1.24 \leq T_X \leq 10.8)$ keV and $(0.138 \leq L_X \leq 241.48) \times 10^{44}$ erg/s. By comparison, there are 30 $z > 0.8$ clusters in XCS-DR1, and 23 in XCS-SDSS.

3.8.2 The second XCS data release in the SDSS DR13 footprint

The SDSS–XCSDR2 (XCS-SDSS) (Manolopoulou et al., 2017), briefly described in Section 3.8.3, is a subset of the second XCS data release that coincides with the SDSS DR13 footprint (see Sec. 2.4). The construction of this catalogue was lead by PhD student M. Manolopoulou (University of Edinburgh). Manolopoulou and I worked in parallel on the two XCSDR2 catalogues. She adopted the methodology for cluster candidate selection that I developed

for XCS-DES (and as described in Sec. 3.4.1).

In total, 12,920 XCS cluster candidates with more than 200 counts in the X-ray soft band were detected in the SDSS DR13 region. 4,622 of these candidates were identified as either extended or PSF-size by XAPA (see Sec. 2.2.3). Of the 1,384 PSF-size flagged sources, only 268 were selected as true cluster candidates. The final sample that entered the main Zoo exercise contained 3,074 sources. The analysis of the Zoo results led to 1,255 optically confirmed clusters in the SDSS DR13 region. In order to validate the methodology employed to classify the SDSS images, a second classification exercise took place using images from the Hyper Suprime-Cam of the Subaru Telescope (Aihara et al., 2014). This second exercise included 154 cluster candidates in the overlapping region with SDSS, the results showed a similar classification score for 145 (94%) clusters. This outcome showed the reliability of the classification method described in Section 3.4.1. To determine whether a cluster was found serendipitously or not by XCS, I carried out the same procedure depicted in Section 3.5. In total 903 (with 98% of clusters at an off-axis position >3') of the 1,255 clusters in XCS-SDSS sample were serendipitously detected by XCS.

I derived the X-ray spectral properties of the XCS-SDSS clusters using the updated version of XCS3P (see Sec. 2.2.4). Only 82 of the 1,225 clusters with redshifts did not run successfully through XCS3P, leaving 1,143 clusters (93% of the whole sample) with T_X and L_X measurements. As referred to in Section 2.2.4, some of the reasons why a cluster might not have a measured T_X and L_X include a low signal-to-noise XMM detection, or a very high signal-to-noise detection but low redshift.

Properties

In summary, the catalogue contains:

- 1,255 optically confirmed clusters, of which 203 have never been catalogued as an X-ray cluster detection before and 903 are serendipitous detections.

- Almost all of the clusters have associated redshifts: 931 have spectroscopic redshifts from SDSS, 160 have GMPhoRCC(Hood and Mann, 2017) redshifts, 117 have spectroscopic redshifts taken from the literature, 6 have `zCluster` redshifts and 11 have photometric redshifts taken from the litarature. The redshifts range extends out to $\sim$ 1.2 with a median of 0.28. In total, 1,225 of my clusters have associated redshifts, either

spectroscopic or photometric.

- 1,143 clusters have calculated X-ray temperature and luminosity values. A cut in temperature of $T_X > 5$ keV was made. The subsample contained 194 clusters within the redshift range ($0.037 \leq z \leq 1.169$) with $5.0 < T_X < 13.8$ [keV] and $4.1 \times 10^{-3} < L_X < 8.8 \times 10^{1}[10^{44}$ erg/s].

- 1,223 clusters have an estimated richness value from GMPhoRCC.

Further details about the catalogue and its applications can be found in (Manolopoulou, 2019).

3.8.3 Comparison to previous XCS Catalogues

I compared the DES-XCS sample to the first XCS data release and XCS-SDSS sample in terms of number of clusters, X-ray luminosities, and redshifts. The panels of Figure 3.12 show the comparison of the redshifts for each of the different XCS catalogues, it can be seen that the XCS-DES has a relevant contribution of clusters at high-redshift (i.e. for $0.7 < z < 1.0$), where DES has proven to provide reliable imaging for cluster finding. In Figure 3.12, the histograms for the X-ray temperature and luminosity distributions of the DEX-XCS sample (in blue) is compared to that from XCS-DR1 (in red) and XCS-SDSS (in yellow).

3.9 Scaling relations

In this section I present the scaling relations of the DES-XCS cluster catalogue. For this study, I used the 684 clusters that had reliable core excised T_X and L_X measurements, i.e. with an average error lower than 25% and $z \geq 0.1$ (see Sec. 2.2.4). For the optical to X-ray scaling relations, I used a subsample of 220 clusters with optical richness ($\lambda > 20$) from redMaPPer (see Sec. 2.5). The model used to fit the $T_X - L_X$, $T_X - \lambda$ and $L_X - \lambda$ scaling relations is based on the linear regression model.

Given a data set $y_i, x_{i1}, x_{i2}, ..., x_{in}{}_{i=1}^{n}$ of n statistical units, a linear regression model assumes a linear relationship between the dependent variable y and the $p-$vector of regressors x. The relationship is modeled through a disturbance term or error variable ϵ an unobserved random variable that adds noise to the linear relationship between the dependent variable and regressors. The model takes the form

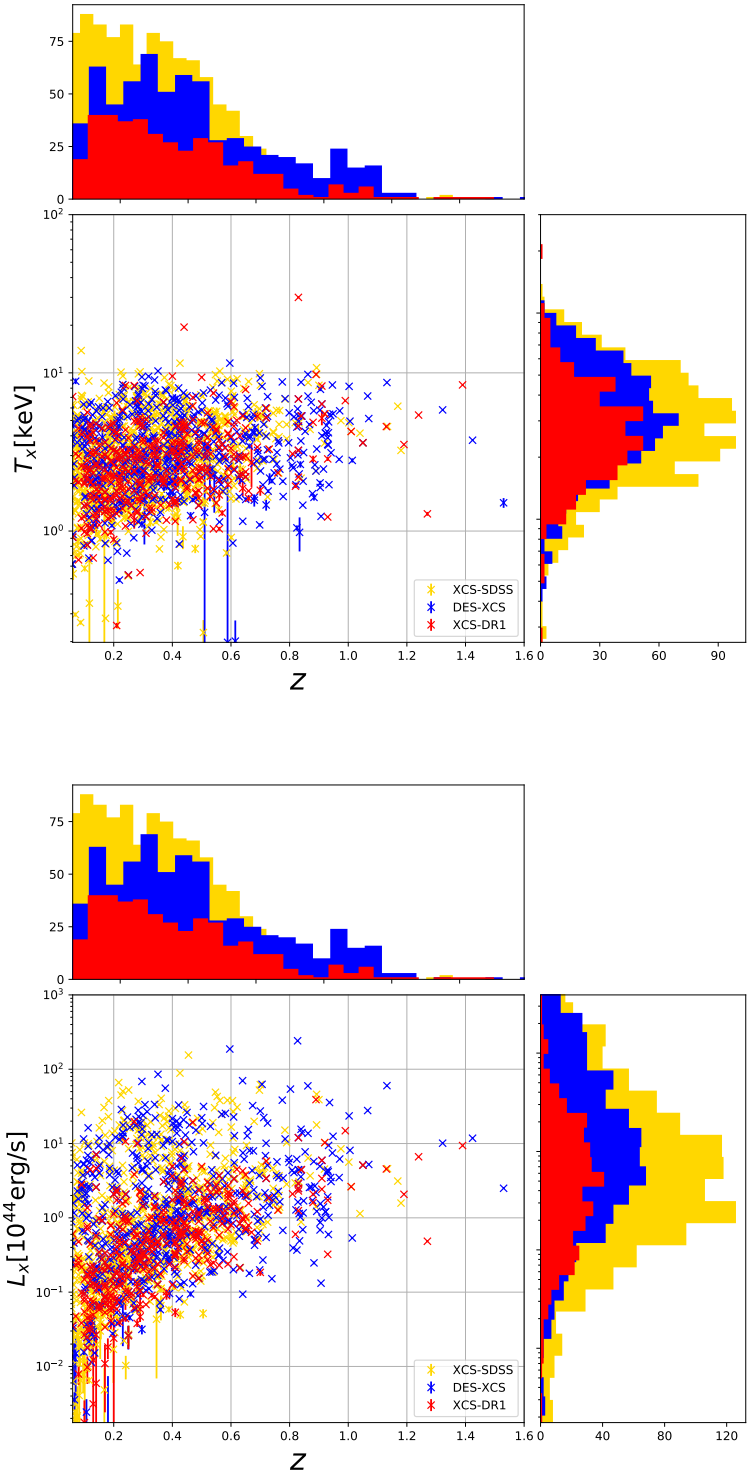

Figure 3.12: X-ray temperature (left panel) and X-ray bolometric luminosity (right panel) distribution of DES-XCS clusters in blue, XCS-DR1 in red, and XCS-SDSS in yellow. At the top and on the right of each image are the projected quantities z, T_X and z, L_X respectively for each image.

$$y_i(x_i) = \beta_0 + \beta_1 x_{i1} + \beta_2 x_{i2} + ... + \beta_p x_{ip} + \epsilon = x_i^T \beta + \epsilon, \qquad i = 1, ..., n. \tag{3.1}$$

For the scaling relations I worked with, Equation 3.1 can be reduced to to fit a line of the form

$$y_i(x_i) = \beta_0 + \beta_1 x_i + \epsilon_i, \tag{3.2}$$

with β_0 the intercept and β_1 the slope of the fitting line respectively. A value close to zero indicate little to no relationship, large positive or negative values indicate large positive or negative relationships, respectively. The residual error (or noise) ϵ_i represents the fact that the data will not fit perfectly. In order to minimize the residual error a common approach (Im, 1996) is to define a function $J = J(\beta_0, \beta_1)$ given by

$$J(\beta_0, \beta_1) = \frac{1}{2n} \sum_{i=1}^{n} \epsilon_i^2 \tag{3.3}$$

which has a minimum when

$$\beta_1 = \frac{\sum_{i=1}^{n}(x_i - \bar{x})(y_i - \bar{y})}{\sum_{i=1}^{n}(x_i - \bar{x})^2}, \qquad \beta_0 = \hat{y} - \beta_1 \bar{x}. \tag{3.4}$$

3.9.1 The Temperature - Luminosity relation

In the case of the $T_X - L_X$ relation, Equation 3.2 is given then by

$$\ln(T_X) = \beta_0 + \beta_1 \ln(L_X), \tag{3.5}$$

which for the DES-XCS subsample is

$$\ln(T_X) = 1.119^{+0.01}_{-0.01} + 0.258^{+0.005}_{-0.005} \ln(L_X). \tag{3.6}$$

The plot of the $T_X - L_X$ is shown in Figure 3.13. The thick line represents the fitting described by Equation 3.6 along with its 95% confidence interval for the regression. The sample was split into different redshift bins: $z \in (0.007, 0.25]$ in purple, $z \in (0.25, 0.5)$ in black, and $z \in [0.5, 1.4)$ in teal.

As shown in Figure 3.13, there are 24 clusters lying outside the 95% confidence level region, i.e. over 5σ) from the best fit of the $T_X - L_X$ relation. Even if these clusters have been

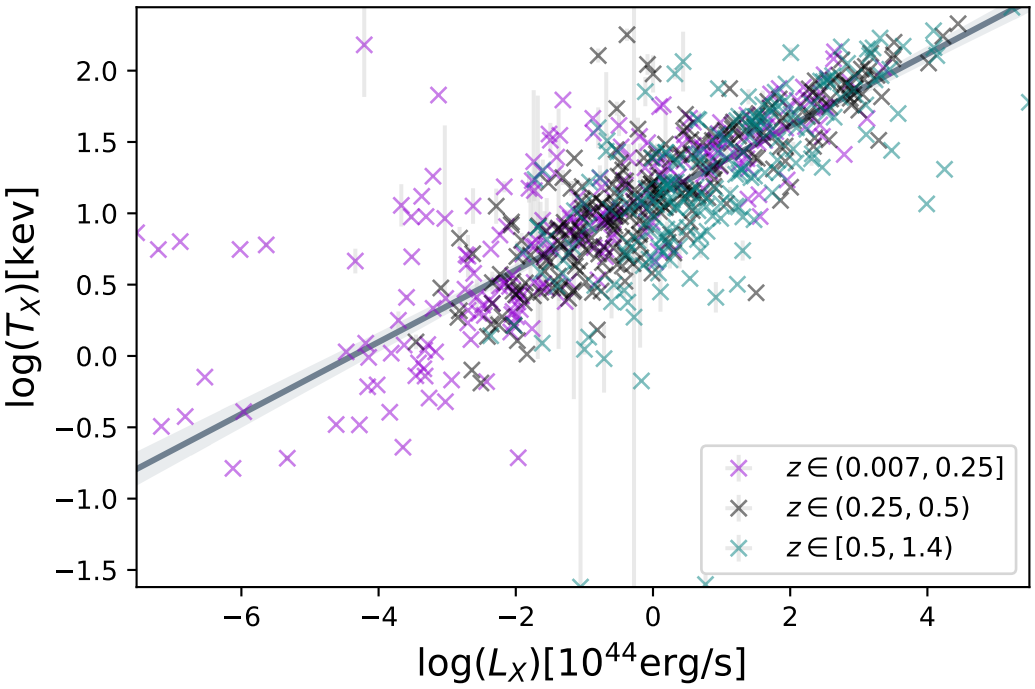

Figure 3.13: The X-ray temperature (T_X) - luminosity (L_X) scaling relation for the DES-XCS sample split into different redshift bins: $z \in (0.007, 0.25]$ in purple, $z \in (0.25, 0.5)$ in black, and $z \in [0.5, 1.4)$ in teal. The line of best fit is shown with the thick grey line along with its 95% confidence interval for the regression.

weighted out during the linear regression analysis, it is important to determine whether there is any kind of underlying issue with the data/analysis of the XMM data or the DES images. In total, 79% of these outliers are serendipitous detections (see Sec. 3.5), and all of them have been catalogued before in the literature: 12 by redMaPPer (see Sec. 2.5), 10 are associated with a source found in NED[3], 1 by XCS-DR1 (see Sec. 3.8.3), and 1 by Planck (Ade et al., 2016). I found that 17 (71%) of these clusters had a number of photon counts lower than 1,000 with 13 (76%) within the redshift range of $0.2 < z < 0.8$. With this information, and after a quick optical inspection, I discovered that most of these clusters have not a very good signal-to-noise ratio, making their X-ray temperature measurement unreliable. This means that these clusters will require a longer exposure in order to extract reliable X-ray information. On the other hand, the 7 (29%) clusters with a number of photon counts larger than 1,000, all but one were at low redshift (i.e. $z < 0.2$). Most of these clusters are so extended in the XMM observation that it makes hard for XCS3P (see Sec. 2.2.4) to determine their region aperture for spectral extraction, making their X-ray temperature measurement unreliable. Figure 3.14 shows some examples of the aforementioned type of sources. From left to right: cluster XMMXCS J232835.7-534916.2 is a high redshift ($z = 0.87$) serendipitous cluster with a low signal to noise; XMMXCS J005558.2-373300.0 lies too close to the edge of the field of view; XMMXCS J022318.6-052708.2 is a low redshift ($z = 0.21$) serendipitous cluster with a low signal to noise; XMMXCS J062616.8-534207.9 is a low redshift ($z = 0.049$) highly extended target cluster.

The X-ray temperature (T_X) - luminosity (L_X) scaling relation was also calculated for the XCS-DR1 sample, which is

$$\ln\left(T_X\right) = 1.132^{+0.02}_{-0.02} + 0.260^{+0.01}_{-0.01}\ln\left(L_X\right). \tag{3.7}$$

and for the XCS-SDSS sample, which is

$$\ln\left(T_X\right) = 1.131^{+0.01}_{-0.01} + 0.273^{+0.007}_{-0.007}\ln\left(L_X\right). \tag{3.8}$$

I compared the fit shown in Figure 3.13 to the ones from the first data release of XCS and the XCS-SDSS catalogue. The plot of the comparison between the XCS-DR1 (red) and the DES-XCS (blue) $T_X - L_X$ relations is shown in Figure 3.15(a). The light red region represents

[3]https://ned.ipac.caltech.edu/

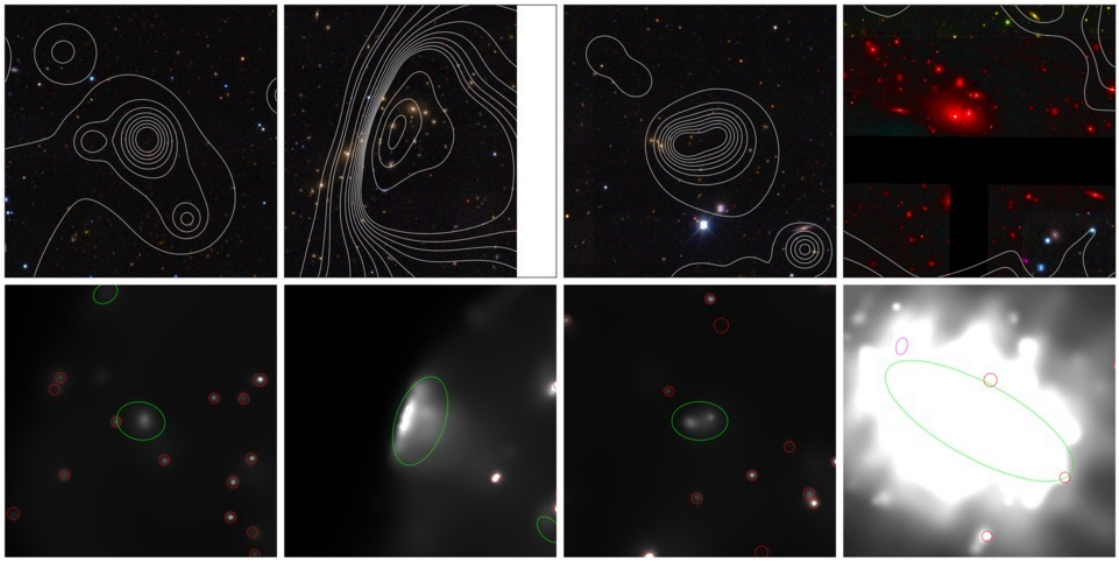

Figure 3.14: Examples of sources in DES-XCS lying far out of the 95% confidence region of Figure 3.13. Their corresponding optical images (with data taken from DES) with X-ray contours (with data taken from XCS) are shown (top) and their X-ray images (bottom). From left to right: XMMXCS J232835.7-534916.2, XMMXCS J005558.2-373300.0, XMMXCS J022318.6-052708.2, XMMXCS J062616.8-534207.9.

the 95% confidence interval for the regression for the XCS-DR1 sample, while the light blue region represents a similar value but for the DES-XCS sample. The plot of the comparison between the XCS-SDSS (yellow) and the DES-XCS (blue) $T_X - L_X$ relations is shown in Figure 3.15(b). The light yellow area represents the 95% confidence interval for the regression, while the light blue region represents a similar value but for the DES-XCS sample.

3.9.2 The X-ray observable - Richness relations

In the case of the $T_X - \lambda$ relation, Equation 3.2 is given by

$$\ln(T_X) = \beta_0 + \beta_1 \ln(\lambda) \tag{3.9}$$

which for the DES-XCS subsample is

$$\ln(T_X) = 0.83^{+0.04}_{-0.04} + 0.008^{+0.001}_{-0.001} \ln(\lambda). \tag{3.10}$$

The plot of the $T_X - \lambda$ is shown in Figure 3.16 (left), the thick line represents the fitting described by Equation 3.10, the grey region represents 95% confidence interval for the regression.

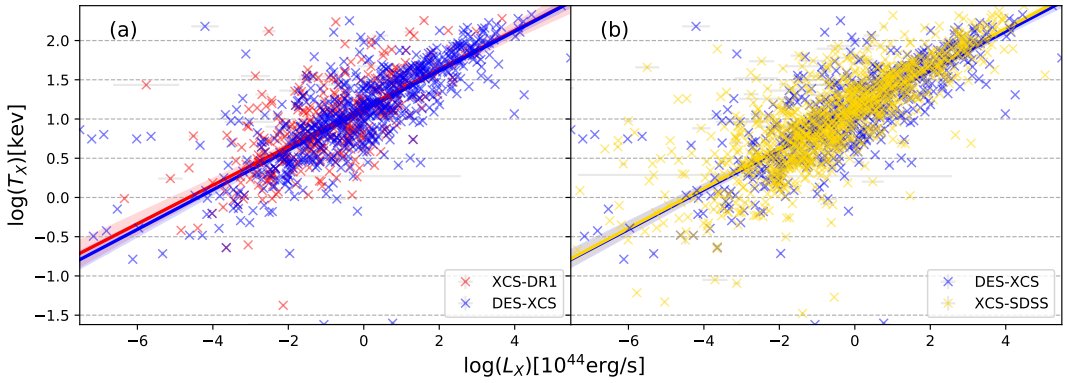

Figure 3.15: The X-ray temperature - luminosity scaling relation for the XCS-DR1 sample from Mehrtens et al. (2012) in (a) and the XCS-SDSS sample from (Manolopoulou et al., 2017) in (b), given by Equation 3.7 and Equation 3.8 respectively, compared to the DES-XCS sample.

In the case of the $L_X - \lambda$ relation, Equation 3.2 is given by

$$\ln(L_X) = \beta_0 + \beta \ln(\lambda) \tag{3.11}$$

which for the DES-XCS subsample is

$$\ln(L_X) = -0.73^{+0.13}_{-0.13} + 0.024^{+0.002}_{-0.002} \ln(\lambda). \tag{3.12}$$

The plot of the $L_X - \lambda$ relation is shown in Figure 3.16 (right). The thick line represents the fitting described by Equation 3.10, the grey region represents 95% confidence interval for the regression.

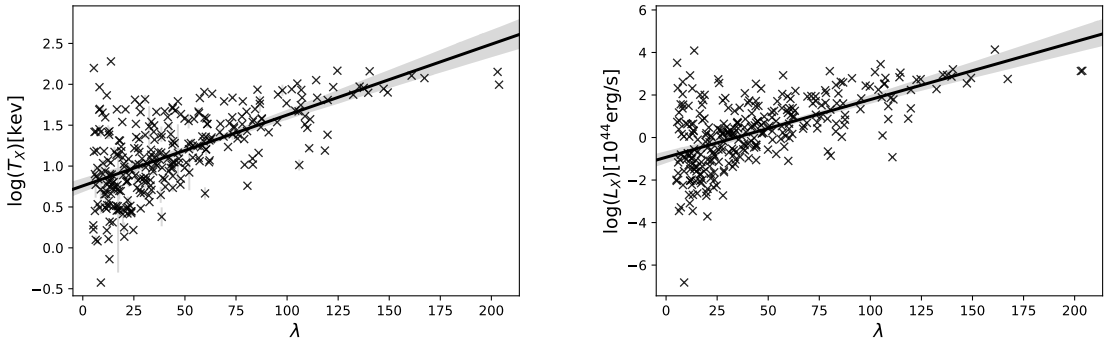

Figure 3.16: *Left*: optical to X-ray scaling relation between optical richness (λ) and X-ray temperature (T_X). *Right*: Optical to X-ray scaling relation between optical richness (λ) and X-ray luminosity (L_X).

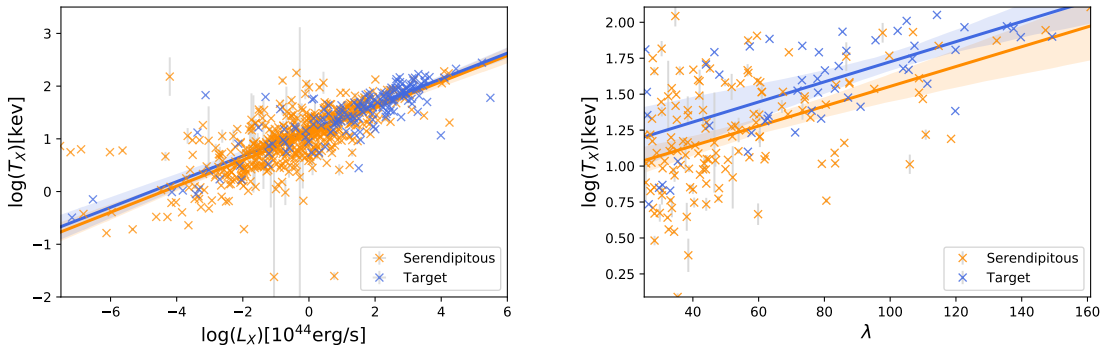

Figure 3.17: *Left*: The X-ray temperature (T_X) - luminosity (L_X) scaling relation for the targeted (blue) and serendipitously (orange) detected clusters respectively. *Right*: The X-ray temperature (T_X) - luminosity (L_X) scaling relation for the targeted (blue) and serendipitously (orange) detected clusters respectively.

3.9.3 Targeted vs Serendipitous clusters

I separated the DES-XCS cluster sample into serendipitously and targeted detected clusters and remade the scaling relations from the previous section. The results of the $T_X - L_X$ relation for these two subsets of clusters are given by

$$\ln(T_X) = 1.19^{+0.02}_{-0.02} + 0.220^{+0.01}_{-0.01} \ln(L_X). \tag{3.13}$$

for the targeted clusters and

$$\ln(T_X) = 1.08^{+0.01}_{-0.01} + 0.222^{+0.01}_{-0.01} \ln(L_X). \tag{3.14}$$

The plot with the comparison between the targeted (blue) and the serendipitously (orange) $T_X - L_X$ relations is shown in Figure 3.17. The blue and orange areas represent the 95% confidence interval for the regression for the targeted and serendipitous clusters respectively.

In the case of the $T_X - \lambda$ relation, the results are given by

$$\ln(T_X) = 1.02^{+0.16}_{-0.16} + 0.0068^{+0.04}_{-0.04} \ln(\lambda). \tag{3.15}$$

for the targeted clusters and

$$\ln(T_X) = 0.84^{+0.1}_{-0.1} + 0.0067^{+0.03}_{-0.03} \ln(L_X). \tag{3.16}$$

for the serendipitous clusters.

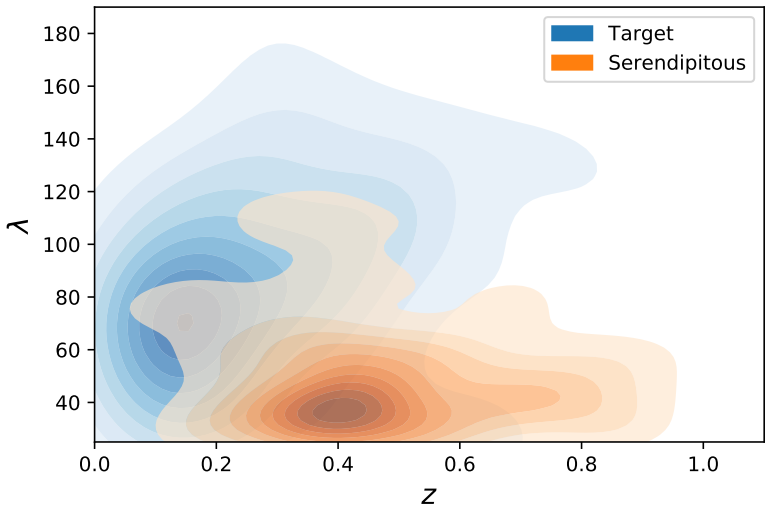

Figure 3.18: Richness distribution of the DES-XCS sample as a function of redshift, split between clusters with targeted XMM observations (blue) and those detected serendipitously (orange).

The plot with the comparison between the targeted (blue) and the serendipitously (orange) $\lambda - T_X$ relations is shown in Figure 3.17. The blue and orange areas represent the 95% confidence interval for the regression for the targeted and serendipitous clusters respectively. Assuming that a targeted sample may have more 'interesting' brighter clusters, containing a higher fraction of cool-core clusters, Figure 3.17 shows that there is no significant difference between targeted and serendipitous clusters for the $T_X - L_X$ scaling relation. This was also shown by P. Giles (in prep.) and for the $T_X - \lambda$ scaling relation, even when the core of the clusters is excluded, by removing the $0 - 0.15r_{500}$ region. While for the the $T_X - \lambda$ relation this happens to be the opposite, which was also shown by P. Giles (in prep.). This could be due to the fact that serendipitous clusters may require a higher exposure in order to extract the true X-ray temperature of the cluster, as seen with all the clusters with a low richness value (λ) in Figure 3.18 which happen to be serendipitous. A further study of these objects might be required.

3.10 Conclusions

I have presented a new X-ray selected cluster catalogue of the XMM Cluster Survey covering the Dark Energy Survey Year 3 data release area. The catalogue consists of 722 optically

confirmed galaxy clusters, 534 serendipitous and 188 targeted detections. The catalogue was proved to be complete and reliable given the method I chose, I am confident that future releases of combined optical and X-ray data will yield a homogeneously selected set of confirmed X-ray clusters with increased size and completeness with a low level of contamination. I assigned redshifts, mainly from the redMaPPer cluster catalogue, and measured X-ray temperatures and bolometric (0.5 - 10 keV) luminosities using the XCS post processing pipeline.

The process of compiling the cluster catalogue started from the latest XCS master source list which contains X-ray detections in the XMM archival data. From this list I only took the sources that were in the DES Y3 area and produced images using both X-ray and optical data. After this, I led an optical classification procedure to produce a galaxy cluster catalogue which I analysed in detail. The assigned redshifts and measured X-ray properties of the sample showed a redshift mean of 0.38, temperatures within the range (0.45 - 11.53) keV and a median of 3.68 keV, and luminosities within the range $(5.4 \times 10^{-4} - 2.41 \times 10^{2}) \times 10^{44}$ erg/s with a mean of 5.26×10^{44} erg/s. I compared my sample with other cluster surveys to ensure the good quality of my catalogue. A study of the different galaxy cluster scaling relations for different subsamples was presented as well. I used linear regression to fit the scaling relation models to my data. I found that for the $T_X - L_X$ scaling relation the fits of the three different XCS data releases lie within 95% confidence interval. The comparison of the scaling relation results show that the data can be used to test cluster physics. I also found that $T_X - L_X$ scaling relation fit for the serendipitous and targeted subsamples lie within the 95% confidence interval. A brief study of the outliers in this scaling relation was done at the end of this chapter. This study is currently under preparation for publication in a scientific journal.

3.10.1 Future work

The work presented in this chapter sets a precedent of the study of the second data release of XCS. The method of creating downsampled images from the DES Y3 release from the g, r, i bands, described in Section 3.3, which was broadly followed in the creation of the second XCS data release in the SDSS DR13. I feel confident of having laid ground in the search of of X-ray clusters with future DES releases.

The XCS team has recently started working on validating the redMaPPer catalogues by

checking masks and completeness against the XCS catalogues and also by checking for missing clusters in XCS. Future work includes the use of 30k classified extended sources on 2k confirmed clusters to develop a selection function for the XCS catalogues via an analytical and machine learning approach using Deep Convolutional Neural Networks.

Chapter 4

Constraining MoG Theories with Galaxy Clusters

4.1 Overview

In this chapter I explain the process of constraining modified theories of gravity (MOG) using stacked profiles of galaxy clusters. Section 4.2 describes how the galaxy cluster sample of Wilcox et al. (2015) was developed. The methodology to generate a stacked X-ray surface brightness and a stacked weak lensing profile using CFHTLenS data is described in Section 4.3. I apply this method first to the original sample from Wilcox et al. (2015) (Section 4.2) to replicate its results. In Section 4.4.1, I explain how to simultaneously fit modified gravity models to these stacked profiles by employing Markov chain Monte Carlo (MCMC) methods. The reproduced results of Wilcox et al. (2015) are shown in Section 4.4. I finish this chapter by developing a larger and improved sample of clusters, compared to the one used in Wilcox et al. (2015), in the CFHTLenS footprint. The results from this different sample and its implications compared to the original sample from Wilcox et al. (2015) are presented in Section 4.5.

4.2 The galaxy cluster sample from Wilcox et al.

The list of cluster candidates from Wilcox et al. (2015) was built by searching for XMM observations within the CFHTLenS wide areas (see Sec. 2.6). Followed by a similar process to the one described in Section 2.2.2, but using a previous version of XAPA (see Sec. 2.2.3). A total

of 348 extended XMM sources, with more than 100 background subtracted photon counts, taken as a cut-off limit as the minimum photon count required to measure an X-ray temperature according to Lloyd-Davies et al. (2011), were located in the CFHTLenS fields. After an optical inspection, 186 were excluded leaving the sample with 162 candidates. Of these only 82 had redshifts, mainly from GMPhorCC (Hood and Mann, 2017). For a more detailed explanation of the aforementioned procedure see Wilcox et al. (2015). A previous version of the XCS Post Processing Pipeline (XCS3P) to the one described in Section 2.2.4 was used by the authors to derive the X-ray spectral properties of the clusters candidates. The final X-ray selected cluster sample contained 58 clusters with temperatures measured by XCS within the redshift range $0.1 < z < 1.2$ (median $z = 0.33$) and temperature range $0.2 < T_X < 8$ keV (median $T_X = 2.3$ keV).

4.3 Methodology

The method described in Wilcox et al. (2015) was proven to be robust and in agreement with simulations (Wilcox et al., 2018), as summarized in Section 1.5.5. Improvements to the methodology that I applied include updates to the software and to the X-ray analysis. One relevant change that I made was to remove all potential sources of contamination from the X-ray images during the analysis, which was not done by Wilcox et al. (2015). As covered in Chapter 2, point sources in the $(2 - 10$ keV) X-ray band correspond mainly to Active Galactic Nuclei (AGN) (Mushotzky, 1984), which have an X-ray flux that is significant enough to spoil the total X-ray flux from the cluster. This causes an overestimation of the surface brightness profile and affects the measured cluster profile. The process of removing this background sources is covered in Section 4.3.1. Also, I updated the X-ray analysis of the sources in the sample in Section 4.5, using the most recent version of the XCS pipelines.

4.3.1 Stacking X-ray surface brightness profiles

After selected their X-ray cluster sample, Wilcox et al. (2015) stacked the multiple different XMM observations for each of these clusters. The process comprised of several steps in order to build up a signal to noise in the outer parts of the ensemble cluster profile. Most of clusters in the sample were covered by more than one XMM observation using more than one camera: MOS1, MOS2, PN (see Sec. 2.2.1). The different background properties, exposure times, and

energy dependent sensitivities were taken into account for each observation and for each of the cameras during the stacking.

To subtract the background for a given cluster, I measured the number of counts on each image by placing an annulus around the source to exclude the outer region. Next, I removed the point sources by setting their pixel values to zero to then determined the number of background counts. I calculated the respective source and background areas by taking the same region sizes and setting the pixel values to one, to later sum the pixels to get the source area and background area. The cluster signal is then given by the following expression

$$\text{signal} = \text{counts}_{\text{tot}} - (\text{area}_{\text{tot}}/\text{area}_{\text{bg}}) \times \text{counts}_{\text{bg}}, \tag{4.1}$$

where area_{bg} and $\text{counts}_{\text{bg}}$ correspond to the background area and counts respectively. The motivation for this process, which was not done in Wilcox et al. (2015), is demonstrated by the PN XMM observation 0720250501 shown in Figure 4.1. The top panel shows the original observation while the bottom panel shows the same image after the background sources have been subtracted. Both images were made in the (0.50 - 2.00) keV energy band. Having the signal value, the total count rate for a cluster is given by

$$\text{count\_rate} = \text{signal} \times \text{source\_counts}/\text{exposure\_time}. \tag{4.2}$$

Each cluster was then multiplied by the specific count rate to luminosity conversion factor of each camera (for a more detailed explanation see Lloyd-Davies et al. (2011)). This procedure allowed me to combine all the images for a cluster in a consistent manner.

To generate a single stack from the cluster sample, I had to re-scale the combined images of the individual clusters to a standard size. Assuming that the clusters follow the self-similarity prediction (see Sec. 1.2.1), I rescaled the images into the same projected dimension using M_{500}. Making predictions for X-ray cluster observations requires us to model scaling relations (to relate temperature to mass) to be able to predict cluster distributions. As explained in Section 1.2.2, the X-ray temperature is one of the best mass proxy observables. The redshift dependant relationship between the X-ray temperature, T_X, and cluster mass, M_{500}, given by Equation 1.16 can be rewritten in the form

$$T_X = (M_{500}/M^*)^{2/3}(\rho_{500}(z)E^2(z))^{1/3}, \tag{4.3}$$

where $\rho_{500}(z)$ is the mean overdensity of a cluster within r_{500} with respect to the critical density (see Sec. 1.2.4), $E(z)$ is the energy density given by Equation 1.51, and $M^* = 3 \times 10^{14} h^{-1} M_{Sun}$ at $z = 0.05$ for an X-ray temperature of 5 keV. This normalization of the cluster X-ray temperature to mass relation was chosen to agree with that derived from X-ray data, according to Sahlén et al. (2009), Arnaud, Pointecouteau and Pratt (2005) and Vikhlinin et al. (2009), which reproduces the local abundance of galaxy clusters as given by astronomical catalogues in their cosmological models. Various definitions of the mass of a halo can be converted assuming a halo density profile. The general scaling function provided by Hu and Kravtsov (2002) converts M_{500} and M_{200} under the assumption of a NFW profile to better than 1% accuracy at cluster scales. I computed the M_{200} values to deduce the r_{200} radius, at which the average density is two hundred times the critical density. Next the stacked images can then be rescaled so that each of them has the same r_{200} radius (in terms of image elements/pixels) using linear interpolation. After that, I centered each of the scaled images on the source centroid as determined by XAPA and then stacked them using the process described below.

The surface brightness profiles of the individual clusters were binned into 24 equally spaced logarithmic annulus, out to a distance of $1.2 \times r_{200}$. From each of these profiles, I calculated the maximum surface brightness and this a mean value for the whole sample. I used this mean maximum to re-scale each of the individual values of the surface brightness, so the original maximum surface brightness became the maximum with the data in each bin, when I scaled them by this value. This was done as adding clusters over a range of different masses could result in a significant number of clusters lying outside from their true corresponding bin in the final stacked profile. In reality this is hard to achieve, for instance, due to the effects of the telescope PSF which can blur out the image. Since changes in one surface brightness bin affect the values in the other surface brightness bins, it is important to minimize such effect as much as possible. The stacked surface brightness profile of the 58 clusters in the (Wilcox et al., 2015) sample that I generated using this method is shown in Figure 4.2 in a 500×500 pixels sized image. To estimate bootstrap errors on the surface brightness in each pixel of the stack, I selected a subset of the 58 clusters (with replacement) with 100 re-samplings.

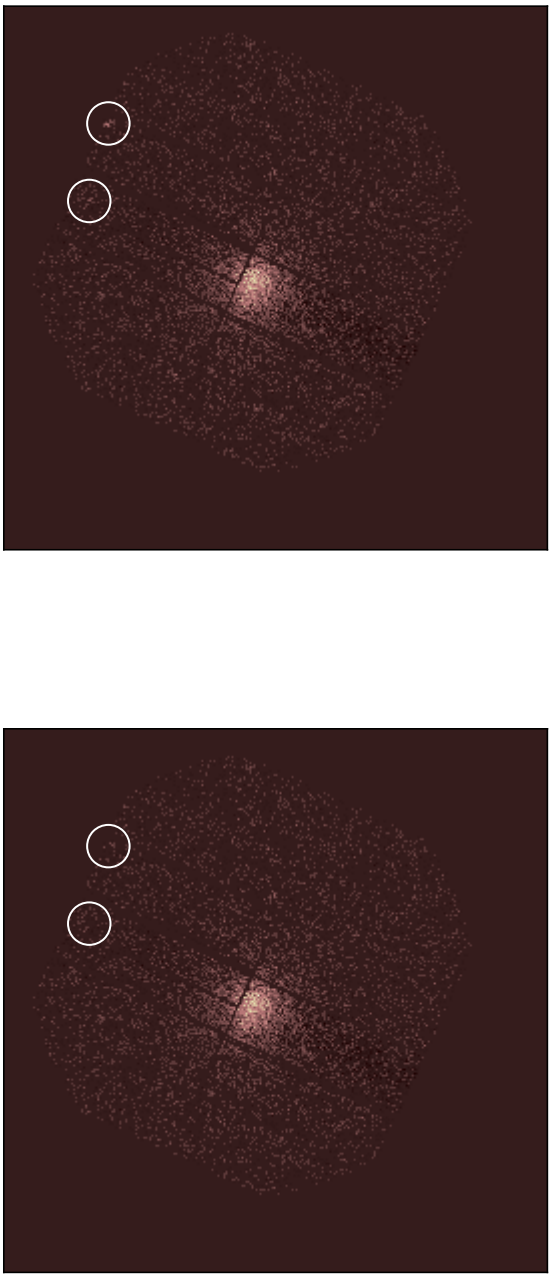

Figure 4.1: Example of the background subtraction of the PN XMM observation 0720250501 in the (0.50 - 2.00) keV. In the top panel is the original observation with two background sources encircled in white set as examples. In the bottom panel is the same image but with the background sources subtracted.

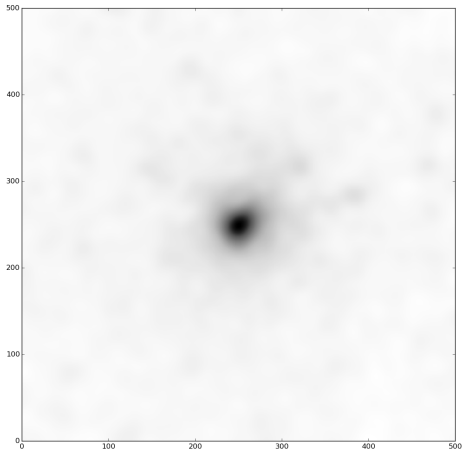

Figure 4.2: Reproduced stacked 2D surface brightness profile of the 58 cluster sample from (Wilcox et al., 2015). This 500×500 pixels sized image was made by taking the mean value of each pixel of the individual 2D surface brightnesses for each of the clusters in the sample.

4.3.2 Stacking weak lensing profiles

The stacked cluster shear profile, given by γ_t in Equation 1.36, can be built using the ellipticities (e_1 and e_2) provided by CFHTLenS (see Sec. 2.6) for each source galaxy. However, it was required to do small additive and multiplicative corrections before using the data provided by this survey. These corrections are necessary due to the biases caused by noise in the simulated data that is used to calibrate the shape measurement pipelines (see Liu, Ortiz-Vazquez and Hill (2016) for more details). The corrections were done analytically by comparing the true galaxy shapes from simulations to the measured shapes using the catalogue data in Miller et al. (2011). The additive correction, c_2, and the mean multiplicative bias correction, m, could then be calculated for each galaxy as a function of size and signal to noise with the use of

$$c_2 = \max\left(\frac{F\log_{10}(\nu_{SN} - G)}{1 + (r/r_0)^H}, 0\right), \quad m = \frac{\beta}{\log(\nu_{SN})}\exp\left(-r\alpha\nu_{SN}\right) \tag{4.4}$$

where ν_{SN} and r are the signal to noise ratio and the size of each galaxy respectively, all of these parameters are found in the CFHTLenS shear catalogue. The parameters α, β, F, G, and H are described in Heymans et al. (2012). The corrective values were applied to each galaxy in the form

$$e_{int,i} = \frac{e_i - c_{2,i}}{1 + \bar{m}}, \tag{4.5}$$

above c_2 was applied on a galaxy by galaxy basis and $\bar{m}$ is a summation of $1 + m$ for each galaxy, applied as an ensemble average to each radial bin. Each galaxy was weighted with the corresponding weight parameter from the CFHTLenS catalogue, defined as

$$w = \left(\frac{\sigma_e^2 e_{max}^2}{e_{max}^2 - 2\sigma_e^2} + \sigma_{pop}^2 \right)^{-1}, \tag{4.6}$$

with σ_e the error of a galaxies shape, e_{max} the maximum allowed ellipticity, and σ_{pop} the average error on a galaxies shape across the whole population.

I measured the tangential shear around each of the clusters and binned them into 24 equal spaced logarithmic annulus out to a distance of $10 \times r_{200}$ using Equation 1.37. The value in each bin was then rescaled using the same average mean used in the Section 4.3.1 to ensure consistency with the X-ray profiles. Finally, again in a similar way to Section 4.3.1 and in order to improve the signal to noise of the tangential profiles, I re-scaled and stacked the individual cluster profiles of the sample. I did this by adding up the profiles of each cluster to calculate the average shear in each bin across all clusters. Similar to the X-ray procedure, I calculated the average tangential shear in each bin and took as the average shear value for all the lenses. The errors on the shear profile were estimated using the same bootstrap resampling method mentioned in Section 4.3.1.

I made consistency tests of the CFHTLenS shape data to ensure that the shear profiles were unbiased as much as possible. Figure 4.3(a) shows the tangential shear (blue) and the cross shear (orange) around the 58 stacked clusters. The tangential shear is a measurement of the matter within each radial bin. Since the profile is centered on the cluster stack, a shear measurement is expected at lower radii. On the other hand, the cross shear takes constant values around zero at all radii as expected (see Sec. 1.3.2). Figure 4.3(b) shows the tangential shear of the stacked cluster sample for three bins of source galaxies with different signal to noise ratios, $S/N < 20, 20 < S/N < 40$, and $S/N > 40$. The S/N is a function of the source photon counts over the background photon counts and was taken from the CFHTLenS catalogue. Each of the bins has similar redshift distributions, with a median of 0.85, 0.82, and 0.79 respectively. The three signals are consistent with each other as expected. Figure 4.3(c) shows the tangential shear around the stacked clusters after the source galaxies

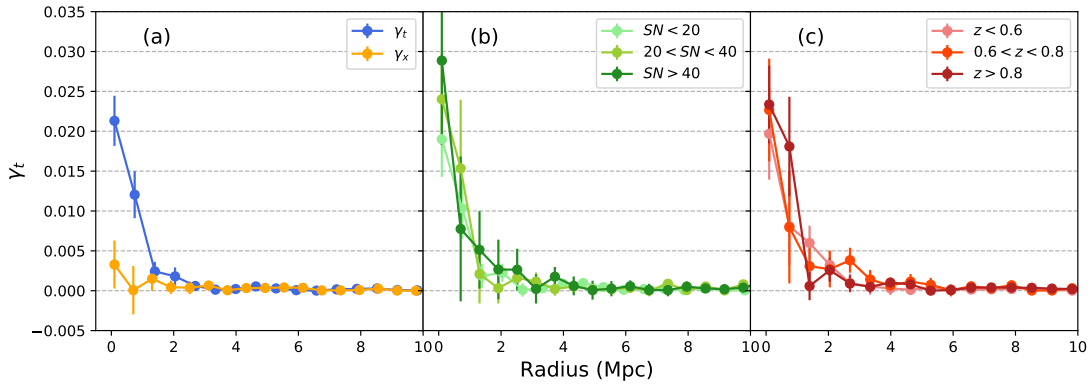

Figure 4.3: Null and consistency tests of the CFHTLenS data in binned annuli from the cluster stack centre. (a): The tangential shear around the 58 staked clusters in blue and the cross shear in orange. (b) The tangential shear around the cluster stack for three different signal to noise (S/N) bins. (c): The tangential shear around the cluster stack for three different redshifts. This figure is equivalent to Figure 1 in (Wilcox et al., 2015) but produced by me using the same data.

were split into three different bins based upon their photometric redshift, $z < 0.6, 0.6 < z < 0.8$, and $z > 0.8$. Reproducing Wilcox et al. (2015)

Stacking a lensing signal in the way just described in this Section was first used in Sheldon et al. (2001), where 42 clusters were stacked to obtain a higher signal to noise measurement. Ever since the publication of that work, stacking clusters to boost the measurable lensing signal has become more common. In Sheldon et al. (2001) and Mckay et al. (2001) 30,000 galaxies are stacked respectively to measure a lensing signal. This required centering on each of the lens to then sum all the tangential shears for each galaxy in radial bins. In this way, a shear measurement is recorded for every galaxy that is a set distance from any lens. The average tangential shear in each bin is then calculated and taken as the average shear value for all the lenses, just as described in this Section.

4.3.3 Binning the cluster sample into X-ray temperature bins

A source of systematic error when stacking profiles comes from mixing clusters of different sizes and masses. To minimise such effect in the modified gravity tests, the data set was binned in X-ray temperature. As explained in Section 1.2, X-ray temperature is related to its mass via Equation 4.3. So by binning in the sample in X-ray temperature, the sample is also split by mass. This cut was made at an X-ray temperature of $T = 2.5$keV, to give two bins

of mass with equal errors on their stacked profiles. Studies (Stott et al., 2010) in this matter show that this temperature cut splits the sources roughly into two samples: galaxy clusters (hotter systems) and galaxy groups (cooler).

4.4 Reproducing the results of Wilcox et al.

In this section I present the fit of a modified gravity model to the profiles derived in Section 4.3.1 and Section 4.3.2. I employed a multi-parameter MCMC method to minimize a χ^2 function and get constraints on the chameleon gravity parameters that will be discussed in Section 4.4.1. The results are shown in Section 4.4.2.

4.4.1 MCMC analysis

The analysis was performed in close collaboration with A. Tamosiunas from the University of Portsmouth. We used a code based on the one from Wilcox et al. (2015) but with changed python libraries. This code employs Markov chain Monte Carlo (MCMC) (Gilks, Richardson and Spiegelhalter, 1995) to fit models to the four stacked cluster profiles, both X-ray surface brightness and weak lensing for the two temperature bins, constructed in Section 4.3.1 and Section 4.3.2 respectively. The MCMC fit was made using *GetDist* (Foreman-Mackey et al., 2012), which, like other codes of this type, uses a random walk through the parameter space using a step size and direction defined by an algorithm. There are many algorithms that use this method but most of them are special cases of the Metropolis-Hastings algorithm (Metropolis et al., 1953), which is used in this work.

The Metropolis-Hastings algorithm works by starting at an arbitrary position in the parameter space X_t, where t denotes the time, the following position X_{t+1} is chosen by first sampling a candidate point Y from a proposed probability distribution function $q(|Y)$. The probability that the candidate point Y is accepted is given by

$$\alpha(X|Y) = \min\left(1, \frac{\pi(Y)q(Y|X)}{\pi(X)q(Y|X)}\right). \tag{4.7}$$

If the candidate point is accepted, the following state becomes $X_{t+1} = Y$, if the candidate is rejected the chain does not move $X_{t+1} = X_t$. This process is repeated until the parameter space has been sufficiently sampled.

All the parameters that depend upon the cluster properties were allowed to vary for each temperature bin during the MCMC run. This led to fourteen free parameters for the stacked profiles (ten used for each X-ray surface brightness profile and four for each weak lensing profile) for each temperature bin to constrain modified gravity. As covered thoroughly in Section 1.5.4, the X-ray surface brightness was modelled using Equation 1.10 by defining, for both temperature bins, the electron number density (dependent upon b_0, n_0, r_0) shown in Equation 1.11 and the normalization of the gas temperature T_0. On the other hand, the weak lensing mass was modelled using Equation 1.90 and Equation 1.25.

The chameleon gravity parameters described in Section 1.5.1 were reconfigured as

$$\beta_2 = \beta/(1+\beta) \quad , \quad \phi_{\infty,2} = 1 - \exp(-\phi_\infty/10^{-4}M_{Pl}) \tag{4.8}$$

in order to span the parameter range of β and ϕ_∞ in the interval [0,1]. The cooling function (see Sec. 1.1) was obtained by running XSPEC (Arnaud, 1996) using the APEC model (Smith et al., 2001) over the same range of the XMM observations, i.e., from 0.5 keV to 2 keV. This model has the gas temperature, the cluster redshift, the cluster metallicity and a normalization as inputs, it provides the X-ray cluster flux. The metallicity value of $Z = 0.3Z_{Sun}$ was adopted throughout this study. This model helped to generate fluxes for a range of temperatures which are interpolated for use in the modified theory of gravity model. The MCMC run was made in parallel in the Sciama supercomputer at the University of Portsmouth, using 128 walkers with 10,000 time steps with 2,000 iterations removes in the "burn in" phase.

Goodness of fit

The goodness of fit was minimized using χ^2 statistic derived from joint fitting of both models

$$\begin{aligned}\chi^2(T_0^I, n_0^I, b_1^I, r_1^I, M_{200}^I, c^I, T_0^{II}, n_0^{II}, b_1^{II}, r_1^{II}, M_{200}^{II},\\ c^{II}, \beta_2, \phi_{\infty,2}) = (\chi_{WL}^I)^2 + (\chi_{WL}^{II})^2 + (\chi_{SB}^I)^2 + (\chi_{SB}^{II})^2\end{aligned} \tag{4.9}$$

where the I, II notation will indicate from now on the temperature bin $T_X < 2.5$ and $T_X > 2.5$ respectively and

$$(\chi_{WL}^I)^2 = \sum_i \frac{(\gamma(r_{\perp,i}^I) - \gamma_i^{obs,I})^2}{(\sigma\gamma_i^{obs,I})^2}, \tag{4.10}$$

$$(\chi^{II}_{WL})^2 = \sum_i \frac{(\gamma(r^{II}_{\perp,i}) - \gamma^{obs,II}_i)^2}{(\sigma\gamma^{obs,II}_i)^2}, \tag{4.11}$$

$$(\chi^{I}_{SB})^2 = \sum_i \frac{(S_B(r^{I}_{\perp,i}) - S^{obs,I}_{B,i})^2}{(\sigma S^{obs,I}_{B,i})^2}, \tag{4.12}$$

$$(\chi^{II}_{SB})^2 = \sum_i \frac{(S_B(r^{II}_{\perp,i}) - S^{obs,II}_{B,i})^2}{(\sigma S^{obs,II}_{B,i})^2}, \tag{4.13}$$

With $\gamma_(r_{\perp,i})$ is the value of the lensing model at a distance $r_\perp$ from the cluster centre, in the meantime $S_B(r_{\perp,i})$ is the value of the surface brightness model at a distance $r_\perp$ from the cluster's centre. $\gamma^{obs}_i, S^{obs}_{B,i}$ are the observed shear profile and a surface brightness profile respectively, while $\sigma\gamma^{obs}_i$ is the observed error on the shear profile.

4.4.2 Results

Figure 4.4 shows the results of the four fits for the two temperature binned X-ray surface brightness and weak lensing profiles using the 14 model parameters from Section 4.4.1 and minimizing χ^2 from Equation 4.9 (see Figure 4.5). Two sets of data are shown in Figure 4.4: the dots, solid line, and grey bands correspond to the results from the new analysis (or "reproduction") of the Wilcox et al. (2015) by Tamosiunas and myself. The crosses and the solid line correspond to values and best fit originally derived by Wilcox et al. (2015). The surface brightness profiles are measured out to $1.2 \times r_{200}$. The two weak lensing profiles are presented out to $10 \times r_{200}$. It can be seen that the results from the new analysis follow more closely the line of best fit than those from Wilcox et al. (2015). This is due to improvements made to the methods using process the data, including with the approach taken for background subtraction, there are small differences.

Figure 4.6 shows the 2D constraints for the chameleon model parameters, β_2 and $\phi_{\infty,2}$, given by Equation 4.8. The 95% (99%) confidence limit constraint for these parameters is shown in mid blue (light blue). Also shown in this figure is the 95% (99%) confidence limit excluded region in the dashed (solid) from Wilcox et al. (2015) for comparison. It can be seen in the Figure that the values of the new analysis (or "reproduction") follow the similar shape of Wilcox et al. (2015), under a much larger number of time steps in the run (and smaller error bars in Figure 4.4) the reproduction values would resemble more the ones from the black lines. The measured likelihoods of the nuisance parameters (those different to β_2

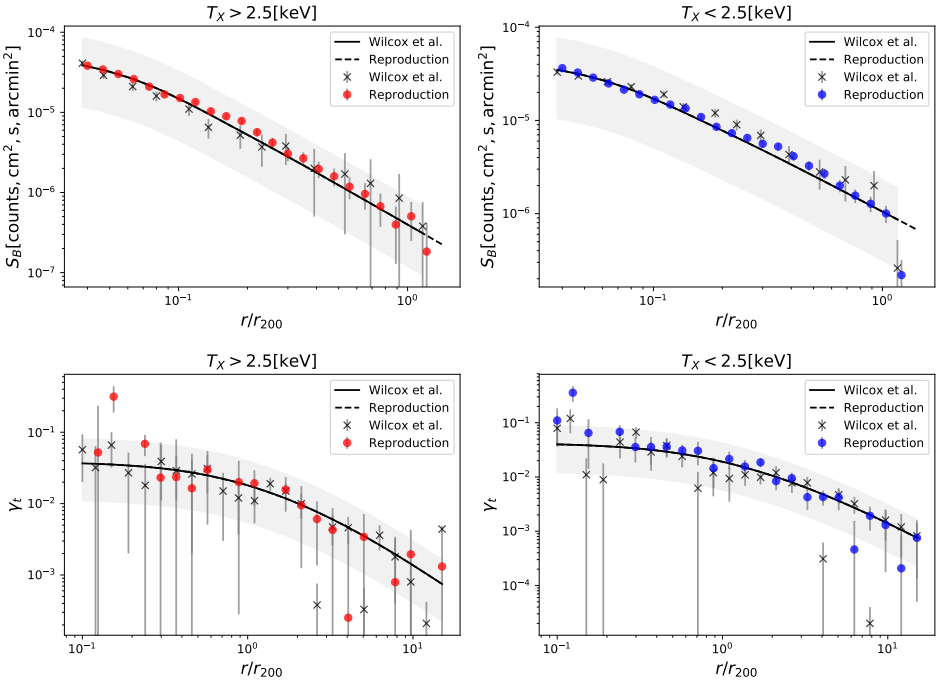

Figure 4.4: X-ray surface brightness profiles (top) and weak lensing (bottom) for the two bins of X-ray temperature: $T < 2.5$keV (left) and T > 2.5keV (right), against radial distance normalised by r_{200}, the radius at which the density is two hundred times the critical density. Two sets of data are shown in this figure: the dots with their (solid) line of best fit correspond to this work while the data in crosses with their dashed line of best fit correspond to Wilcox et al. (2015). I chose to show the modified gravity profiles with the highest likelihood parameters: $T_0^I = 13.7$keV, $n_0^I = 1.26[10^{-2}\text{cm}^{-3}]$, $b_1^I = -0.56$, $r_1^I = 0.07$ Mpc, $M_{200}^I = 9.0[10^{14}\text{M}_{\text{Sun}}]$, $c^I = 5.3$, $T_0^{II} = 6.9$ keV, $n_0^{II} = 2.36[10^{-2}\text{cm}^{-3}]$, $b_1^{II} = -0.681$, $r_1^{II} = 0.0417$[Mpc], $M_{200}^{II} = 9.7[10^{14}\text{M}_{\text{Sun}}]$, $c^{II} = 4.9$, $\beta_2 = 0.52$, $\phi_{\infty,2} = 0.47 \times 10^{-4}\text{M}_{\text{Pl}}$. The light grey shaded area correspond to the 2σ regions.

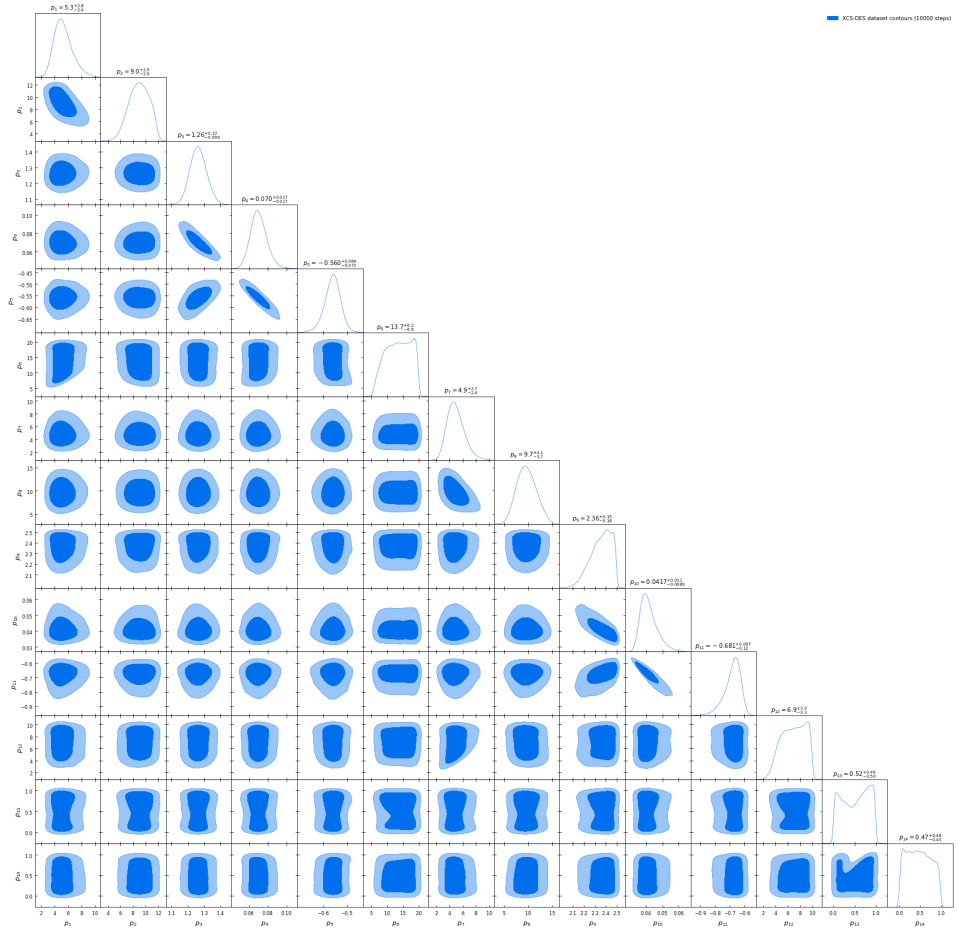

Figure 4.5: The 95% (dark blue region) and the 99% CL (mid blue region) 2D marginalised contours for the 14 model parameters $p_i (i = 1, ..., 14)$: c^I, $M^I_{200}[10^{14}\mathrm{M_{Sun}}]$, $n^I_0[10^{-2}\mathrm{cm}^{-3}]$, $r^I_1[\mathrm{Mpc}]$, b^I_1, $T^I_0[\mathrm{keV}]$, c^{II}, $M^{II}_{200}[10^{14}\mathrm{M_{Sun}}]$, $n^{II}_0[10^{-2}\mathrm{cm}^{-3}]$, $r^{II}_1[\mathrm{Mpc}]$, b^{II}_1, $T^{II}_0[\mathrm{keV}]$, β_2, $\phi_{\infty,2}$ used in the MCMC analysis. The rightmost plots show the 1D likelihood distributions. This figure is equivalent to Figure C1 in Wilcox et al. (2015) but produced with updated data.

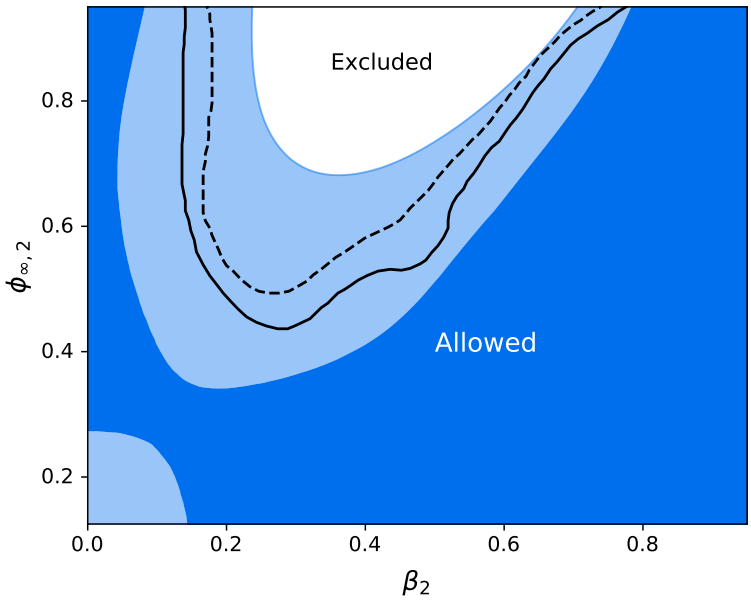

Figure 4.6: The 95% (mid blue region) and the 99% confidence limit (light blue region) constraints for the chameleon model parameters, $\beta_2 = \beta/(1+\beta)$ and $\phi_{\infty,2} = 1 - \exp(\phi_\infty/10^{-4}\mathrm{M_{Pl}})$ obtained from the MCMC analysis of the combination of the X-ray surface brightness and weak lensing profiles for the two cluster stacks of 58 clusters from Wilcox et al. (2015). Also shown in this figure is the 95% (99%) confidence limit excluded region in the dashed (solid) from Figure 3 in Wilcox et al. (2015) for comparison.

or $\phi_{\infty,2}$) are marginalised to generate the modified gravity constraints. The shape of these contours follow the definition of the β (strength of the fifth force) and ϕ_∞ (effectiveness of the screening mechanism) parameters given by Equation 1.81 in Section 1.5.3. As covered in Section 1.5.3, a low value of β causes a deviation to the profile to be distinguished from GR given the observational errors. When GR is recovered outside the critical radius r_c, setting an upper limit on β/ϕ_∞. With the increase of β, a lower value for ϕ_∞ is necessary to keep r_c within the cluster, which explains the oval shape of the excluded region.

With the results presented above, I have shown the methodology developed by myself and Tamosiunas (Section 4.3) is reliable, as it produces results consistent with those published in (Wilcox et al., 2015). As a consequence, we can feel confident about applying the this methodology again to a different CFHTLS cluster sample in Section 4.5 and to different weak lensing data from the Dark Energy Survey in Chapter 5.

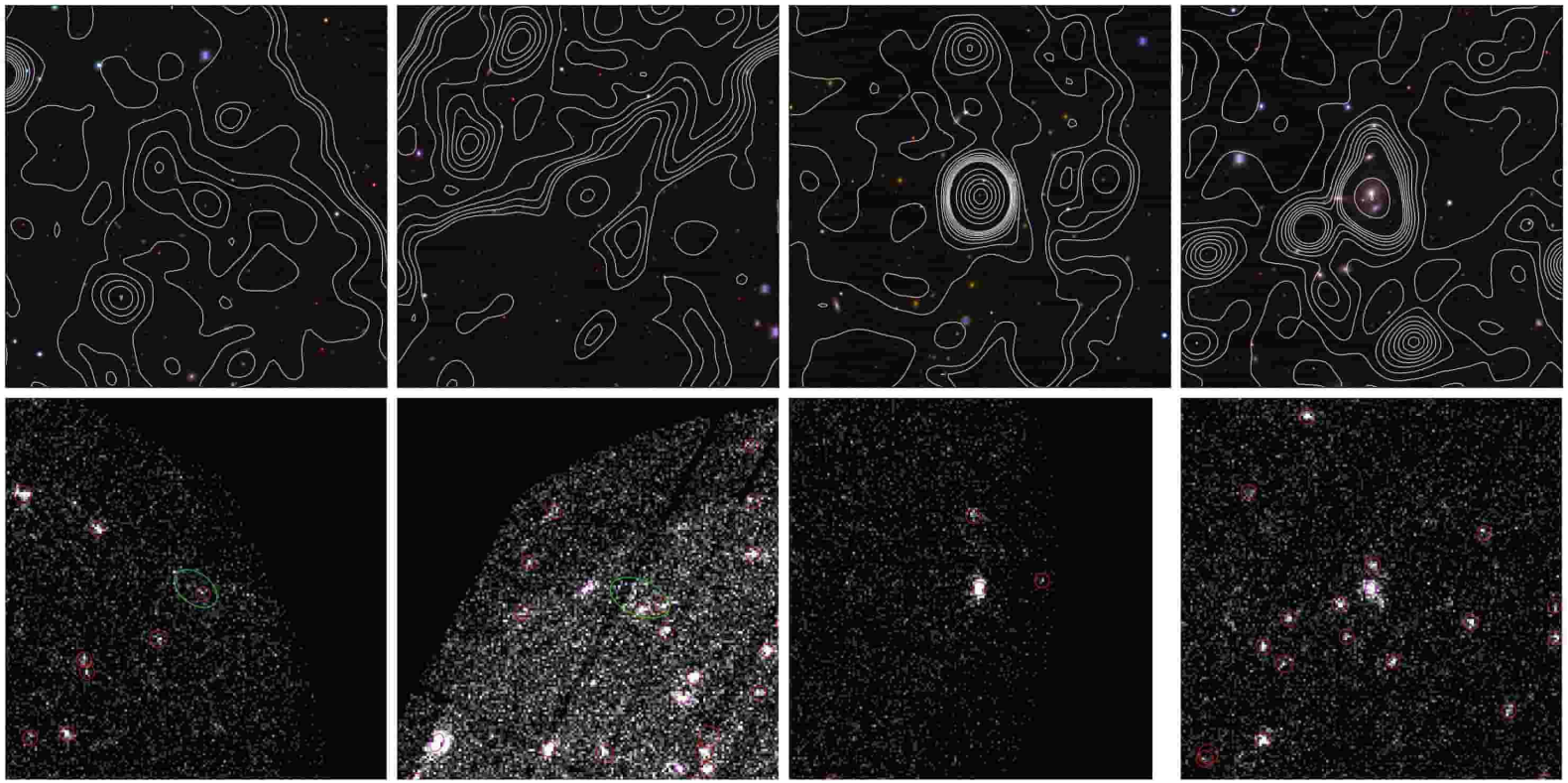

Figure 4.7: Examples of X-ray sources in (Wilcox et al., 2015) that were classified as clusters but that have now been reclassified. Their corresponding optical images (with data taken from CFHTLS) with X-ray contours (with data taken from XCS) are shown (top) and their X-ray images (bottom). From left to right: XMMXCS J021719.1-040333.5, XMMXCS J022433.1-040030.5, XMMXCS J020744.0-060956.6, XMMXCS J022456.1-050802.0.

4.5 A New XCS-CFHTLenS Sample

While developing the methods described in Section 4.3, I noticed that many of the sources (Wilcox et al., 2015) in the sample were not in fact galaxy clusters. A quick search of these sources in the most recent and updated version of the XCS MSL (see Sec. 2.2.3) revealed that XAPA now classified 8 of these objects as point sources (rather than extended). A further 11 were classed as extended sources but with a PSF warning flag (and thus require careful examination). The reason the MSL had different classifications was because the analysis techniques used by XCS have improved over the intervening years as explained in Section 2.2.4.

Including an X-ray source that is not a cluster to a sample would add noise in the weak lensing signal (since there would be not any shear at the location). However, in the X-ray profile that would be an effect, especially in the core, if point sources were being included in the stack. However, as mentioned in Section 1.5, the sensitivity of the gravitational model comes from the outskirts of the cluster, so the presence of some point sources in the (Wilcox et al., 2015) analysis may not have made a significant impact. That said, I felt it was important to test whether sample impurity were affecting the conclusions regarding constraints on the chameleon model.

Therefore, I decided to inspect the optical and X-ray images of all of the objects in the sample to determine if whether they were liklely to be clusters or not. As a result, 27 of the 58 objects in Wilcox et al. (2015) were removed from the sample. These objects did not meet the requirements to qualify as cluster candidates that have been adopted by the XCS collaboration, i.e. either the X-ray extended emission did not coincide with an obvious overdensity of galaxies, or an overdensity of galaxies did not coincide with an obvious X-ray source with extended emission (see Sec. 3.4.1). Table 4.1 shows some of information about the characteristics of these clusters. Figure 4.7 shows some examples of the particular type of sources that were removed from the sample; many of the sources with a PSF flag resembled a point like source rather than an ensemble of multiple galaxies with an extended X-ray emission.

Removing these 27 objects has improved the purity of the cluster sample, however it will have also reduce its completeness (because some of the removed objects will in fact be clusters). This will not be a problem for our study since corrections for sample selection function are not required in this type analysis (see for instance Terukina and Yamamoto (2012) and Terukina et al. (2014) where the study is done using only the Hydra and Coma clusters

Redshift range	N	$\langle z \rangle$	$\langle T_X \rangle$ [keV]	$\langle L_X \rangle [10^{44} \mathrm{erg/s}]$	$\langle \mathrm{counts} \rangle$
[0.1065, 0.25]	5	0.23	1.91	0.21	596
(0.25, 0.45]	9	0.38	2.55	0.53	384
(0.45, 0.65]	5	0.73	2.02	1.42	303
(0.65, 1.201]	8	0.47	2.12	0.79	422

Table 4.1: Characterization of the 27 objects in the Wilcox et al. (2015) sample that were removed. The table includes (from left to right): the number of clusters, average redshift, average temperature, average luminosity, and average photon counts are given for each redshift bin.

respectively). However, it would still be beneficial to maximise the number of clusters used in the stacked profile, in order to increase the signal to noise in the outskirts and this improve the constraints on gravity models.

Therefore, I decided to increase the size of the cluster sample by conducting a new search for XCS cluster candidates in the CFHTLenS footprint. To avoid the time consuming process of classifying potential candidates described in Section 3.4.1, a cross-match between the latest available XCS MSL and the 3D-MF catalogue (see Sec. 2.6) was used. For this, it was assumed that all physical matches would occur within $1.5h^{-1}$ Mpc of the 3D-MF centre (assuming the XCS source to be at the 3D-MF redshift), and that all physical matches would be with the sources classified as extended (including PSF sized) in the XCS MSL with more than 200 photon counts. This criteria allows the measurement of X-ray temperatures with an associated error of less than 30% (see Sec. 2.2.4). Another aspect taken into consideration, which was not considered by Wilcox et al. (2015), as mentioned in Section 4.3.1, was to select candidates without potential sources of contamination in their X-ray images. Any XMM observation usually contains point-like sources, of which most are AGN. If X-ray bright AGN lie within, or along the line of sight to, a given cluster, that cluster's surface brightness will be overestimated. Therefore, I selected only those XCS sources without MSL warning flags when matching to 3D-MF clusters candidates.

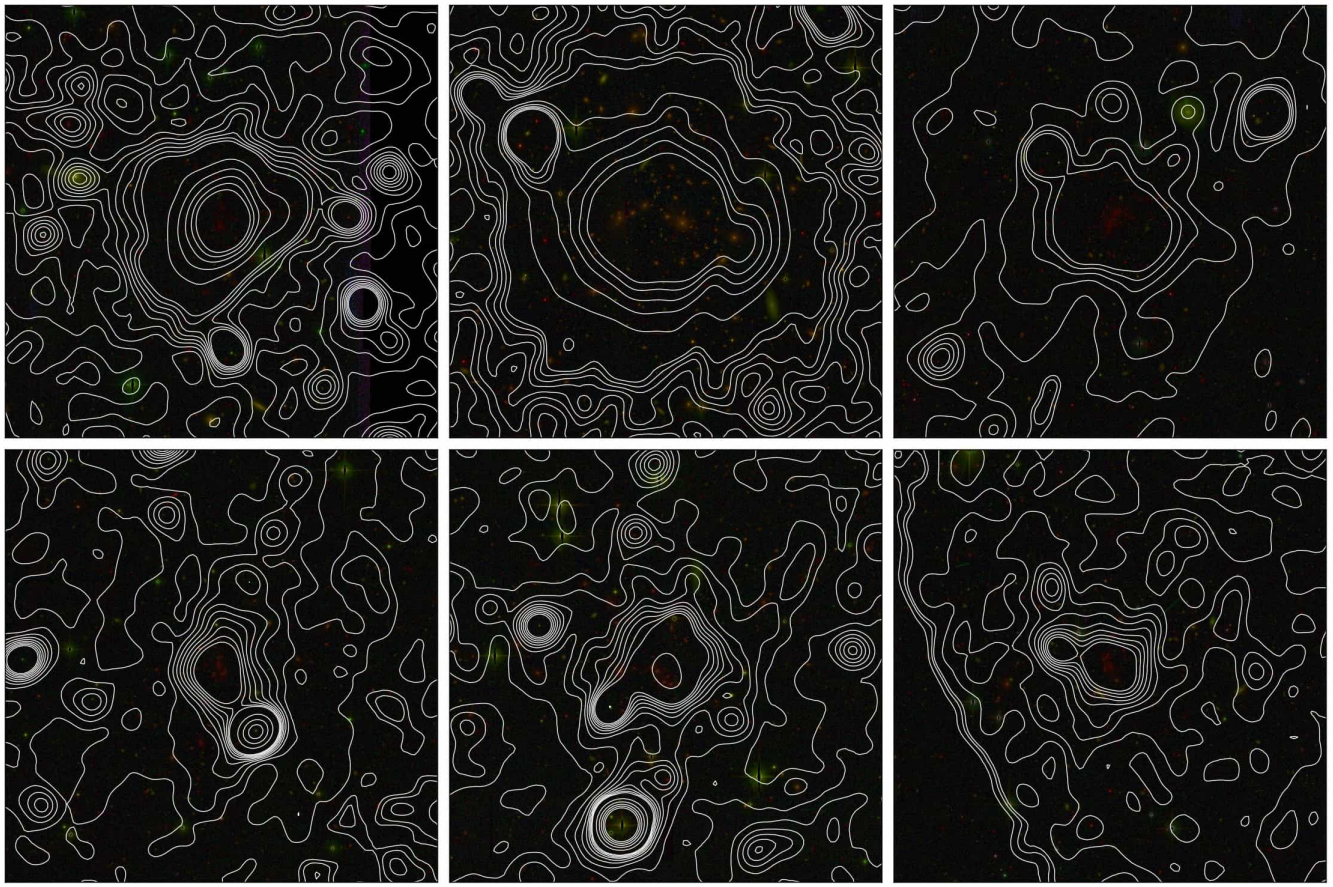

Figure 4.8: A selection of XCS+3D-MF clusters. The false colour optical images are 6×6 arcminutes in size and were generated from public CFHTLS data. The clusters are overlaid with X-ray contours generated by XCS. From left to right XMMXCS J141446.9+544709.1 ($z = 0.6$), XMMXCS J022145.6-034613.7 ($z = 0.5$), XMMXCS J020647.7-065648.9 ($z = 0.5$), XMMXCS J020524.4-054349.2 ($z = 0.3$), XMMXCS J020341.8-074704.2 ($z = 0.2$), XMMXCS J023142.5-045254.5 ($z = 0.2$)

While the 3D-MF catalogues contain clusters detected at $> 3.5\sigma$, it is expected to find increasing numbers of contaminating objects as this limit is approached (see Sec. 2.6). Therefore, I made a cut at $> 5\sigma$ to ensure the sample is as uncontaminated as possible. Not all of the 3D-MF $> 5\sigma$ clusters that fall in XMM images will have an XCS extended source counterpart because: the respective location in the XMM observation may have a low exposure time and/or high background, or fall on the edge of the field of view (where the PSF is poorly modelled), or fall in an EPIC chip gap. The matching procedure produced 86 cluster candidates. This number excludes 9 cluster candidates that were found in the 3D-MF catalogues but that already were part of the cleaned Wilcox et al. (2015) sample. The Wilcox et al. (2015) redshifts were consistent with those in 3D-MF catalogues. In the subsequent analysis, the Wilcox et al. (2015) redshifts were used.

Next, I prepared optical and X-ray images prepared for each of the 86 candidates so that a visual inspection could take place. A conservative approach was taken, and of these 86, only 46 sources were confirmed as clusters, i.e. the X-ray object needed to be an obvious source of extended emission and it had to coincide with an obvious overdensity of galaxies. When combined with the cleaned Wilcox et al. (2015) sample, the resulting list contained 77 X-ray selected, optically confirmed, clusters in the CFHTLenS footprint. Figure 4.9 shows the redshift (left panel) and normalized X-ray temperature (right panel) distributions for the original sample from Wilcox et al. (2015) and the new XCS-CFHTLenS sample. The full cluster list is given in Table C.1 in Appendix C. A few examples of the optical images of the XCS+3D-MF clusters are shown in Figure 4.8.

4.5.1 X-ray data from XCS

The latest version of XCS3P was then used to derive the X-ray spectral properties of the 77 cluster candidates, namely their X-ray temperature, (T_X), and luminosity, (L_X). As summarized in Section 2.2, the pipeline can be run in batch mode and applied to hundreds of clusters at the same time. I ran XCS3P on the APOLLO supercomputer at the University of Sussex. An overview of XCS3P, including the methodology of the reduction process of archival XMM observations, can be found in Lloyd-Davies et al. (2011). Some of the improvements and corrections made since is covered in P. Giles (in prep.).

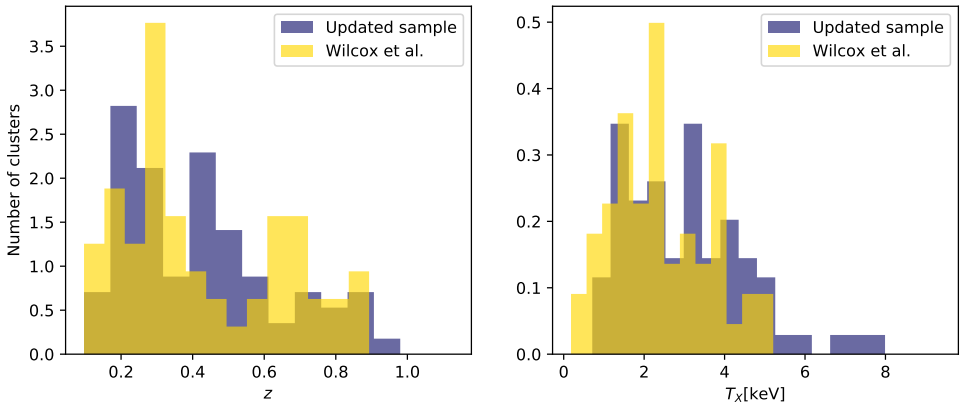

Figure 4.9: The redshift and (normalized) X-ray temperature distributions for the sample from (Wilcox et al., 2015) of 58 objects in yellow and of the new 77 cluster candidates from XCS-CFHTLenS in blue. These figures show the large range both in redshift and temperature (normalized) of the two samples.

4.5.2 Stacking the cluster profiles

I stacked the X-ray surface brightness profiles of the new sample in the same way as described in Section 4.3.1. Each of the clusters was rescaled to a standard projected size using M_{200} values to calculate r_{200}. The surface brightness profiles of the individual clusters were binned into 24 equally spaced logarithmic annulus out to a distance of $1.2 \times r_{200}$, rescaled, and stacked using linear interpolation to a common 500 by 500 pixel format as shown in Figure 4.10. The bootstrapping method used before was applied to this sample to estimate errors on the surface brightness.

I stacked the individual shear cluster profiles of the new sample using the same method of Section 4.3.2 and from CFHTLenS for the new added objects. For each galaxy I calculated the tangential and cross shears given by Equation 1.37 as a function of their position relative to the cluster position. The tangential shear around each of the clusters was binned into 24 equally spaced logarithmic annuli out to a distance of $10 \times r_{200}$. Then, the 77 individual cluster profiles were stacked. The errors on the shear profile were estimated using the bootstrap resampling method described in Section 4.3.1.

The data set was split again into two separate temperature bins as done in Section 4.3.3. The sample was cut $T_X = 2.5$keV, 44 clusters had $T_X > 2.5$ keV and 33 clusters had $T_X < 2.5$.

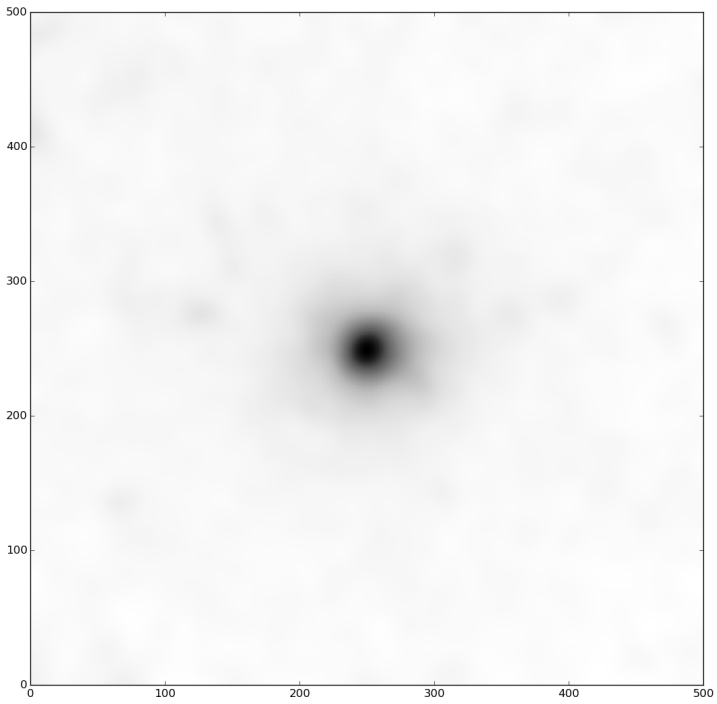

Figure 4.10: Stacked 2D surface brightness profile of 77 clusters from the new sample from XCS and CFHTLenS. This 500×500 pixels figure was made by taking the mean value of each pixel of the individual 2D surface brightnesses for each of the clusters in the sample. The physical surface brightness profile of this image is shown in Figure 4.11.

4.5.3 MCMC analysis

The analysis outlined in Section 4.4.1 was repeated in collaboration with Tamosiunas. We used MCMC to fit models to the four stacked cluster profiles, both X-ray surface brightness and weak lensing for the two temperature bins, from the previous section.

As in Section 4.4.1, all the parameters that depend upon the cluster properties were allowed to vary for each temperature bin during the MCMC run. I used again the configuration of the chameleon gravity described by β_2 and $\phi_{\infty,2}$ in Equation 4.8. The MCMC run was made in parallel in the Sciama supercomputer at the University of Portsmouth, using 128 walkers with 10,000 time steps with 2,000 iterations removes in the 'burn in' phase.

The goodness of fit was minimized using the same χ^2 statistic of Section 4.9, which is derived from the joint fitting of both models.

4.5.4 Results

I show in Figure 4.11 the X-ray surface brightness and weak lensing profiles measured for the two temperature bins. The surface brightness profiles are measured out to $1.2 \times r_{200}$. Similarly, the two weak lensing profiles are presented out to $10 \times r_{200}$. In the same figure is shown the best fit models for each profile using the parameters summarized in Section 4.4.1 and minimizing χ^2 following Equation 4.9 of Figure 4.12. These best fit models are compared to the fits from GR which use Equation 1.4 when solving Equation 1.10, showing that the effect that $f(R)$ would have on the profile in the presence of the chameleon field is not distinguishable between the two (see bottom left window in Fig. 5.3), which is due to the large size of the error bars in the surface brightness profiles at large radii. This would imply that the extra field has barely an effect on the profile outside the value of β_2 (at large values of r_c) as also shown in Wilcox et al. (2018) and confirmed by other studies too (Lubini et al., 2011; Arnold, Puchwein and Springel, 2014) but is not possible to tell, constraints can still be set to the parameters nonetheless. As demonstrated by Equation 1.88 in Section 1.5.3, the modified gravity model does not affect the weak lensing profile so is not necessary to show the relativistic model explicitly for comparison.

In Figure 4.13, I show the 2D constraints for β_2 and $\phi_{\infty,2}$. In this figure is also presented, within the mid-blue (light blue) region, the 95% (99%) confidence limit excluded region defined by Terukina and Yamamoto (2012) (see Fig. 1.6). Again, the measured likelihoods

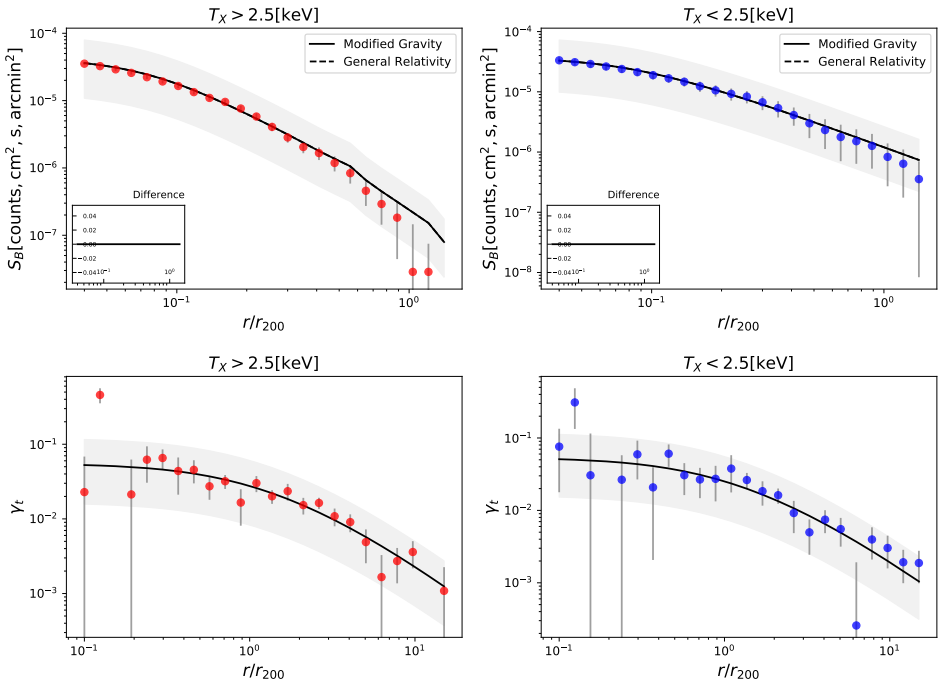

Figure 4.11: X-ray surface brightness profiles (top) and weak lensing (bottom) for the two bins of X-ray temperature: $T < 2.5$keV (left) and T > 2.5keV (right), against radial distance normalised by r_{200}, the radius at which the density is two hundred times the critical density. The line of best fit for the chameleon model is shown with the solid line with the highest likelihood parameters given by $T_0^I = 22.0$keV, $n_0^I = 1.08[10^{-2}\text{cm}^{-3}]$, $b_1^I = -0.605$, $r_1^I = 0.093$ Mpc, $M_{200}^I = 21[10^{14}\text{M}_{\text{Sun}}]$, $c^I = 4.78$, $T_0^{II} = 9.3$ keV, $n_0^{II} = 1.306[10^{-2}\text{cm}^{-3}]$, $b_1^{II} = -0.754$, $r_1^{II} = 0.0904[\text{Mpc}]$, $M_{200}^{II} = 27.0[10^{14}\text{M}_{\text{Sun}}]$, $c^{II} = 4.41$, $\beta_2 = 0.55$, $\phi_{\infty,2} = 0.41 \times 10^{-4}\text{M}_{\text{Pl}}$. The relativistic model is shown with the dashed line for comparison. The small window in the surface brightness profiles panels corresponds to the between the lines of best fit for both models, where the chameleon model should separate from the relativistic case in the outskirts of the cluster. The light grey shaded area corresponds to the 2σ regions.

of the nuisance parameters (those different to β_2 or $\phi_{\infty,2}$) were marginalised to generate the modified gravity constraints. This is possible because the chameleon gravity model outlined in Section 1.5 is not sensitive to the overall amplitude of the cluster profiles, the shape of the profiles is the only that matters for the constraints. The shape of the contours in Figure 4.13 follow the definition of the β (strength of the fifth force) and ϕ_∞ (effectiveness of the screening mechanism) parameters.

Implications for modified gravity

The constraints presented in the Section 4.5.4 have implications for $f(R)$ gravity models for chameleon mechanisms with $\beta = \sqrt{1/6}$ (Starobinsky, 2007) as explained in Section 1.5.2. The estimated upper bound on $f(R)$ gravity is $\phi_\infty < 5.425 \times 10^{-5}$ at 95% confidence limit, which corresponds to the value of ϕ_∞ where $\beta = \sqrt{1/6}$ intersects the light blue region in Figure 4.13. Using Equation 1.77, which relates $f(R)$ to ϕ_∞, it turns that $f_R(z = 0.41) < 4.42 \times 10^{-5}$ at 95% confidence limit (where $z = 0.41$ is the median redshift of the cluster sample). The time evolution of the background $f_R(z)$ given in (Li et al., 2013) is

$$f_R(z) = |f_{R0}|(1/n)((1 + \Omega_\Lambda)/(\Omega_M(1 + z)^3 + 4\Omega_\Lambda))^{n+1} \tag{4.14}$$

where n is a free parameter of the model (described in Eqn 1.71). At higher redshifts, the background energy density is higher, therefore $f_R(z)$ is smaller and the screening is more efficient. So $f_R(z)$ decreases by 16% from the median redshift ($z = 0.41$) of the sample to $z = 0$, when $n = 1$ and the constraint at $z = 0$ is $|f_{R0}| < 7.3 \times 10^{-5}$ at 95% confidence limit. For a model with $n = 3$, the constraint becomes $|f_{R0}| < 1.77 \times 10^{-4}$ at 95% confidence limit.

With this considered, I found that my results for the revisited and updated XCS-CFHTLenS sample are no different and of the same order of magnitude of Terukina et al. (2014) and Wilcox et al. (2015). Which have $|f_{R0}| < 6 \times 10^{-5}$ for $n = 1$ and $|f_{R0}| < 2 \times 10^{-4}$ for $n = 3$, compared with my measurement of $f_{R0} < 3.83 \times 10^{-5}$ for $n = 1$ and $|f_{R0}| < 1.77 \times 10^{-4}$, all at 95% confidence level. Figure 4.14 shows a comparison of these constraints with Terukina et al. (2014) and Wilcox et al. (2015), the solid (dashed) red line represents the 95% (99%) confidence limit excluded region. Exhibiting no major impact in the order of magnitude of the constraints other than consistency despite having a slightly larger number of clusters. My results are also one order of magnitude stronger than those from the CMB (Raveri et al.,

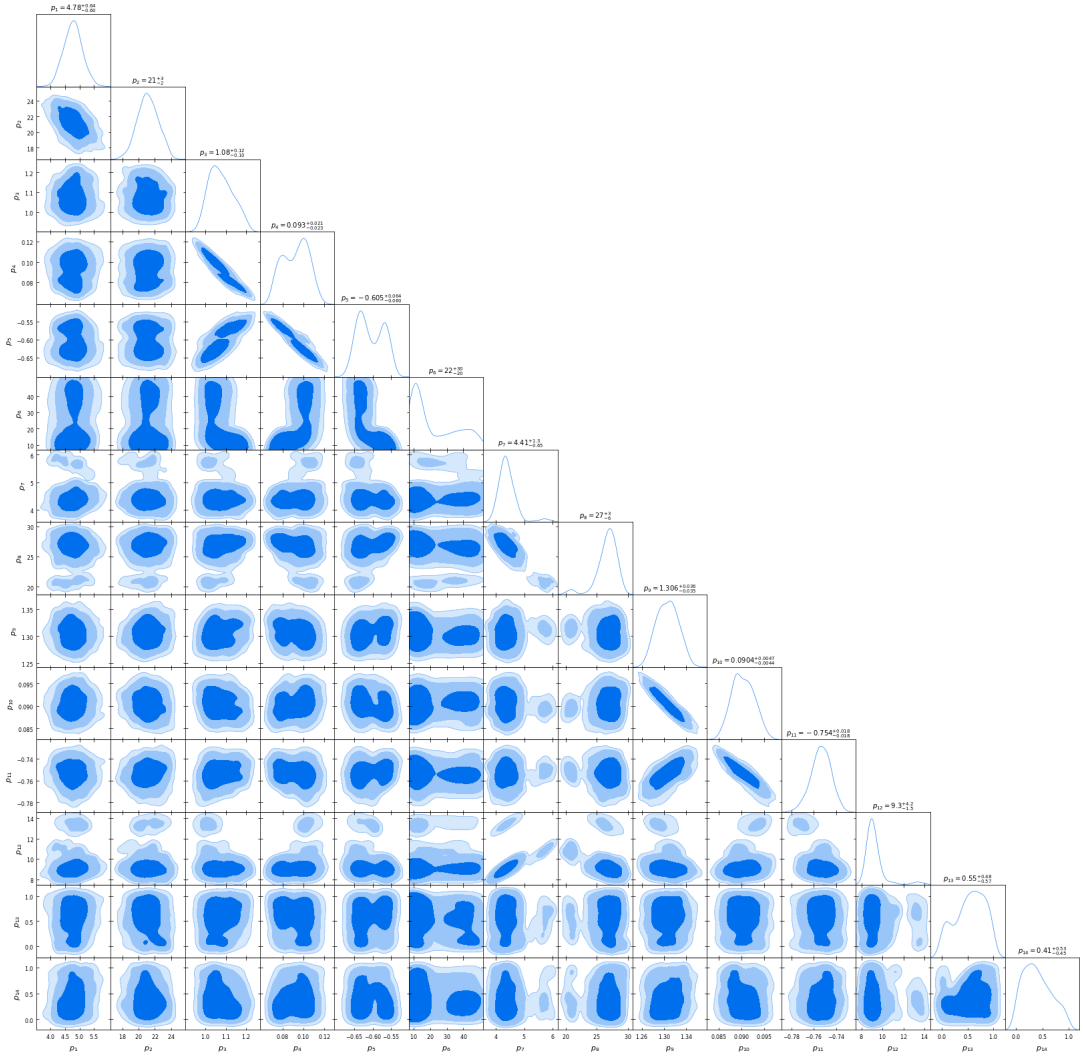

Figure 4.12: The 95% (mid blue region) and the 99% CL (light blue region) 2D marginalised contours for the 14 model parameters $p_i (i = 1, ..., 14)$: c^I, $M^I_{200}[10^{14}\mathrm{M_{Sun}}]$, $n^I_0[10^{-2}\mathrm{cm}^{-3}]$, $r^I_1[\mathrm{Mpc}]$, b^I_1, $T^I_0[\mathrm{keV}]$, c^{II}, $M^{II}_{200}[10^{14}\mathrm{M_{Sun}}]$, $n^{II}_0[10^{-2}\mathrm{cm}^{-3}]$, $r^{II}_1[\mathrm{Mpc}]$, b^{II}_1, $T^{II}_0[\mathrm{keV}]$, β_2, $\phi_{\infty,2}$ used in the MCMC analysis for the new XCS-CFHTLS sample of 88 clusters. The rightmost plots show the 1D likelihood distributions.

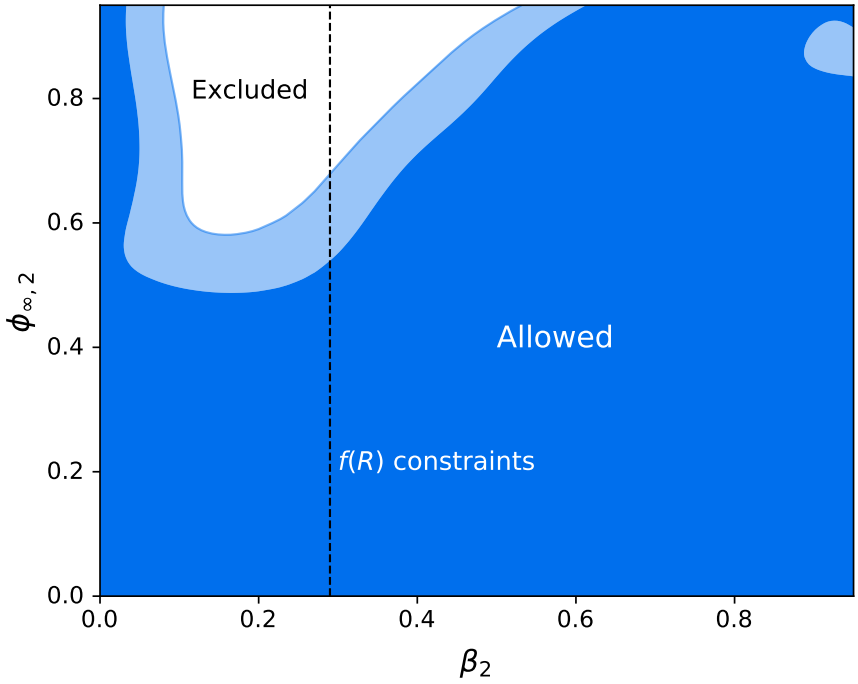

Figure 4.13: The 95% (mid blue region) and the 99% confidence limit (light blue region) constraints for the chameleon model parameters, $\beta_2 = \beta/(1+\beta)$ and $\phi_{\infty,2} = 1 - \exp(\phi_\infty/10^{-4}\mathrm{M_{Pl}})$ obtained from the MCMC analysis of the combination of weak lensing and X-ray surface brightness for our two cluster stacks. The dashed vertical line is at $\beta = \sqrt{1/6}$, showing the constraints for $f(R)$ gravity models.

2014) and are comparable to Cataneo et al. (2014) as shown in Table 5.1 in Section 5.4.1 in Chapter 5.

4.6 Conclusions

In this chapter I have reproduced the methodology and results of Wilcox et al. (2015) to constrain modified gravity models using stacked galaxy cluster profiles. In order to do so, I have used the original CFHTLens sample from this publication to test the stacking methodology. I also examined such sample and removed some of its sources and added new cluster candidates to expand it to 77 clusters. I examined the weak lensing data from CFHTLenS for this samples, together with the X-ray data from XCS. With the samples binned by X-ray temperature, I generated both X-ray surface brightness profiles and weak lensing profiles.

I reproduced the results obtained by Wilcox et al. (2015) using a larger and better X-ray selected cluster sample. I studied the chameleon screening mechanism which predicts the existence of an additional pressure that lies in between clusters. This extra force causes the gas component of a cluster to become more compressed than general relativity gravity predicts. To study this phenomena, I compared the X-ray profile to the weak lensing profile, which is unaffected by the fifth force. It was found that, given the size of the error bars in the surface brightness profiles, this extra pressure is barely distinguishable from the relativistic side. The MCMC analysis of these profiles produced constraints on the chameleon parameters β and ϕ_∞, used to also constrain $|f_{R0}|$, a parameter characterising $f(R)$ theories. These results are of the same order of magnitude as the results of Terukina et al. (2014) and Wilcox et al. (2015), without putting further constraints on these parameters despite having a larger and better sample.

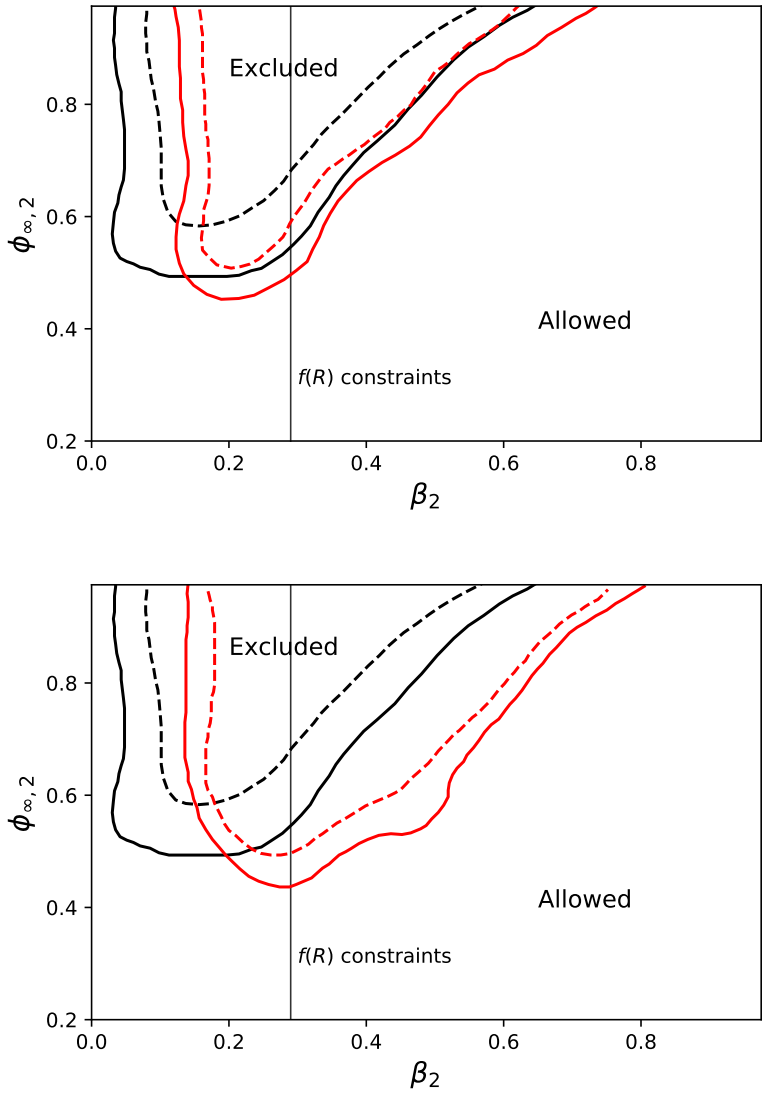

Figure 4.14: *Top*: comparison between the 95% (dashed line) and the 99% confidence limit (solid line) constraints for the chameleon model parameters, β_2 and $\phi_{\infty,2}$, for the new XCS-CFHTLS sample (black) and the 95% (solid line) and 99% (dashed line) from the sample of Terukina et al. (2014) in red. *Bottom*: comparison between the 95% (dashed line) and the 99% confidence limit (solid line) constraints for the chameleon model parameters, β_2 and $\phi_{\infty,2}$, for the new XCS-CFHTLS sample (black) and the 95% (solid line) and 99% (dashed line) from the sample of Wilcox et al. (2015) in red. The vertical dotted line is at $\beta = \sqrt{1/6}$, showing the constraints for $f(R)$ gravity models in both figures.

Chapter 5

Constraining gravity models with DES and XCS

The constraints on chameleon gravity models presented in the previous Chapter were limited by the number of clusters available with sufficient high quality weak lensing data. However, as mentioned in Section 2.3.3, the advent of large imaging surveys, such as DES and LSST, will provide larger cluster catalogues with both X-ray and weak lensing data. In this chapter I introduce a redMaPPer selected cluster sample from the DES Y1 data release. I use this sample to perform another comparison of X-ray and weak lensing cluster profiles to place limits on the strength of the fifth force. The lay out of this chapter is as follows. In Section 5.1, I describe the DES Y1 redMaPPer sample of clusters with X-ray data from XCS. The techniques employed in the previous chapter to produce both an X-ray stacked profile and weak lensing stacked profile are repeated in Section 5.2 and Section 5.2. The chapter ends with the MCMC fits of the same gravity models of the previous chapter to the derived profiles. This was done by minimising a χ^2 function and obtaining constraints on the chameleon gravity parameters. The implications of my results are discussed in Section 5.4.

5.1 A redMaPPer selected cluster sample

The cluster sample selected for this follow-up study is the one from Farahi et al. (2019), outlined in Appendix A.2.2, which is based on data obtained during the DES Y1 observing season summarized in Section 2.3.2. The sample consists of a volume-limited sample of 95 X-ray selected galaxy clusters from XCS detected in the DES Y1 photometric data using the

6.4.17 redMaPPer version (see Sec. 2.5). The X-ray information for these clusters was taken from XMM archival data.

5.1.1 X-ray data

The redMaPPer sample was matched to all XMM ObsIDs within a radius of 13 arcminutes between the redMaPPer position and the aim point of the ObsID. After this, the XMM observations were filtered by exposure time, requiring the mean and median to be $>$ 3ks and $>$ 1.5ks determined within a radius of 5 pixels centred on the the redMaPPer position. Where the mean is taken to be the exposure time averaged over the sum of each pixel, while the median refers to 50% of the pixel in the enclosed region. These cuts ensure that a redMaPPer cluster of interest is within the XMM field of view, but not falling on chip gaps, thus guaranteeing a long enough exposure time for reliable T_X measurements to be made. The X-ray sources in each ObsID were detected by XAPA in the way outlined in Section 2.2.3. At the position of the most likely central galaxy of each redMaPPer cluster, the XAPA extended sources were matched within a comoving distance of 2 Mpc. Finally, DES cutout and XMM images were produced, as described in Section 3.3, so that a visual inspection could take place. For this analysis presented in this chapter, the sample contained 95 clusters. The luminosities and temperatures for the sample were derived using the XCS Post Processing Pipeline described in Section 2.2.4.

5.1.2 Weak lensing data

I used the DES Y1A1 Gold catalogue to build the shear profiles. Several cuts were made following following the recommendations outlined in Section 2.3.3. The calibration columns (m, c_1, c_2), and the weight (w), covered in Section 4.3.2, were already calculated and provided in the DES Y1 shape catalogues.

As in Section 4.3.2, I made consistency tests of the DES Y1 shape data to ensure that the shear profiles are unbiased as much as possible. Figure 5.1(a) shows the tangential shear (blue) and the cross shear (orange) around the 95 stacked clusters. The tangential shear is different from zero at low radii while the cross shear takes constant values around zero at all radii. Figure 5.1(b) shows the tangential shear of the stacked cluster sample for three bins of source galaxies with different signal to noise ratios, $S/N < 20, 20 < S/N < 40$, and $S/N > 40$. The three signals are consistent with each other with increasing radius as

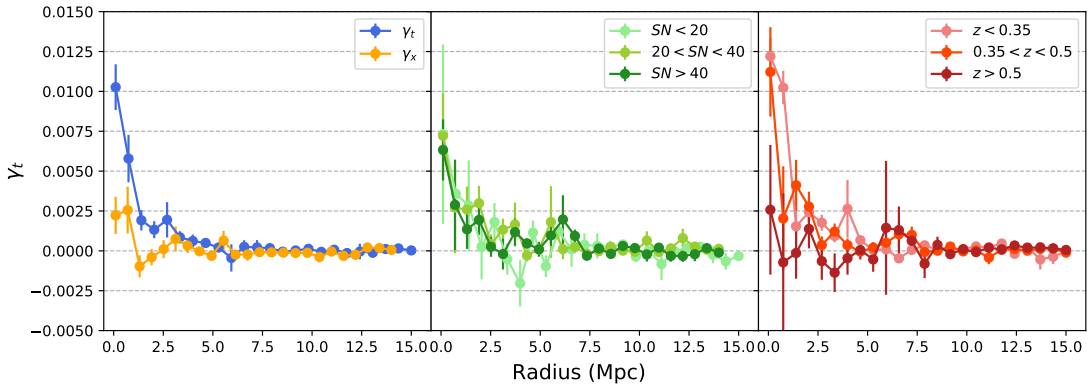

Figure 5.1: Null and consistency tests of the DES-Y1-RM data in binned annuli from the cluster stack centre. (a): The tangential shear around the 95 staked clusters in blue and the cross shear in orange. (b) The tangential shear around the cluster stack for three different signal to noise (S/N) bins. (c): The tangential shear around the cluster stack for three different redshifts.

expected. Figure 5.1(c) shows the tangential shear around the stacked clusters after being split into three different redshift bins, $z < 0.35, 0.35 < z < 0.5$, and $z > 0.5$ with means values of $0.27, 0.42, 0.58$ respectively. Since there is a smaller fraction of galaxies and clusters at higher redshifts, the weak lensing signal is expected to be reduced with redshift. This effect is seen in the measured signal for the high redshift bin. Therefore, completing the tests done in Figure 4.3 in Section 4.3.2.

5.2 Stacking the cluster profiles

The process of stacking the X-ray surface brightness profiles of the this sample was done in the same way as in Section 4.3.1. Each of the clusters was rescaled to a standard projected size using M_{200} values to calculate r_{200}. The surface brightness for every single cluster was binned into 24 equally spaced logarithmic annulus out to a distance of $1.2 \times r_{200}$, rescaled, and stacked using linear interpolation to a common 500 by 500 pixel format as shown in Figure 5.2. The bootstrapping method used before was applied to this sample to estimate errors on the surface brightness as well.

I stacked the individual shear cluster profiles of the new sample using the same method of Section 4.3.2. For each galaxy I calculated the tangential and cross shears given by Eq. 1.37 as a function of their position relative to the cluster position. The tangential shear around

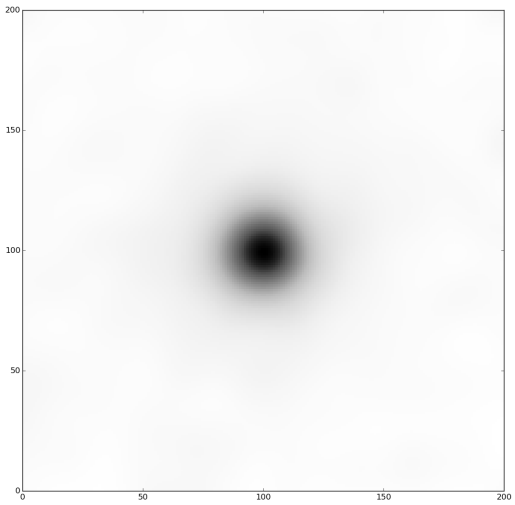

Figure 5.2: Stacked 2D surface brightness profile of 95 clusters from the redMaPPer cluster sample. This 500×500 pixels figure was made by taking the mean value of each pixel of the individual 2D surface brightnesses for each of the clusters in the sample. The physical surface brightness profile of this image is shown in Figure 5.3.

each of the clusters was binned into 24 equally spaced logarithmic annuli out to a distance of $10 \times r_{200}$. Then, the 95 individual cluster profiles were stacked. The errors on the shear profile were estimated using the bootstrap resampling method described in Section 4.3.1.

The data set was split into two separate temperature bins to reduce the error on the stacked profiles as done in Section 4.3.3. The sample was cut with $T_X = 2.5$ keV, where 72 clusters had $T_X > 2.5$ keV and 23 clusters had $T_X < 2.5$.

5.3 MCMC analysis

In collaboration with Tamosiunas, we repeated the analysis outlined in Section 4.4.1. Again, we used MCMC to fit models to the four stacked cluster profiles, both X-ray surface brightness and weak lensing for the two temperature bins.

As in Section 4.4.1, all the parameters that depend upon the cluster properties were allowed to vary for each temperature bin during the MCMC run. The MCMC run was made again in parallel in the Sciama supercomputer at the University of Portsmouth, using 128 walkers with 10,000 time steps with 2000 iterations removes in the 'burn in' phase.

The goodness of fit was minimized following again Section 4.9, which is derived from joint fitting of both models.

5.4 Results

I show in Figure 5.3 the X-ray surface brightness and weak lensing profiles measured for the two temperature bins. The large scatter of the points in the 'cool' ($T_X < 2.5$ keV) bin can be attributed to the low number of clusters, 23 clusters compared to the 72 clusters in the 'warm' ($T_X > 2.5$ keV) bin. This 'cool' bin has clusters with low richness (see Sec. 2.5), with $\langle\lambda\rangle_{T_X<2.5} = 33.99$ and $\langle z\rangle_{T_X<2.5} = 0.47$ compared to the sample mean of $\langle\lambda\rangle = 69.14$ and $\langle z\rangle = 0.43$, which is associated with a larger scatter in the recovered weak lensing profiles (Mcclintock et al., 2017). Figure 5.3 also shows the best fit models for each profile using the parameters summarized in Section 4.4.1 and minimizing χ^2 following Equation 4.9 (see Figure 5.5). These best fit models for the surface brightness profiles are compared to the fits from GR which use Equation 1.4 when solving Equation 1.10, showing again that the effect that $f(R)$ would have on the profile in the presence of the chameleon field is not distinguishable between the two (see bottom left window in Fig. 5.3), which is due to the large size of the error bars in the surface brightness profiles. As mentioned in Section 4.5.4, with these results is not possible to tell if the extra field has barely any effect on the profile. In Figure 5.4 I show the 2D constraints for β_2 and $\phi_{\infty,2}$ from Equation 4.8. In this figure is presented again, within the mid-blue (light blue) region, the 95% (99%) confidence limit excluded region defined by Terukina and Yamamoto (2012).

5.4.1 Implications for modified gravity

The constraints presented in the last section have for $f(R)$ gravity models for chameleon mechanisms with $\beta = \sqrt{1/6}$ (Starobinsky, 2007) as explained in Section 1.5.2. The upper bound on $f(R)$ gravity of 4.4×10^{-5} at 95% confidence limit, which corresponds to the value of $\phi_{\infty,2}$ where $\beta = \sqrt{1/6}$ intersects the dark blue region in Figure 5.4. Using Equation 1.77, which relates $f(R)$ to ϕ_∞, I got $f_R(z = 0.43) < 3.59 \times 10^{-5}$ at 95% confidence limit (where $z = 0.43$ is the median redshift of the cluster sample). Using the time evolution of the background $f_R(z)$ given by Equation 4.14 I computed that at higher redshifts, the background energy density is higher, therefore $f_R(z)$ is smaller and the screening is more efficient. So $f_R(z)$

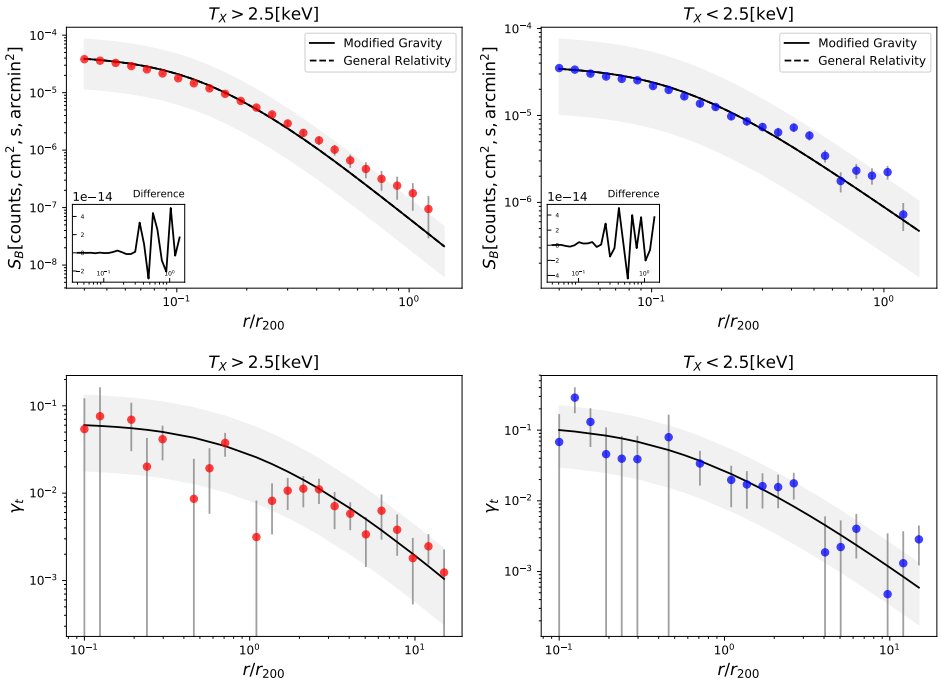

Figure 5.3: X-ray surface brightness profiles (top) and weak lensing (bottom) for the two bins of X-ray temperature: $T < 2.5$keV (left) and T > 2.5keV (right), against radial distance normalised by r_{200}, the radius at which the density is two hundred times the critical density. The line of best fit for the chameleon model is shown with the solid line with the highest likelihood parameters $T_0^I = 39.0$ [keV], $n_0^I = 2.84[10^{-2}\text{cm}^{-3}]$, $b_1^I = -0.95$, $r_1^I = 0.20$ [Mpc], $M_{200}^I = 25.0[10^{14}\text{M}_{\text{Sun}}]$, $c^I = 9$, $T_0^{II} = 15.3$ [keV], $n_0^{II} = 4.18[10^{-2}\text{cm}^{-3}]$, $b_1^{II} = -2.8$, $r_1^{II} = 0.39$ [Mpc], $M_{200}^{II} = 14[10^{14}\text{M}_{\text{Sun}}]$, $c^{II} = 7.7$, $\beta_2 = 0.63$, $\phi_{\infty,2} = 0.41 \times 10^{-4}\text{M}_{\text{Pl}}$. The relativistic model is shown with the dashed line for comparison. The small window in the surface brightness profiles panels corresponds to the difference between the lines of best fit for both models, where the chameleon model should separate from the relativistic case in the outskirts of the cluster. The light grey shaded area correspond to the 2σ regions. The light grey shaded area correspond to the 2σ regions.

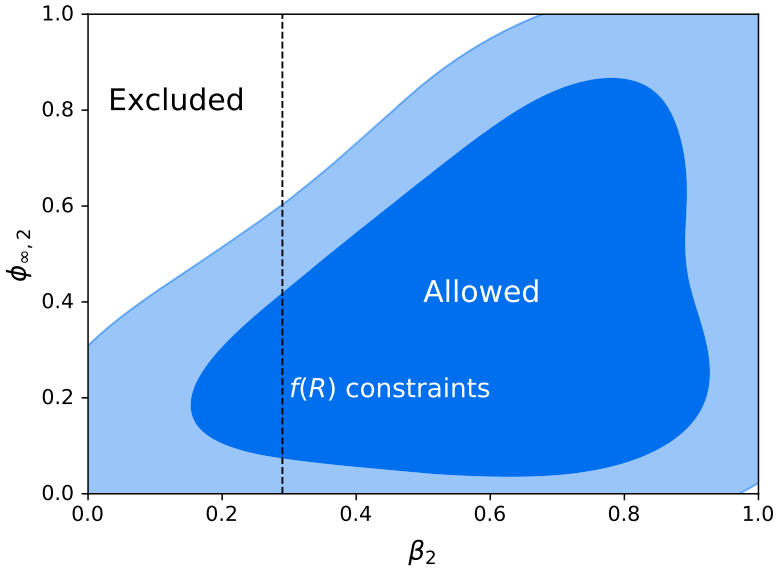

Figure 5.4: The 95% (mid blue region) and the 99% confidence limit (light blue region) constraints for the chameleon model parameters, $\beta_2 = \beta/(1+\beta)$ and $\phi_{\infty,2} = 1 - \exp(\phi_\infty/10^{-4}\mathrm{M_{Pl}})$ obtained from the MCMC analysis of the combination of weak lensing and X-ray surface brightness for our two cluster stacks. The dashed vertical line is at $\beta = \sqrt{1/6}$, showing the constraints for $f(R)$ gravity models.

decreases by 24% from the median redshift ($z = 0.43$) of the sample to $z = 0$, when $n = 1$ and the constraint at $z = 0$ is $|f_{R0}| < 3.6 \times 10^{-5}$ at 95% confidence limit. For a model with $n = 3$, the constraint becomes $|f_{R0}| < 1.0 \times 10^{-4}$ at 95% confidence limit.

Comparison to previous constraints

I found my results to set constraints at the same order of magnitude but slightly tighter than the results from Wilcox et al. (2015) and the updated XCS-CFHTLenS sample of Section 4.5 (which has deeper weak lensing data), excluding more parameter space using a higher number of clusters as shown in the top and bottom panels of Figure 5.6 respectively. However, despite this large number of clusters, a sample with a more balanced number of clusters in both bins would have benefited this study to reduce the scatter in the profiles. The DESY1-RM sample has an upper bound on $f(R)$ gravity of 5.5×10^{-5} at 95% confidence limit and $f_R(z = 0.33) < 4.5 \times 10^{-5}$ at 95% confidence limit. The time-evolution of the background $f_R(z)$ for a Hu-Sawicki model with $n = 1$ decreases by 22% from $z = 0.33$ to $z = 0$, with a constraint at $z = 0$ of $f(R) < 6 \times 10^{-5}$ at 95% confidence limit. As with Wilcox et al. (2015),

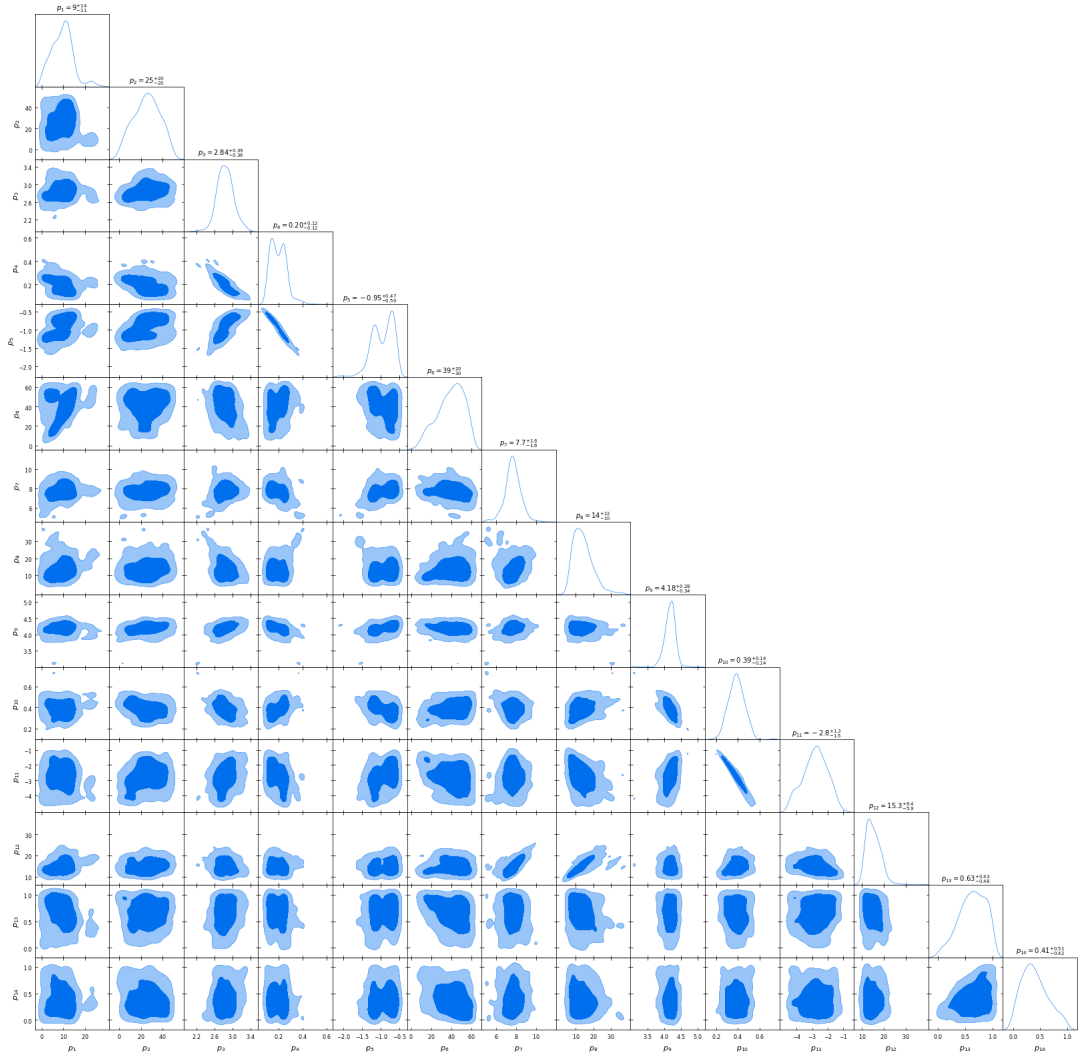

Figure 5.5: The 95% (mid blue region) and the 99% CL (light blue region) 2D marginalised contours for the 14 model parameters T_0^I[keV], $n_0^I[10^{-2}\mathrm{cm}^{-3}]$, b_1^I, r_1^I[Mpc], $M_{200}^I[10^{14}\mathrm{M_{Sun}}]$, c^I, T_0^{II}[keV], $n_0^{II}[10^{-2}\mathrm{cm}^{-3}]$, b_1^{II}, r_1^{II}[Mpc], $M_{200}^{II}[10^{14}\mathrm{M_{Sun}}]$, c^{II}, β_2, $\phi_{\infty,2}$ used in the MCMC analysis for the DES-Y1-RM sample of 96 clusters. The rightmost plots show the 1D likelihood distributions.

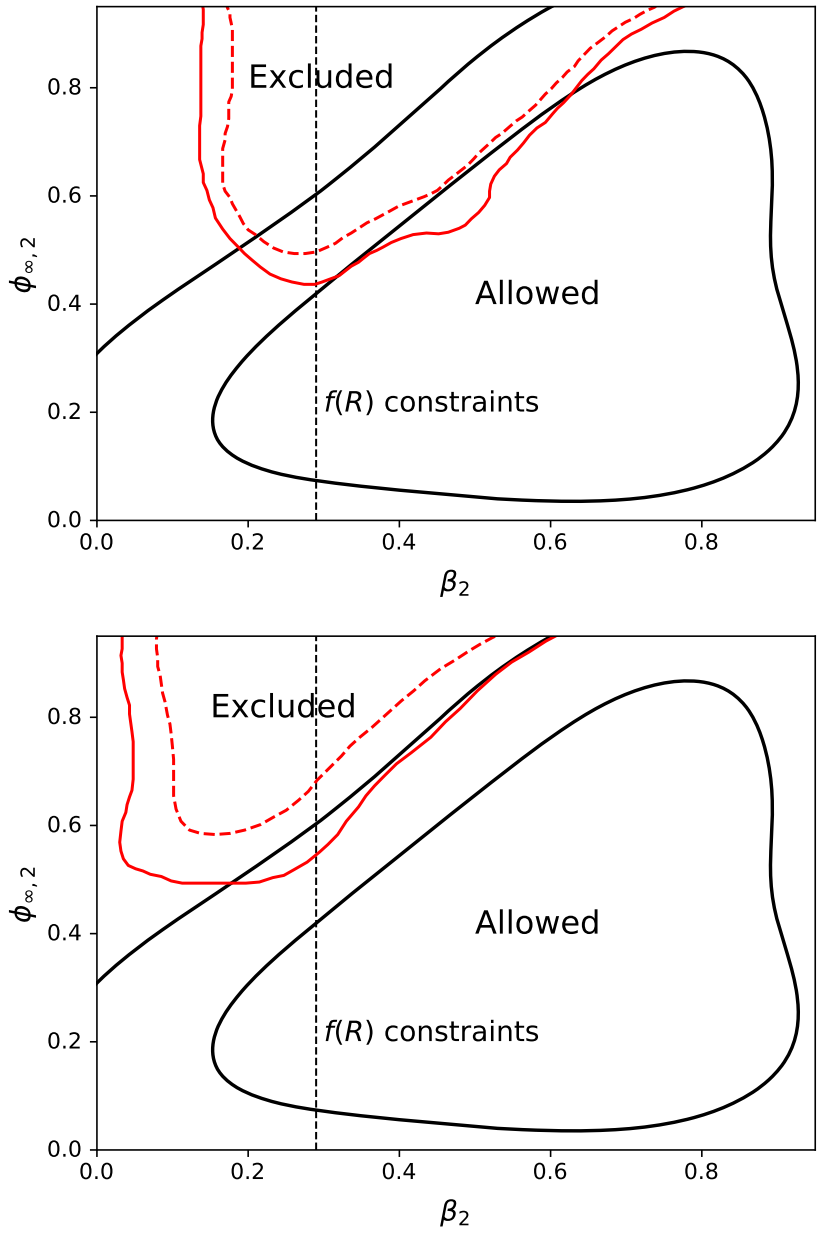

Figure 5.6: *Top*: comparison between the 95% (outer line) and the 99% confidence limit (inner line) constraints for the chameleon model parameters, β_2 and $\phi_{\infty,2}$, for the DES sample from Fig. 5.4 (in black) and in red the 95% (solid line) and 99% (dashed line) from the sample of Wilcox et al. (2015). *Bottom*: comparison between the 95% (outer line) and the 99% confidence limit (inner line) constraints for the chameleon model parameters, β_2 and $\phi_{\infty,2}$, for the DES sample from Fig. 5.4 (in black) and in red the 95% (solid line) and 99% (dashed line) from the updated XCS-CFHTLenS sample of Section 4.5. The vertical dotted line is at $\beta = \sqrt{1/6}$, showing the constraints for $f(R)$ gravity models in both figures.

Source	Scale	$\log_{10}(\lvert f_{R0}\rvert)$
Solar System (Sawicki et al., 2016)	pc	-6
Dwarf galaxies (Jain, Vikram and Sakstein, 2012)	kpc	-6.3
Coma Cluster (Terukina et al., 2014)	Mpc	-4.2
Cluster Abundance (Cataneo et al., 2014)	Mpc	-4.6 ($n = 1$), -3.5 ($n = 3$)
Cluster stack (Wilcox et al., 2015)	Mpc	-4.3 ($n = 1$), -3.9 ($n = 3$)
Updated XCS-CFHTLenS cluster stack (**This work**)	Mpc	-4.3 ($n = 1$), -3.8 ($n = 3$)
DES-Y1-RM cluster stack (**This work**)	Mpc	-4.4 ($n = 1$), -3.9 ($n = 3$)
CMB (Raveri et al., 2014)	Gpc	-3.0

Table 5.1: Comparison of the constraints on $\log f_{R0}$ with previous publications.

I found my results for the DESY1-RM also to be one order of magnitude stronger than those from the CMB (Raveri et al., 2014). My results are slightly stronger at 95% confidence level to the results for the Coma cluster Terukina et al. (2014) which have $|f_R(z)| < 6 \times 10^{-5}$, as mentioned in Section 1.5.5. They are also comparable to (Cataneo et al., 2014) which have $|f_{R0}| < 2.6 \times 10^{-5}$ for $n = 1$, compared with our measurement of $f_{R0} < 3.6 \times 10^{-5}$, and $|f_{R0}| < 3.1 \times 10^{-4}$ for $n = 3$, compared with my measurement of $f_{R0} < 1.0 \times 10^{-4}$ at 95% confidence level. A comparison of these constraints is shown in Table 5.1.

5.5 Conclusions

In this chapter I have employed the methodology originally developed in Wilcox et al. (2015), and then adapted by myself and collaborator Tamosiunas, to constrain modified gravity models using stacked galaxy cluster profiles. However, this time I used a redMaPPer cluster sample of 95 clusters with X-ray data from XCS and weak lensing data from the Dark Energy Survey Year 1 release. As in Chapter 5 I studied the the chameleon screening mechanism by comparing the X-ray profiles to the weak lensing profiles. The MCMC analysis of these profiles produced stronger constraints on the chameleon parameters β and ϕ_∞ compared to the results from Section 4.5.4 (see Table 5.1), excluding a larger area of the parameter space despite being a sample with narrower redshift range and less deep weak lensing data. There are plans to publish the results presented in this Chapter.

5.6 Future work

Future work will involve improving the weak lensing profiles and applications to different modified gravity models. The use of larger samples, as more DES shear data becomes available, will bring tighter constraints on different models upon release of updated lensing catalogues.

5.6.1 Improving the weak lensing profiles

As mentioned in Chapter 3 (Sec. 3.10), future DES+XCS samples will have over a thousand of clusters with weak lensing that will help reducing the error bars in the profile up to at least 2σ. In order to reduce the error bars in the weak lensing profile derived from the method presented in Section 4.3.2, the XPIPE Python package (T. Varga) could be used instead. XPIPE[1] was created to automate work when measuring and calibrating weak lensing shear and mass profiles in wide area lensing surveys such as DES. XPIPE also measures the boost-factor profile (with the $p(z)$ decomposition technique) and estimates errors using a Jackknife method. This package has been broadly used within the DES collaboration to compute γ_t and estimate mass profiles.

5.6.2 Further tests of gravity

In this section I discuss other tests of gravity using large samples of galaxies clusters to forecast constraints for other types of theories of modified gravity. I present a brief summary of the methodology used to constrain different types models, such as: Emergent Gravity (see Sec. 1.5.5), Superfluid dark matter, and the gravitational slip parameter.

Testing gravity in massive, relaxed clusters

Recent work has suggested the possibility of testing Emergent Gravity (Verlinde, 2016) (see Sec. 1.5.5) using the matter densities of relaxed, massive clusters of galaxies using observations from the optical and X-ray wavebands. Zuhone and Sims (2019) recently improved upon previous work (Ettori et al., 2016; Halenka and Miller, 2018) in this area, by including the baryon mass contribution of the brightest cluster galaxy in each system, in addition to total mass profiles from gravitational lensing and mass profiles of the X-ray emitting gas to

[1] https://xpipe.readthedocs.io/en/stable/index.html

predict the dark matter distribution from the observed baryon distribution, and vice-versa. Zuhone and Sims (2019) have shown that the inclusion of the brightest cluster galaxy in this type of analysis improves the agreement with observations in the inner regions of the clusters ($r \leq 10$kpc), at larger radii ($r \sim 100$ kpc). The Emergent Gravity predictions for mass profiles and baryon mass fractions are discrepant with observations by a factor of ~ 2, though the agreement improves at radii near r_{500}. At least in its current form, Emergent Gravity does not appear to reproduce the observed characteristics of relaxed galaxy clusters as well as cold dark matter models. Therefore, a follow up study using a larger sample of clusters could put further contraints in this type of gravity.

Constraints on the gravitational slip

The gravitational slip parameter is a discriminator between large classes of gravity theories at cosmological and astrophysical scales (Sawicki et al., 2016). With the use of galaxy cluster mass profiles, inferred from strong and weak lensing, and by the dynamics of the cluster member galaxies, is possible to reconstruct the gravitational slip parameter η and estimate constrains upon its value. In Pizzuti et al. (2019), the authors explain how galaxy cluster observations can constrain η down to the percent level with just a few tens of clusters by performing a full likelihood statistical analysis. Figure 5.7 was made by Tamosiunas and it shows the constraints on these parameter for the cluster sample from Section 5.1 in the dashed dotted line and the predicted DES-Y1 sample of one thousand clusters in the dotted line, compared against the constraints from Pizzuti et al. (2019). I have the intentions to publish the constraints on the gravitational slip in collaboration with A. Tamosiunas.

Superfluid dark matter

It has recently been proposed, by assuming that dark matter is a superfluid (Berezhiani and Khoury, 2015b), that MOND-like effects can be achieved on small scales while preserving cold dark matter like properties on large scales. However, detailed models within superfluid dark matter (SDM) are yet to be constructed (see for instance (Berezhiani and Khoury, 2015a; Khoury, 2016). The SDM model is defined by two parameters: (i) Λ a mass scale in the Lagrangian of the scalar field that effectively describes the phonons, and it acts as a coupling constant between the phonons and baryons. (ii) m is the mass of the dark matter particles. Based on these parameters. The latter are thought to encompass the largest part of galaxy

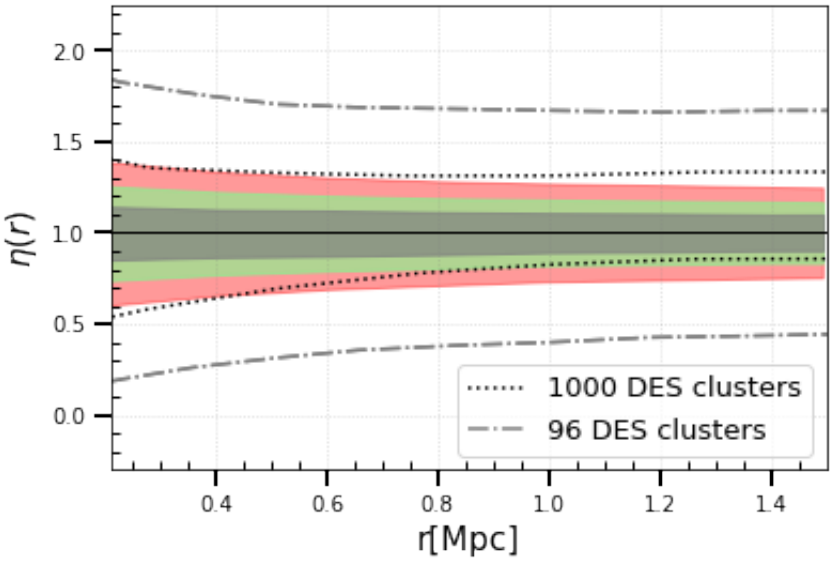

Figure 5.7: Forecast of the gravitational slip constraints on a scale-dependent η as a function of the radius from the centre of the cluster. The different 2σ bands are derived from different numbers of clusters: Red = 15, Green = 30, Dark Green = 45, Yellow = 60 and Violet = 75 clusters respectively from the sample of Pizzuti et al. (2019). The dasdhed dotted and dotted line represent cluster samples from DES. TImage credit Tamosiunas.

clusters. The SDM transition is set in these studies at the radius where the density and pressure of the superfluid and normal phase coincide, neglecting the effect of phonons in the superfluid core. This method was applied to a sample of clusters in (Hodson et al., 2016) to directly compare the SDM predicted mass profiles to data. The results in (Hodson et al., 2016) show that the superfluid formulation can reproduce the X-ray dynamical mass profile of clusters reasonably well, but with a slight under-prediction of the gravity in the central regions. They found that the superfluid formalism is reasonably consistent with clusters.

Future work in superfluid formulation could be successful in describing galaxy clusters, depending on the amount of baryons present in the central cluster galaxy and on the actual effect of phonons. Ideally, more realistic models will be explored, i.e. those that allow for non-sphericity and for a more realistic SDM to normal phase transition.

Chapter 6

Conclusions

Galaxy clusters are the largest gravitationally bound objects in the universe, and thereby provide information on cosmic structure formation. Their mass distribution can be predicted for different cosmologies and different initial densities. By comparing such predictions to the observed cluster mass function, astronomers can constrain cosmological parameters. This thesis combined the information about galaxy clusters from the XMM Cluster Survey (XCS) and the Dark Energy Survey (DES) to obtain a well selected cluster catalogue to derive their optical and X-ray properties and to test modified theories of gravity.

For the first part of this thesis, I described the search for XCS cluster candidates from the second data release within the DES Year 3 region. I obtained and processed three-band optical images to validate my X-ray selected cluster candidates. I designed a classifying exercise for my sample which derived in a catalogue of optically confirmed galaxy clusters. I confirmed the numbers in my catalogue by comparing them to other published catalogues from the literature and data releases from XCS. I then measured the X-ray properties of the catalogue and studied the X-ray temperature - luminosity relation. I adopted a Bayesian framework to constrain this scaling relation. I found my results to be consistent with other cluster samples, with a scaling relation slope, $\alpha = 1.11 \pm 0.01$. While exploring the numbers of serendipitous and targeted clusters in my sample, I found that neither the use of serendipitous nor targeted clusters affected the results beyond the range of uncertainties. My plan is to publish these results. One limiting factor in my sample was the quantity and quality of the X-ray data. By the time this work was produced, the number of XAPA extended detections, with a significant number of photon counts, in the DES region was too small to take full advantage of the wide-area of such survey. Due to this, the number density of clusters

is not consistent across the whole DES Y3 area. However, further data releases from XCS containing more information derived from the XMM archives will be available in the future, providing additional homogeneous and dense cluster candidates in the DES footprint and other wide-area imaging surveys. I look forward to the use of more clusters derived with the use of DES and other larger samples from upcoming surveys such as LSST, to measure scaling relations with greater precision.

For the second part of this thesis, the work begun with the reproduction of the methodology and results of Wilcox et al. (2015). This process involved stacking galaxy cluster profiles to test chameleon gravity. This type of gravity predicts the existence of an additional pressure within clusters, which suppresses the gas component to become more compressed than general relativity predicts. To study this phenomena, I compared the X-ray profile with the weak lensing profile, just like Wilcox et al. (2015) did. After binning the clusters by X-ray temperature, I generated a stacked surface brightness profile and a stacked weak lensing profile using data from XCS and CFHTLenS. I reproduced the constraints of (Wilcox et al., 2015) on the chameleon parameters β and ϕ_∞ that lead to constraints for f_{R0}, a parameter that characterizes $f(R)$ theories. During the reproduction of these results, I realized that 27 of the 58 clusters were not galaxy clusters. I removed and replaced these clusters and expanded the sample by cross-matching XCS clusters candidates with the largest CFTHLenS cluster catalogue available. As result, I obtained a new sample of 77 clusters. I reproduced the same methodology and analysis to find a new set of constraints on the chameleon parameters of β and ϕ_∞ which lead again to constraints for f_{R0} of the same order of magnitude as in previous studies at this scale. To finish this study I used a redMaPPer sample with a larger number of galaxy clusters in the DES Y1 footprint. I produced again a stacked surface brightness profile and a weak lensing profile using data from XCS and DES Y1. In my analysis I found the corresponding set of constraints on β and ϕ_∞ which lead to stronger constraints for f_{R0} than the sample from CFTHLenS by excluding a larger region in the parameter space.

My analysis was once again restricted by the the quantity and quality of the data I used. The DES Y1 shear data covers a significant but small part of the sky, barely comparable to the one from CFHTLenS in terms of coverage but not in terms of deepness. As I explained in this thesis, the DES Y1 shape catalogues are not definite, remaining issues with the calibration and analysis methods are still under further development by DES. However, the shape catalogues from the year 3 and year 5 data releases from DES will contain much more in-

formation, providing a more homogeneous and dense galaxy shapes samples around galaxy clusters. The catalogue of clusters obtained in the first part of this work will contain twice or three times as many clusters with high quality weak lensing data from these data releases. I intend to use these samples to set constraints to different gravitational models.

The potential of galaxy clusters to probe cosmological parameters using wide-area astronomical surveys will produce world leading constraints on cosmological models. To take advantage of the full potential of these surveys it is necessary to fully understand the properties that can be derived from clusters. As part of the doctoral formation several contributions and collaborations with different cluster research groups were made. I carried out different tasks involving data analysis, pipeline development, and high performance computing. I also provided X-ray selected cluster samples, optical imaging and visualization of astrophysical objects, and X-ray temperatures and luminosities from selected clusters. I successfully adapted to collaborate on ten articles, some of them published in prestigious peer-reviewed scientific journals (see Appendix A for abstracts of these articles), two further articles are being planned for future publication.

Appendix A

Contributions and Collaborations

The potential of galaxy clusters to probe cosmological parameters using wide-area astronomical surveys will produce world leading constraints on cosmological models. To take advantage of the full potential of these surveys it is necessary to fully understand the properties that can be derived from clusters. As part of the doctoral formation several contributions and collaborations with different cluster research groups were made. We carried out different tasks involving data analysis, statistical inference, pipeline development, and high performance computing. We also provided X-ray selected cluster samples, optical imaging and visualization of astrophysical objects, and X-ray temperatures and luminosities from selected clusters using XCS3P (see Section 2.2.4). We successfully adapted to collaborate on ten articles, some of them published in prestigious peer-reviewed scientific journals (see Appendix A for abstracts of these articles), two further are being planned for future publication.

A.1 XCS contributions

A.1.1 Joint modelling of the Luminosity - Temperature scaling relation for clusters and groups of galaxies

A sample of 533 clusters and groups was prepared to study the X-ray luminosity-temperature relation (Eqn. 1.19) more thoroughly in (Ebrahimpour et al., 2018). The sources were mostly from XCS but also identified in SDSS using the redMaPPer algorithm. With redshifts spanning within the range $(0.1 < z < 0.6)$. It was allowed for the redshift evolution of the normalisation and for the intrinsic scatter of the $L_X - T_X$ relation, the possibility of a temperature-

dependent change-point in the exponent of such relation. However, there was not found any statistical support for deviations from the usual modelling of the $L_X - T_X$ relation as a single power-law, where the normalisation evolves self-similarly and the scatter remains constant with time. Nevertheless, assuming a priori the existence of the type of deviations considered, then faster evolution than the self-similar expectation for the normalisation of the $L_X - T_X$ relation is favoured, as well as a decrease with redshift in the scatter about the $L_X - T_X$ relation. The results also indicate an increase in the power-law exponent of the $L_X - T_X$ relation when moving from the group to the cluster regime, and faster evolution in the former with respect to the later, driving the temperature-dependent change-point towards higher values with redshift.

A.1.2 A RedMaPPer analysis of the second XCS data release in the SDSS DR8 footprint

For this paper (which is still in preparation), the construction and analysis of a cluster subsample of the first redMaPPer cluster catalogue of SDSS DR8 data (see Sec. 2.5) matched to the XCS. Details about the current state of the reduction process of XCS and the updated version of XCS3P (see Sec. 2.2.4) are covered. In the results, the best fit for the temperature-luminosity ($T_X - L_X$) and temperature-richness ($T_X - \lambda$) were obtained using clusters with a robust temperature measurement only. The best-fit values for each relation are consistent to the self-similar evolution and consistent with previous studies. The sample was splitted between targeted and serendipitously detected clusters to repeat this analysis, only to find that there was no difference in the derived scaling relations.

A.2 DES contributions

A.2.1 Dark Energy Survey Year 1 Results: Calibration of Cluster Mis-centering in the redMaPPer Catalogs

The determination of the centre of a galaxy cluster from optical cluster finding algorithms can offset from prescriptions or N-body definitions of its host halo center. These offsets reverberate the the richness measurements and the weak lensing shear profile around the clusters. This paper models the centering performance of the redMaPPer cluster finding algorithm using X-ray observations of redMaPPer selected clusters. By assuming the X-ray

emission peaks as the true halo centres, and studying their offsets to the redMaPPer centres, it was found that $\sim 75 \pm 8\%$ of the redMaPPer clusters are well centered. The mis-centered offset follows a Gamma distribution. These mis-centering offsets cause a systematic under-estimation of cluster richness relative to the well-centered clusters, for which we propose a descriptive model. The results of (Zhang et al., 2019a) enable the DES Y1 cluster cosmology analysis by characterizing the necessary corrections to both the weak lensing and richness abundance functions of the DES Y1 redMaPPer cluster catalog.

A.2.2 Mass Variance from Archival X-ray Properties of Dark Energy Survey Year-1 Galaxy Clusters

Using archival X-ray observations and a log-normal population model, Farahi et al. (2019) estimate constraints on the intrinsic scatter in halo mass at fixed optical richness for a galaxy cluster sample identified in Dark Energy Survey Year-One (DES-Y1) data with the redMaPPer algorithm. The scaling behaviour for clusters with X-ray temperatures, T_X, and optical richness, Λ_{RM}, was examined in the redshift range $0.2 < z < 0.7$. X-ray temperatures are obtained from Chandra and XMM observations for 58 and 110 redMaPPer systems, respectively.

A.2.3 Galaxies in X-ray Selected Clusters and Groups in Dark Energy Survey Data II: Hierarchical Bayesian Modeling of the Red-Sequence Galaxy Luminosity Function

For the work in (Zhang et al., 2019b), around ~ 100 X-ray selected clusters in DES-SV data were selected to constrain the luminosity function (LF) of cluster red sequence galaxies as a function of redshift within the range $(0.1 < z < 1.05)$. A hierarchical Bayesian model was applied to fit the LF by employing a Schecter model to each cluster galaxy. A weak and statistically insignificant $(\sim 1.9\sigma)$ evolution was found in the faint end slope α versus redshift. Also no dependence in α or m_{Sun} with the X-ray inferred cluster masses was found. However, the amplitude of the LF as a function of cluster mass is constrained to $\sim 20\%$ precision. The correlation between the LF and cluster mass was used to provide an improved estimate of the individual cluster masses as well as the scatter in true mass given the X-ray inferred masses.

A.2.4 Dark Energy Survey Year 1 Results: Weak Lensing Mass Calibration of redMaPPer Galaxy Clusters

The mass–richness scaling relation of redMaPPer galaxy clusters identified in the DES-Y1 data is studied in (Mcclintock et al., 2017) using WL. The sample was split clusters into 4×3 bins of richness Λ and redshift z for $\Lambda > 20$ and $0.2 < z < 0.65$ to measure the mean masses of these bins using their stacked WL signal. By modeling the scaling relation the normalization of the scaling relation was constrained at the 5.0 per cent level, producing the tightest measurements of the normalization and richness scaling index made to date from using WL. The analysis accounts for several sources of systematic error (e.g. shear and photometric redshift errors among others) characterized by a semi-analytic covariance matrix. The results are agreement but with smaller uncertainties than previous measurements, which augurs well for the power of the DES cluster survey as a tool for precision cosmology and upcoming galaxy surveys such as LSST, Euclid and WFIRST.

A.2.5 The redMaPPer galaxy cluster catalog from DES Science Verification data

This work (Rykoff et al., 2016) describes updates to the redMaPPer algorithm. The updated algorithm is applied to 150 squared degrees of Science Verification (SV) data from the DES, and to the SDSS DR8 photometric data set. The DES- SV catalog is locally volume limited, and contains 786 clusters with richness $\Lambda > 20$ and $0.2 < z < 0.9$. The DR8 catalog consists of 26,311 clusters with $0.08 < z < 0.6$. X-ray data from Chandra and XMM and Sunyaev-Zeldovich from the South Pole Telescope was used to show that the centering performance and mass richness scatter are consistent with expectations based on prior runs of redMaPPer on SDSS data. It was shown that the redMaPPer photo-z and richness estimates are relatively insensitive to imperfect star/galaxy separation and small-scale star masks.

A.2.6 Stellar mass as a galaxy cluster mass proxy: application to the Dark Energy Survey redMaPPer clusters

In this paper, Palmese et al. (2020) introduces a galaxy cluster mass observable, μ_*, based on the stellar masses of cluster members, and also present results for the DES-Y1 observations. Stellar masses are computed using a Bayesian Model Averaging method, and are validated for DES data using simulations and COSMOS data. We show that μ_* works as a promising

mass proxy by comparing our predictions to X–ray measurements. We measure the X–ray temperature–μ_* relation for a total of 150 clusters matched between the wide–field DES-Y1 redMaPPer catalogue and Chandra and XMM archival observations, spanning the redshift range $0.1 < z < 0.7$. For a scaling relation which is linear in logarithmic space, we find a slope of $\alpha = 0.488 \pm 0.043$ and a scatter in the X–ray temperature at fixed μ_* for the joint sample. By using the halo mass scaling relations of the X–ray temperature from the Weighing the Giants program, we further derive the μ_*–conditioned scatter in mass, finding $\sigma_{\ln M|\mu_*} = 0.26^{+0.15}_{-0.10}$. These results are competitive with well–established cluster mass proxies used for cosmological analyses, showing that μ can be used as a reliable and physically motivated mass proxy to derive cosmological constraints.

A.2.7 Galaxy populations and dynamical states of 289 SPT clusters in DES Year 3 footprint

A sample of 289 clusters from the South Pole Telescope (SPT) Sunyaev-Zeldovich (SZ) efect survey (SPT-SZ) with images from DES-Y3 were selected to characterize their dynamical state (Zenteno et al., 2020). The aim was to examine the spatial offsets between the BCG and the center of the gas distribution as as traced by the SPT-SZ centroid and by the X-ray centroid/peak position. It is shown the radial distribution of the offsets provides no evidence that SPT-SZ selected cluster samples include a higher fraction of mergers than X-ray selected cluster samples. The most disturbed systems were selected to compare their cluster galaxy populations to 41 relaxed systems. By examining their stacked luminosity functions it was found that for low redshift clusters that m^* and α are in agreement, while for high redshift clusters m^* is brighter and α is steeper for merging clusters than for relaxed systems.

Appendix B

The XCS DR2 - DES Y3 catalogue

An excerpt of the DES-XCS catalogue is shown in Table B.1. The first column corresponds to the the XCS name, the second to the DES name, the third and fourth are the X-ray cluster centre coordinates, column 5 is the number of photon counts, columns 6 and 7 contain the cluster redshift and its source respectively, columns 8, 9 and 10 provide the the X-ray temperature with its lower and upper limits respectively, while columns 11, 12, 13 are the X-ray luminosity with its lower and upper limit respectively.

XCS Name	DES Name	Photon Counts	redshift	redshift source	$T_{X,500}$	$T_{X,500,l}$	$T_{X,500,u}$	$L_{bol,500}$	$L_{bol,500,l}$	$L_{bol,500,u}$
XMMXCS J032835.9-554239.3	DESJ032836.0-554239.3	23747.992	0.0844	SPT	4.70293	4.60344	4.80572	3.97739	3.932956336	4.023314404
XMMXCS J003317.9-212459.6	DESJ003318.0-212459.6	229.08443	0.17	zCluster	1.12196	0.961104	1.36807	0.0703676	0.061977701	0.078954867
XMMXCS J002944.5+045223.5	DESJ002944.5+045223.6	475.80005	0.206231	NED	1.46215	1.39233	1.5426	0.139694	0.135347242	0.144087618
XMMXCS J003346.3-431729.7	DESJ003346.3-431729.8	3703.6329	0.220131	redMaPPer	2.2913	2.19243	2.40001	0.54869	0.537984582	0.5601911
XMMXCS J034137.6-345811.0	DESJ034137.7-345811.0	268.63802	0.30463	redMaPPer	1.5871	1.20552	7.55561	0.315395	0.256763019	0.402685138
XMMXCS J003428.0-431854.2	DESJ003428.1-431854.2	3373.0639	0.4	XCS-DR1	3.18996	3.02689	3.36622	1.7292	1.700832946	1.755908632
XMMXCS J234231.5-562105.9	DESJ234231.5-562106.0	325.5183	0.414	XLSSC 540	3.16312	2.76493	3.68313	1.0825	1.037003146	1.124034077
XMMXCS J011902.8+032352.3	DESJ011902.9+032352.4	2089.3889	0.456822	redMaPPer	3.37884	2.90823	3.96501	1.54405	1.432498106	1.656476969
XMMXCS J025733.1-232342.3	DESJ025733.1-232342.4	235.88966	0.46	zCluster	2.71125	1.85733	5.10482	0.368456	0.324445424	0.412941266
XMMXCS J233633.8-524400.3	DESJ233633.9-524400.3	290.74783	0.541357	redMaPPer	2.2431	1.87134	2.77834	0.803298	0.751695304	0.852934906
XMMXCS J232727.7-020439.2	DESJ232727.7-020439.2	1555.6804	0.705919	redMaPPer	8.21465	7.35366	9.23166	62.6225	59.09885287	66.12295239
XMMXCS J053447.9-543547.6	DESJ053447.9-543547.7	287.90267	0.756916	redMaPPer	3.14032	2.69646	3.70022	5.6894	5.250630597	6.102721659
XMMXCS J020235.7-064356.0	DESJ020235.8-064356.0	201.99428	0.886	XLSSC 094	2.62291	2.12097	3.33031	2.68377	2.383926037	2.965546102
XMMXCS J022156.9-034000.4	DESJ022157.0-034000.5	514.5485	0.921982	redMaPPer	4.16383	3.05603	6.20444	1.20014	1.115070354	1.275768631
XMMXCS J213656.4-630719.4	DESJ213656.4-630719.4	2160.1332	0.926	SPT	4.6517	4.18114	5.22202	4.09097	3.940536447	4.219651036

Table B.1: An excerpt of the DES-XCS catalogue.

Appendix C

The updated XCS - CFHTLenS cluster sample

The updated XCS-CFHTLenS sample of 77 galaxy clusters described in Section 4.5 is shown in Table C.1. The first column corresponds to the the XCS name, the second to the number of photon counts, the third and fourth to the X-ray temperature ($T_{X,500}$) and the redshift respectively, the fifth column contains a note specifying if the cluster comes from the original sample of Wilcox et al., 2015 or was added.

Table C.1: The new XCS-CFHTLenS sample.

XCS Name	Photon Counts	$T_{X,500}$	redshift	Note
XMMXCS J021529.1-044039.9	17.47263	2.28711	0.33	Wilcox et al.
XMMXCS J021939.3-040024.9	111.06057	1.52393	0.29	Wilcox et al.
XMMXCS J021722.3-053920.9	112.86442	2.44354	0.561	Wilcox et al.
XMMXCS J023052.4-045123.5	117.13661	1.48567	0.2955	Wilcox et al.
XMMXCS J022433.1-040030.5	122.06958	3.34106	0.661	Wilcox et al.
XMMXCS J022246.3-035151.2	122.97052	1.26847	0.155	Wilcox et al.
XMMXCS J021843.7-053257.6	124.81672	1.26311	0.404	Wilcox et al.
XMMXCS J021719.2-040333.2	127.71973	1.29865	0.672	Wilcox et al.
XMMXCS J022352.2-082125.6	137.12507	3.81559	0.215	Wilcox et al.
XMMXCS J021452.5-042324.1	203.17724	2.43723	0.7	Added cluster
XMMXCS J020304.4-070604.5	209.75947	1.58048	0.4	Added cluster
XMMXCS J021527.9-053319.2	234.71071	2.64266	0.285	Wilcox et al.
XMMXCS J021228.7-053116.5	237.48681	3.05498	0.3	Added cluster
XMMXCS J022607.8-041843.2	242.88115	2.38293	0.3905	Wilcox et al.
XMMXCS J020221.8-055400.6	259.96047	1.63462	0.2	Added cluster
XMMXCS J221211.4-000809.1	260.35772	3.0242	0.4	Added cluster
XMMXCS J021250.8-043601.2	272.47374	1.48525	0.2	Added cluster

XMMXCS J022634.8-040409.2	279.88567	1.73734	0.4	Added cluster
XMMXCS J020232.1-073343.7	282.3563	3.98308	0.552	Wilcox et al.
XMMXCS J020232.1-073343.7	282.3563	6.8613	0.5	Added cluster
XMMXCS J022732.9-055731.1	290.5598	2.95529	0.2	Added cluster
XMMXCS J020846.4-042608.2	291.91585	2.95088	0.7765	Wilcox et al.
XMMXCS J020353.2-050146.0	299.36584	4.17995	0.6	Added cluster
XMMXCS J141137.8+523733.6	300.0664	1.08209	0.2	Added cluster
XMMXCS J022812.6-100538.6	304.04935	1.86589	0.1755	Wilcox et al.
XMMXCS J020301.0-045952.7	315.61989	2.30981	0.5	Added cluster
XMMXCS J023026.7-043444.5	318.92649	3.02254	0.4	Added cluster
XMMXCS J021227.9-060440.2	320.50941	1.30656	0.4	Added cluster
XMMXCS J022812.4-043234.6	320.55721	3.14045	0.501	Wilcox et al.
XMMXCS J022037.2-054214.9	321.54644	2.23425	0.8185	Wilcox et al.
XMMXCS J021252.9-061206.3	321.9474	3.08234	0.4	Added cluster
XMMXCS J023143.3-072800.2	325.02016	3.63374	0.204	Wilcox et al.
XMMXCS J022328.5-085208.3	339.89138	2.9854	0.2	Added cluster
XMMXCS J022401.9-050528.4	341.65538	1.79098	0.325	Wilcox et al.
XMMXCS J022803.3-045053.3	345.67267	2.85272	0.4	Added cluster
XMMXCS J022832.2-094931.0	347.82396	4.40242	0.4	Added cluster
XMMXCS J140955.7+523312.7	353.5806	1.48522	0.2	Added cluster
XMMXCS J022136.5-051817.5	354.74786	1.94483	0.8	Added cluster
XMMXCS J020719.9-044935.6	355.31006	2.17109	0.3	Added cluster
XMMXCS J023205.5-053313.9	402.53896	4.16385	0.6	Added cluster
XMMXCS J020744.0-060955.2	448.81798	3.8574	0.35	Wilcox et al.
XMMXCS J020611.2-061130.6	457.41173	3.99315	0.8755	Wilcox et al.
XMMXCS J020611.2-061130.6	457.41173	3.8245	0.9	Added cluster
XMMXCS J022512.2-062305.1	486.81709	3.04602	0.3	Added cluster
XMMXCS J021444.1-034914.9	491.79977	3.49583	0.7	Added cluster
XMMXCS J022156.9-034000.4	514.5485	1.43936	0.1	Wilcox et al.
XMMXCS J021428.3-062722.9	514.85808	3.91173	0.3	Wilcox et al.
XMMXCS J085448.0-012144.6	578.36283	2.9822	0.4	Added cluster
XMMXCS J022319.9-052710.7	583.84914	1.15937	0.3	Added cluster
XMMXCS J022456.3-050755.6	608.98374	0.710352	0.1245	Wilcox et al.
XMMXCS J021500.9-035429.9	614.30267	1.59162	0.2	Wilcox et al.
XMMXCS J021500.9-035429.9	614.30267	2.08952	0.2	Added cluster
XMMXCS J090139.3-015856.7	614.69483	4.98713	0.4	Added cluster
XMMXCS J022610.6-045811.3	639.16303	0.758475	0.0965	Wilcox et al.
XMMXCS J022610.6-045811.3	639.16303	0.758475	0.0965	Wilcox et al.
XMMXCS J021529.0-044052.8	649.2794	3.04141	0.4	Added cluster
XMMXCS J021322.3-060553.1	661.22895	3.89726	0.7	Added cluster
XMMXCS J140936.8+540800.5	693.07189	3.17491	0.4	Added cluster
XMMXCS J022530.4-041421.8	750.72245	1.8221	0.2	Added cluster
XMMXCS J020647.7-065648.9	756.18511	3.37537	0.5	Added cluster
XMMXCS J022359.2-083543.4	761.49191	4.20171	0.3	Added cluster
XMMXCS J023346.9-085055.7	800.40264	2.018	0.3	Added cluster
XMMXCS J021057.8-061156.8	812.07115	3.25533	0.5	Added cluster

XMMXCS J022505.1-095016.2	904.08898	4.63701	0.95	Wilcox et al.
XMMXCS J022740.4-045130.0	942.37422	1.65936	0.3195	Wilcox et al.
XMMXCS J023337.6-053025.1	951.64118	6.06547	0.5	Added cluster
XMMXCS J021612.5-041426.2	1006.332	2.46491	0.2	Added cluster
XMMXCS J085216.4-010139.3	1025.7585	5.07679	0.5	Added cluster
XMMXCS J021226.8-053734.6	1109.9946	4.35654	0.315	Wilcox et al.
XMMXCS J021524.4-034322.1	1195.8672	7.91702	0.8755	Wilcox et al.
XMMXCS J023147.1-045233.0	1264.304	7.14448	0.7	Added cluster
XMMXCS J022433.9-041432.7	1733.6241	1.43897	0.3	Added cluster
XMMXCS J085216.2-053347.9	1876.4857	4.74288	0.2	Added cluster
XMMXCS J022738.6-031758.9	2213.7837	5.17887	0.8378	Wilcox et al.
XMMXCS J141446.9+544709.1	5188.7075	9.80947	0.6	Added cluster
XMMXCS J022145.6-034613.7	11840.913	5.27889	0.5	Added cluster
XMMXCS J023142.5-045254.5	22873.282	4.96965	0.2135	Wilcox et al.
XMMXCS J023142.5-045254.5	22873.282	4.58288	0.2	Added cluster

Bibliography

Abbott, Timothy et al. (2016). 'The Dark Energy Survey: more than dark energy–an overview'. In: *Monthly Notices of the Royal Astronomical Society* 460.2, pp. 1270–1299.

Abbott, TMC et al. (2018). 'The Dark Energy Survey: Data Release 1'. In: *The Astrophysical Journal Supplement Series* 239.2, p. 18.

Ade, Peter AR et al. (2014). 'Planck 2013 results. XXIX. The Planck catalogue of Sunyaev-Zeldovich sources'. In: *Astronomy & Astrophysics* 571, A29.

Ade, Peter AR et al. (2016). 'Planck 2015 results-xiii. Cosmological parameters'. In: *Astronomy & Astrophysics* 594, A13.

Aihara, Hiroaki et al. (2014). 'Elinor Medezinski 2 , Shoken Miyama 17,30 , Rieko Momose 22 , Anupreeta More 11 , Surhud More 11 , Shiro Mukae 21 , Ryoma Murata 11,1 , Hitoshi Murayama 11,31,32 , Tohru Nagao 29 , Fumiaki Nakata 16 , Mana Niida 33 , Hiroko Niikura 1,11'. In: *Astronomical Society of Japan* 18.0, pp. 1–28. DOI: 10.1093/pasj/xxx000. URL: https://hsc-release.mtk.nao.ac.jp..

Allen, Steven W., August E. Evrard and Adam B. Mantz (2011). 'Cosmological Parameters from Observations of Galaxy Clusters'. In: DOI: 10.1146/annurev-astro-081710-102514.

Andreon, S et al. (2016). 'The amazing diversity in the hot gas content of an X-ray unbiased massive galaxy clusters sample'. In: *Astronomy & Astrophysics* 585, A147.

Arnaud, A.. (1996). 'XSPEC'. In: *Astronomical Data Analysis Software and Systems* 101, p. 17. URL: http://adsabs.harvard.edu/abs/1996ASPC..101...17A.

Arnaud, Monqiue, E Pointecouteau and GW Pratt (2005). 'The structural and scaling properties of nearby galaxy clusters-II. The M–T relation'. In: *Astronomy & Astrophysics* 441.3, pp. 893–903.

Arnold, Christian, Ewald Puchwein and Volker Springel (2014). 'Scaling relations and mass bias in hydrodynamical f (R) gravity simulations of galaxy clusters'. In: *MNRAS* 440, pp. 833–842. URL: https://oup.silverchair-cdn.com/oup/backfile/Content_public/Journal/mnras/440/1/10.1093_mnras_stu332/3/stu332.pdf?Expires=2147483647&Signature=4pv3GajyUqc9yr8LYrQsLlg8Nju5xSG7xR20XCKu0wWyAeYDOeQnf5jw8e0vYsF2u64X-9e2gRw-NrXGjWzYO8Km5-PpINurTkbQit10owI1RQ97.

Bartelmann, Matthias (1996). *Arcs from a Universal Dark-Matter Halo Profile*. Tech. rep. URL: https://arxiv.org/pdf/astro-ph/9602053.pdf.

— (2010). *Gravitational Lensing*. Tech. rep. URL: https://arxiv.org/pdf/1010.3829.pdf.

Berezhiani, Lasha and Justin Khoury (2015a). 'Dark Matter Superfluidity and Galactic Dynamics'. In: DOI: 10.1016/j.physletb.2015.12.054. URL: http://arxiv.org/abs/1506.07877http://dx.doi.org/10.1016/j.physletb.2015.12.054.

— (2015b). 'Theory of dark matter superfluidity'. In: *Physical Review D* 92.10, p. 103510. ISSN: 1550-7998. DOI: 10.1103/PhysRevD.92.103510. URL: https://link.aps.org/doi/10.1103/PhysRevD.92.103510.

Bertin, E. 'STIFF v2.2 User's guide'. In:

Bertin, Emmanuel and Stephane Arnouts (1996). 'SExtractor: Software for source extraction'. In: *Astronomy and Astrophysics Supplement Series* 117.2, pp. 393–404.

Bleem, L. E. et al. (2014). 'Galaxy Clusters Discovered via the Sunyaev-Zel'dovich Effect in the 2500-square-degree SPT-SZ survey'. In: DOI: 10.1088/0067-0049/216/2/27. URL: http://arxiv.org/abs/1409.0850http://dx.doi.org/10.1088/0067-0049/216/2/27.

Boulade, O. et al. (2003). 'MegaCam: the new Canada-France-Hawaii Telescope wide-field imaging camera'. In: *Instrument Design and Performance for Optical/Infrared Ground-based Telescopes*. Ed. by M. Iye and A. F. M. Moorwood. Vol. 4841. Pp. 72–81. DOI: 10.1117/12.459890.

Buchdahl, H A (1970). 'Non-linear lagrangians and cosmological theory'. In: URL: http://articles.adsabs.harvard.edu/cgi-bin/nph-iarticle_query?1970MNRAS.150...1B&data_type=PDF_HIGH&whole_paper=YES&type=PRINTER&filetype=.pdf.

Burns, Jack O, Samuel W Skillman and Brian W O'shea (2010). *Galaxy Clusters at the Edge: Temperature, Entropy, and Gas Dynamics at the Virial Radius*. Tech. rep.

Carlstrom, J E et al. (2011). *The 10 Meter South Pole Telescope*. Tech. rep. URL: https://arxiv.org/pdf/0907.4445.pdf.

Cataneo, Matteo et al. (2014). 'New constraints on $f(R)$ gravity from clusters of galaxies'. In: DOI: 10.1103/PhysRevD.92.044009. URL: http://arxiv.org/abs/1412.0133http://dx.doi.org/10.1103/PhysRevD.92.044009.

Cervantes-Cota, Jorge L. and George Smoot (2011). 'Cosmology today–A brief review'. In: *American Institute of Physics Conference Series*. Ed. by Luis Arturo Ureña-López et al. Vol. 1396. American Institute of Physics Conference Series, pp. 28–52. DOI: 10.1063/1.3647524. arXiv: 1107.1789 [astro-ph.CO].

Chernin, A D et al. (2012). 'Dark energy and extended dark matter halos'. In: *A&A* 539. DOI: 10.1051/0004-6361/201117143. URL: https://www.aanda.org/articles/aa/pdf/2012/03/aa17143-11.pdf.

Chernoff, David F and S Djorgovski (1989). *AN ANALYSIS OF THE DISTRIBUTION OF GLOBULAR CLUSTERS WITH POSTCOLLAPSE CORES IN THE GALAXY*. Tech. rep., pp. 904–918. URL: http://articles.adsabs.harvard.edu/cgi-bin/nph-iarticle_query?1989ApJ...339..904C&data_type=PDF_HIGH&whole_paper=YES&type=PRINTER&filetype=.pdf.

Collaboration, SDSS, FD Albareti and CA Prieto (2016). 'The Thirteenth Data Release of the Sloan Digital Sky Survey: First Spectroscopic Data from the SDSS-IV Survey MApping Nearby Galaxies at Apache Point Observatory'. In: *ArXiv e-prints (Aug. 2016)*.

Costanzi, M et al. (2018). 'Dark Energy Survey year 1 results: methods for cluster cosmology and application to the SDSS'. In: *arXiv preprint arXiv:1810.09456*.

Dalton, Gavin (2009). 'Baryonic acoustic oscillations'. In: *Astrophysics and Space Science Proceedings*. ISBN: 9780521518888. DOI: 10.1007/978-1-4020-9190-2{_}24.

Ebeling, H, A C Edge and J P Henry (2001). *MACS: A quest for the most massive galaxy clusters in the universe*. Tech. rep. URL: https://arxiv.org/pdf/astro-ph/0009101.pdf.

Ebrahimpour, Leyla et al. (2018). *The XMM Cluster Survey: joint modelling of the L X T scaling relation for clusters and groups of galaxies*. Tech. rep., pp. 1–18. URL: http://nxsa.esac.esa.int.

Eckmiller, HJ, DS Hudson and TH Reiprich (2011). 'Testing the low-mass end of X-ray scaling relations with a sample of Chandra galaxy groups'. In: *Astronomy & Astrophysics* 535, A105.

Einstein, A. (1916). 'Die Grundlage der allgemeinen Relativitätstheorie'. In: *Annalen der Physik* 354, pp. 769–822. DOI: 10.1002/andp.19163540702.

Ettori, S. et al. (2016). 'Dark matter distribution in X-ray luminous galaxy clusters with Emergent Gravity'. In: DOI: 10.1093/mnrasl/slx074. URL: http://arxiv.org/abs/1612.07288http://dx.doi.org/10.1093/mnrasl/slx074.

Ettori, Stefano (2000). 'β-model and cooling flows in X-ray clusters of galaxies'. In: *Monthly Notices of the Royal Astronomical Society*. ISSN: 00358711. DOI: 10.1046/j.1365-8711.2000.03664.x. arXiv: 0005224v1 [astro-ph].

Farahi, A. et al. (2019). 'Mass Variance from Archival X-ray Properties of Dark Energy Survey Year-1 Galaxy Clusters'. In: URL: http://arxiv.org/abs/1903.08042.

Foreman-Mackey, Daniel et al. (2012). 'emcee: The MCMC Hammer'. In: DOI: 10.1086/670067. URL: http://arxiv.org/abs/1202.3665http://dx.doi.org/10.1086/670067.

Freeman, P E et al. (2001). *A Wavelet-Based Algorithm for the Spatial Analysis of Poisson Data*. Tech. rep. URL: http://asc.harvard.edu/ciao/..

Friedmann, A. (1922). 'Über die Krümmung des Raumes'. In: *Zeitschrift fur Physik* 10, pp. 377–386. DOI: 10.1007/BF01332580.

Frieman, Joshua, Michael Turner and Dragan Huterer (2008). 'Dark Energy and the Accelerating Universe'. In: DOI: 10.1146/annurev.astro.46.060407.145243.

Ghigna, Sebastiano et al. (1998). 'Dark matter haloes within clusters'. In: *Monthly Notices of the Royal Astronomical Society* 300.1, pp. 146–162.

Gilks, Walter R, Sylvia Richardson and David Spiegelhalter (1995). *Markov chain Monte Carlo in practice*. Chapman and Hall/CRC.

Giodini, S. et al. (2013). *Scaling relations for galaxy clusters: Properties and evolution*. DOI: 10.1007/s11214-013-9994-5.

Gitti, Myriam, Fabrizio Brighenti and Brian R McNamara (2012). 'Evidence for AGN feedback in galaxy clusters and groups'. In: *Advances in Astronomy* 2012.

Gladders, Michael D. and H. K. C. Yee (2000). *A New Method For Galaxy Cluster Detection I: The Algorithm*. Tech. rep. DOI: 10.1086/301557.

Gunn, James E et al. (2006). *The 2.5 m Telescope of the Sloan Digital Sky Survey*. Tech. rep. URL: https://arxiv.org/pdf/astro-ph/0602326v1.pdf.

Halenka, Vitali and Christopher J. Miller (2018). 'Testing Emergent Gravity with mass densities of galaxy clusters'. In: URL: http://arxiv.org/abs/1807.01689.

Hao, Jiangang et al. (2010). 'A GMBCG galaxy cluster catalog of 55,424 rich clusters from SDSS DR7'. In: *The Astrophysical Journal Supplement Series* 191.2, p. 254.

Heymans, Catherine et al. (2012). *CFHTLenS: The Canada-France-Hawaii Telescope Lensing Survey*. Tech. rep. 0000, p. 5. URL: http://terapix.iap.fr/cplt/T0006-doc.pdf.

Hildebrandt, H et al. (2016). *KiDS-450: Cosmological parameter constraints from tomographic weak gravitational lensing*. Tech. rep., pp. 1–49. URL: http://www.lsst.org/.

Hilton, Matt et al. (2017). 'The Atacama Cosmology Telescope: The Two-Season ACTPol Sunyaev-Zel'dovich Effect Selected Cluster Catalog'. In: DOI: 10.3847/1538-4365/aaa6cb. URL: http://arxiv.org/abs/1709.05600http://dx.doi.org/10.3847/1538-4365/aaa6cb.

Hodson, Alistair et al. (2016). 'Galaxy Clusters in the Context of Superfluid Dark Matter'. In: DOI: 10.1051/0004-6361/201630069. URL: http://arxiv.org/abs/1611.05876http://dx.doi.org/10.1051/0004-6361/201630069.

Hoekstra, H. (2013). 'Weak gravitational lensing'. In: *arXiv e-prints*, arXiv:1312.5981, arXiv:1312.5981. arXiv: 1312.5981 [astro-ph.CO].

Honscheid, K et al. (2008). *The Dark Energy Camera (DECam)*. Tech. rep. URL: https://arxiv.org/pdf/0810.3600.pdf.

Hood, R J and R G Mann (2017). 'Characterizing the optical properties of galaxy clusters with GMPhoRCC'. In: *MNRAS* 469, pp. 3851–3871. DOI: 10.1093/mnras/stx940. URL: https://academic.oup.com/mnras/article-abstract/469/4/3851/3747499.

Howell, D. Andrew (2011). *Type Ia supernovae as stellar endpoints and cosmological tools*. DOI: 10.1038/ncomms1344.

Hu, Wayne (2002). 'CMB Temperature and Polarization Anisotropy Fundamentals'. In: DOI: 10.1016/S0003-4916(02)00022-2.

Hu, Wayne and Andrey V. Kravtsov (2002). 'Sample Variance Considerations for Cluster Surveys'. In: DOI: 10.1086/345846. URL: http://arxiv.org/abs/astro-ph/0203169http://dx.doi.org/10.1086/345846.

Hu, Wayne and Ignacy Sawicki (2007). *Models of f (R) Cosmic Acceleration that Evade Solar-System Tests*. Tech. rep. URL: https://arxiv.org/pdf/0705.1158.pdf.

Hudelot, Patrick et al. (2012). *T0007 : The Final CFHTLS Release*. Tech. rep. URL: http://www.cfht.hawaii.edu/Science/CFHTLS/.

Huff, Eric M and Rachel Mandelbaum (2017). *METACALIBRATION: DIRECT SELF-CALIBRATION OF BIASES IN SHEAR MEASUREMENT*. Tech. rep. URL: http://kids.strw.leidenuniv.nl.

Huterer, Dragan and Daniel L Shafer (2018). *Dark energy two decades after: Observables, probes, consistency tests*. Tech. rep.

Im, Eric Iksoon (1996). *A Note On Derivation of the Least Squares Estimator*. Working Papers 199611. University of Hawaii at Manoa, Department of Economics. URL: https://ideas.repec.org/p/hai/wpaper/199611.html.

Jain, Bhuvnesh, Vinu Vikram and Jeremy Sakstein (2012). 'Astrophysical Tests of Modified Gravity: Constraints from Distance Indicators in the Nearby Universe'. In: DOI: 10.1088/0004-637X/779/1/39. URL: http://arxiv.org/abs/1204.6044http://dx.doi.org/10.1088/0004-637X/779/1/39.

Jain, Bhuvnesh et al. (2013). 'Novel Probes of Gravity and Dark Energy'. In: *arXiv e-prints*, arXiv:1309.5389, arXiv:1309.5389. arXiv: 1309.5389 [astro-ph.CO].

Jarvis, M et al. (2015). *The DES Science Verification Weak Lensing Shear Catalogues*. Tech. rep., pp. 1–37. URL: https://www.teledynedalsa.com.

Joyce, Austin et al. (2015). *Beyond the cosmological standard model*. DOI: 10.1016/j.physrep.2014.12.002.

Julio Navarro Carlos Frenk, Simon White (1995). *Simulation of X-ray clusters*. Tech. rep. Durham: Physics Departmen, Unversity of Durham, p. 21. URL: https://academic.oup.com/mnras/article-abstract/275/3/720/954770.

Kaiser, Nick (1986). 'Evolution and clustering of rich clusters'. In: *Monthly Notices of the Royal Astronomical Society* 222.2, pp. 323–345.

Khoury, Justin (2016). 'Another path for the emergence of modified galactic dynamics from dark matter superfluidity'. In: *Physical Review D* 93.10, p. 103533. ISSN: 2470-0010. DOI: 10.1103/PhysRevD.93.103533. URL: https://link.aps.org/doi/10.1103/PhysRevD.93.103533.

Khoury, Justin and Amanda Weltman (2004). *Chameleon Fields: Awaiting Surprises for Tests of Gravity in Space*. Tech. rep. URL: https://arxiv.org/pdf/astro-ph/0309300v3.pdf.

Kim Kwang Tae (1995). 'The velocity inhomogenity in the Coma cluster of galaxies'. In: *Journal of the Korean Astronomical Society*.

Kitzbichler, Manfred G. and Simon D. M. White (2006). 'The high redshift galaxy population in hierarchical galaxy formation models'. In: DOI: 10.1111/j.1365-2966.2007.11458.x. URL: http://arxiv.org/abs/astro-ph/0609636http://dx.doi.org/10.1111/j.1365-2966.2007.11458.x.

Klein, Joshua R and Aaron Roodman (2005). 'BLIND ANALYSIS IN NUCLEAR AND PARTICLE PHYSICS'. In: *Annual Review of Nuclear and Particle Science* 55.1, pp. 141–163. ISSN: 0163-8998. DOI: 10.1146/annurev.nucl.55.090704.151521. URL: http://www.annualreviews.org/doi/10.1146/annurev.nucl.55.090704.151521.

Kneib, Jean-Paul and Priyamvada Natarajan (2012). *Cluster Lenses*. Tech. rep. URL: http://www.springerlink.com/content/j183018170485723/.

Koester, BP et al. (2007). 'A MaxBCG catalog of 13,823 galaxy clusters from the sloan digital sky survey'. In: *The Astrophysical Journal* 660.1, p. 239.

Koyama, Kazuya (2016). *Cosmological Tests of Modified Gravity*. Tech. rep. URL: https://arxiv.org/pdf/1504.04623v2.pdf.

Leistedt, B et al. (2015). *Mapping and simulating systematics due to spatially-varying observing conditions in DES Science Verification data*. Tech. rep., p. 40. URL: https://github.com/emhuff/Balrog.

Lewis1, Aaron D et al. (1999). *X-RAY MASS ESTIMATES AT z D 0.3 FOR THE CANADIAN NETWORK FOR OBSERVATIONAL COSMOLOGY CLUSTER SAMPLE*. Tech. rep., pp. 587–608. URL: https://iopscience.iop.org/article/10.1086/307204/pdf.

Li, Baojiu et al. (2013). 'The non-linear matter and velocity power spectra in f(R) gravity'. In: *Monthly Notices of the Royal Astronomical Society* 428.1, pp. 743–755. ISSN: 1365-2966. DOI: 10.1093/mnras/sts072. URL: http://academic.oup.com/mnras/article/428/1/743/1060673/The-nonlinear-matter-and-velocity-power-spectra-in.

Liu, Jia, Alvaro Ortiz-Vazquez and J Colin Hill (2016). 'Constraining multiplicative bias in CFHTLenS weak lensing shear data'. In: *Physical Review D* 93.10, p. 103508.

Lloyd-Davies, E J et al. (2011). 'The XMM Cluster Survey: X-ray analysis methodology'. In: *Mon. Not. R. Astron. Soc* 418, pp. 14–53. DOI: 10.1111/j.1365-2966.2011.19117.x. URL: https://academic.oup.com/mnras/article-abstract/418/1/14/955206.

Longair, Malcolm S (2007). *Galaxy formation*. Springer Science & Business Media.

Lubini, M et al. (2011). 'Probing the dark matter issue in f (R)-gravity via gravitational lensing'. In: *Eur. Phys. J. C* 71, p. 1834. DOI: 10.1140/epjc/s10052-011-1834-8. URL: https://link.springer.com/content/pdf/10.1140/epjc/s10052-011-1834-8.

Manolopoulou, M et al. (2017). *The XMM Cluster Survey: The second XCS data release in the SDSS DR13 footprint*. Tech. rep., pp. 1–24.

Manolopoulou, Maria (2019). 'Optical and X-ray properties of galaxy clusters'. PhD thesis. University of Edinburgh.

Mantz, A. B. et al. (2014). 'Cosmology and astrophysics from relaxed galaxy clusters - II. Cosmological constraints'. In: *Monthly Notices of the Royal Astronomical Society*. ISSN: 13652966. DOI: 10.1093/mnras/stu368.

Mantz, Adam et al. (2010). 'The observed growth of massive galaxy clusters–I. Statistical methods and cosmological constraints'. In: *Monthly Notices of the Royal Astronomical Society* 406.3, pp. 1759–1772.

Massey, Richard and Alexandre Refregier (2005). 'Polar shapelets'. In: *Mon. Not. R. Astron. Soc* 363, pp. 197–210. DOI: 10.1111/j.1365-2966.2005.09453.x. URL: http://www.astro.caltech.edu/.

Maughan, BJ et al. (2012). 'Self-similar scaling and evolution in the galaxy cluster X-ray luminosity–temperature relation'. In: *Monthly Notices of the Royal Astronomical Society* 421.2, pp. 1583–1602.

Mcclintock, T et al. (2017). *Dark Energy Survey Year 1 Results: Weak Lensing Mass Calibration of redMaPPer Galaxy Clusters*. Tech. rep., p. 30. URL: https://arxiv.org/pdf/1805.00039.pdf.

Mckay, Timothy A et al. (2001). *GALAXY MASS AND LUMINOSITY SCALING LAWS DETERMINED BY WEAK GRAVITATIONAL LENSING*. Tech. rep. URL: www.sdss.org.

Mehrtens, Nicola et al. (2012). 'The XMM Cluster Survey: optical analysis methodology and the first data release'. In: *Mon. Not. R. Astron. Soc* 423, pp. 1024–1052. DOI: 10.1111/j.1365-2966.2012.20931.x. URL: https://academic.oup.com/mnras/article-abstract/423/2/1024/960476.

Mehrtens, Nicola et al. (2016). 'The XMM Cluster Survey: the halo occupation number of BOSS galaxies in X-ray clusters'. In: *MNRAS* 463, pp. 1929–1943. DOI: 10.1093/mnras/stw2119. URL: https://academic.oup.com/mnras/article-abstract/463/2/1929/2892725.

Metropolis, Nicholas et al. (1953). 'Equation of state calculations by fast computing machines'. In: *The journal of chemical physics* 21.6, pp. 1087–1092.

Mewe, R, JR Lemen and GHJ Van den Oord (1986). 'Calculated X-radiation from optically thin plasmas. VI-Improved calculations for continuum emission and approximation formulae for nonrelativistic average Gaunt factors'. In: *Astronomy and Astrophysics Supplement Series* 65, pp. 511–536.

Milkeraitis, M et al. (2018). *3D-Matched-Filter Galaxy Cluster Finder I: Selection Functions and CFHTLS Deep Clusters*. Tech. rep. 0000, pp. 0–000. URL: http://www2.cadc-ccda.hia-iha.nrc-cnrc.gc.ca/megapipe/.

Miller, L et al. (2011). *Bayesian Galaxy Shape Measurement for Weak Lensing Surveys-III. Application to the Canada-France-Hawaii Telescope Lensing Survey*. Tech. rep., p. 7. URL: www.cfhtlens.org.

Mittal, Rupal et al. (2011). 'The LX–Tvir relation in galaxy clusters: effects of radiative cooling and AGN heating'. In: *Astronomy & Astrophysics* 532, A133.

Miyazaki, Satoshi et al. (2012). 'Hyper suprime-cam'. In: *Ground-based and Airborne Instrumentation for Astronomy IV*. Vol. 8446. International Society for Optics and Photonics, 84460Z.

Miyazaki, Satoshi et al. (2015). 'Properties of Weak Lensing Clusters Detected on Hyper Suprime-Cam's 2.3 deg2 Field'. In: *The Astrophysical Journal* 807.1, p. 22.

Mohr, Joseph J et al. (2012). 'The Dark Energy Survey data processing and calibration system'. In: *Software and Cyberinfrastructure for Astronomy II*. Vol. 8451. International Society for Optics and Photonics, p. 84510D.

Moore B et al. (1998). *Resolving the Structure of Cold Dark Matter Halos*. Tech. rep. URL: https://arxiv.org/pdf/astro-ph/9709051.pdf.

Mukhanov, Viatcheslav (2005). *Physical foundations of cosmology*. Cambridge university press.

Murata, Ryoma et al. (2020). 'The splashback radius of optically selected clusters with Subaru HSC Second Public Data Release'. In: *arXiv preprint arXiv:2001.01160*.

Mushotzky, R. F. (1984). 'X-ray emission from clusters of galaxies'. In: *Physica Scripta*. ISSN: 14024896. DOI: 10.1088/0031-8949/1984/T7/036.

Nakajima, Reiko and Gary Bernstein (2007). 'Shear recovery accuracy in weak-lensing analysis with the elliptical Gauss-Laguerre method'. In: *The Astronomical Journal* 133.4, p. 1763.

Oguri, Masamune and Takashi Hamana (2011). *Detailed cluster lensing profiles at large radii and the impact on cluster weak lensing studies*. Tech. rep. URL: https://arxiv.org/pdf/1101.0650.pdf.

Oguri, Masamune and Masahiro Takada (2011). 'Combining cluster observables and stacked weak lensing to probe dark energy: Self-calibration of systematic uncertainties'. In: *Physical Review D* 83.2, p. 023008.

Oguri, Masamune et al. (2018). 'An optically-selected cluster catalog at redshift 0.1< z< 1.1 from the Hyper Suprime-Cam Subaru Strategic Program S16A data'. In: *Publications of the Astronomical Society of Japan* 70.SP1, S20.

Oyaizu, Hiroaki (2008). *Non-linear evolution of f (R) cosmologies I: methodology*. Tech. rep. URL: https://arxiv.org/pdf/0807.2449.pdf.

Pacaud, F et al. (2007). 'The XMM-LSS survey: the Class 1 cluster sample over the initial 5 deg 2 and its cosmological modelling'. In: *The Authors. Journal compilation C* 382, pp. 1289–1308. DOI: 10.1111/j.1365-2966.2007.12468.x. URL: https://academic.oup.com/mnras/article-abstract/382/3/1289/1010701.

Pacaud, F et al. (2015). *The XXL Survey , II. The bright cluster sample: catalogue and luminosity function*. Tech. rep. URL: http://cdsarc.u-strasbg.fr/viz-bin/qcat?J/A+A/vol/page.

Palmese, A et al. (2020). 'Stellar mass as a galaxy cluster mass proxy: application to the Dark Energy Survey redMaPPer clusters'. In: *Monthly Notices of the Royal Astronomical Society* 493.4, pp. 4591–4606.

Pizzuti, Lorenzo et al. (2019). 'Future constraints on the gravitational slip with the mass profiles of galaxy clusters'. In: *Monthly Notices of the Royal Astronomical Society* 486.1, pp. 596–607.

Pratt, GW et al. (2009). 'Galaxy cluster X-ray luminosity scaling relations from a representative local sample (REXCESS)'. In: *Astronomy & Astrophysics* 498.2, pp. 361–378.

Raveri, Marco et al. (2014). 'Effective Field Theory of Cosmic Acceleration: constraining dark energy with CMB data'. In: DOI: 10.1103/PhysRevD.90.043513. URL: http://arxiv.org/abs/1405.1022http://dx.doi.org/10.1103/PhysRevD.90.043513.

Rephaeli, Yoel (2011). 'Cosmology with the S-Z Effect'. In: *The Early Universe and the Cosmic Microwave Background: Theory and Observations*. DOI: 10.1007/978-94-007-1058-0{_}11.

Romer, A Kathy et al. (2000). 'A serendipitous galaxy cluster survey with XMM: expected catalogue properties and applications'. In: URL: https://arxiv.org/pdf/astro-ph/9911499v2.pdf.

Rosati, Piero, Stefano Borgani and Colin Norman (2002). 'The Evolution of X-Ray Clusters of Galaxies'. In: *Annual Review of Astronomy and Astrophysics*. ISSN: 0066-4146. DOI: 10.1146/annurev.astro.40.120401.150547.

Rykoff, E S et al. (2014). *REDMAPPER I: ALGORITHM AND SDSS DR8 CATALOG*. Tech. rep. URL: http://www.naoj.org/Projects/HSC/HSCProject.html.

Rykoff, E S et al. (2016). 'Evrard 27,28 , D. A. Finley 12 , B. Flaugher 12 , P. Fosalba 20'. In: *J. L. Marshall* 18, p. 16. ISSN: 2015-0146. DOI: 10.3847/0067-0049/224/1/1. URL: http://wfirst.gsfc.nasa.gov/.

Sahlén, Martin et al. (2009). 'The XMM Cluster Survey: forecasting cosmological and cluster scaling-relation parameter constraints'. In: *The Authors. Journal compilation C* 397, pp. 577–607. DOI: 10.1111/j.1365-2966.2009.14923.x. URL: http://xcs-home.org.

Sawicki, Ignacy et al. (2016). 'Non-standard gravitational waves imply gravitational slip: on the difficulty of partially hiding new gravitational degrees of freedom'. In: DOI: 10.1103/PhysRevD.95.083520. URL: http://arxiv.org/abs/1612.02002http://dx.doi.org/10.1103/PhysRevD.95.083520.

Schneider, Peter, Christopher Kochanek and Joachim Wambsganss (2006). *Gravitational lensing: strong, weak and micro: Saas-Fee advanced course 33*. Vol. 33. Springer Science & Business Media.

Sevilla, I. et al. (2011). 'The Dark Energy Survey Data Management System'. In: URL: http://arxiv.org/abs/1109.6741.

Sheldon, Erin S and Eric M Huff (2017). 'Practical Weak-lensing Shear Measurement with Metacalibration'. In: *The Astrophysical Journal* 841, p. 24. DOI: 10.3847/1538-4357/aa704b. URL: https://doi.org/10.3847/1538-4357/aa704b.

Sheldon, Erin Scott et al. (2001). *WEAK LENSING MEASUREMENTS OF 42 SDSS/RASS GALAXY CLUSTERS*. Tech. rep. URL: https://arxiv.org/pdf/astro-ph/0103029.pdf.

Smith, R. K. et al. (2001). 'Collisional Plasma Models with APEC/APED: Emission-Line Diagnostics of Hydrogen-like and Helium-like Ions'. In: 556, pp. L91–L95. DOI: 10.1086/322992. eprint: astro-ph/0106478.

Sotiriou, Thomas P and Valerio Faraoni (2010). 'f (R) theories of gravity'. In: *Reviews of Modern Physics* 82.1, p. 451.

Starobinsky, Alexei A. (2007). 'Disappearing cosmological constant in f(R) gravity'. In: DOI: 10.1134/S0021364007150027. URL: http://arxiv.org/abs/0706.2041http://dx.doi.org/10.1134/S0021364007150027.

Stott, J P et al. (2010). 'THE XMM CLUSTER SURVEY: THE BUILD-UP OF STELLAR MASS IN BRIGHTEST CLUSTER GALAXIES AT HIGH REDSHIFT'. In: *The Astrophysical Journal* 718, pp. 23–30. DOI: 10.1088/0004-637X/718/1/23. URL: https://iopscience.iop.org/article/10.1088/0004-637X/718/1/23/pdf.

Sunyaev, Rashid A and Ya B Zeldovich (1970). 'Small-scale fluctuations of relic radiation'. In: *Astrophysics and Space Science* 7.1, pp. 3–19.

Szabo, Thad et al. (2011). 'An optical catalog of galaxy clusters obtained from an adaptive matched filter finder applied to sloan digital sky survey data release 6'. In: *The Astrophysical Journal* 736.1, p. 21.

Tamosiunas, Andrius et al. (2019). *Testing Emergent Gravity on Galaxy Cluster Scales*. Tech. rep. URL: https://arxiv.org/pdf/1901.05505.pdf.

Terukina, Ayumu and Kazuhiro Yamamoto (2012). *Gas density profile in dark matter halo in chameleon cosmology*. Tech. rep. URL: https://arxiv.org/pdf/1203.6163.pdf.

Terukina, Ayumu et al. (2014). *Testing chameleon gravity with the Coma cluster*. Tech. rep. URL: https://arxiv.org/pdf/1312.5083v2.pdf.

Thomas, Peter A et al. (1998). 'The structure of galaxy clusters in various cosmologies'. In: *Monthly Notices of the Royal Astronomical Society* 296.4, pp. 1061–1071.

Tozzi, Paolo (2007). 'Cosmological parameters from galaxy clusters: An introduction'. In: *Lecture Notes in Physics*. ISSN: 00758450. DOI: 10.1007/978-3-540-71013-4{_}5.

Verlinde, Erik P. (2016). 'Emergent Gravity and the Dark Universe'. In: DOI: 10.21468/SciPostPhys.2.3.016. URL: http://arxiv.org/abs/1611.02269http://dx.doi.org/10.21468/SciPostPhys.2.3.016.

Vikhlinin, A et al. (2003). *COSMOLOGICAL CONSTRAINTS FROM EVOLUTION OF CLUSTER BARYON MASS FUNCTION AT Z 0.5*. Tech. rep. URL: https://arxiv.org/pdf/astro-ph/0212075.pdf.

Vikhlinin, A. et al. (2009). 'Chandra cluster cosmology project III: Cosmological parameter constraints'. In: *Astrophysical Journal*. ISSN: 15384357. DOI: 10.1088/0004-637X/692/2/1060.

Voevodkin, A and A Vikhlinin (2003). *CONSTRAINING AMPLITUDE AND SLOPE OF THE MASS FLUCTUATION SPECTRUM USING CLUSTER BARYON MASS FUNCTION*. Tech. rep. URL: https://arxiv.org/pdf/astro-ph/0305549.pdf.

Voit, G Mark (2004). *Tracing cosmic evolution with clusters of galaxies*. Tech. rep.

Wambsganss, Joachim (1998). 'Gravitational Lensing in Astronomy Living Reviews in Relativity Article Revisions'. In: *Gravitational Lensing in Astronomy* 1, p. 12. DOI: 10.1007/lrr-1998-12. URL: http://www.livingreviews.org.

Weinberg, David H. et al. (2013). *Observational probes of cosmic acceleration*. DOI: 10.1016/j.physrep.2013.05.001.

Wen, ZL, JL Han and FS Liu (2012). 'A catalog of 132,684 clusters of galaxies identified from Sloan Digital Sky Survey III'. In: *The Astrophysical Journal Supplement Series* 199.2, p. 34.

White, Simon DM et al. (1993). 'The baryon content of galaxy clusters: a challenge to cosmological orthodoxy'. In: *nature* 366.6454, p. 429.

Wilcox, Harry et al. (2015). 'The XMM cluster survey: Testing chameleon gravity using the profiles of clusters'. In: *Monthly Notices of the Royal Astronomical Society* 452.2, pp. 1171–1183. ISSN: 13652966. DOI: 10.1093/mnras/stv1366.

Wilcox, Harry et al. (2018). *Simulation tests of galaxy cluster constraints on chameleon gravity*. Tech. rep. 0000, pp. 0–000. URL: http://enzo-project.org/.

Will, Clifford M (2006). *The Confrontation between General Relativity and Experiment*. Tech. rep. URL: http://wugrav.wustl.edu/People/CLIFF/index.html.

Wright, Candace Oaxaca and Tereasa G. Brainerd (1999). 'Gravitational Lensing by NFW Halos'. In: URL: http://arxiv.org/abs/astro-ph/9908213.

XMM-Newton Community Support Team (2018). 'XMM-Newton Users Handbook'. In: URL: http://xmm-tools.cosmos.esa.int/external/xmm_user_support/documentation/uhb/XMM_UHB.pdf.

York, Donald G et al. (2000). 'The sloan digital sky survey: Technical summary'. In: *The Astronomical Journal* 120.3, p. 1579.

Zenteno, A et al. (2020). 'A joint SZ–X-ray–optical analysis of the dynamical state of 288 massive galaxy clusters'. In: *Monthly Notices of the Royal Astronomical Society* 495.1, pp. 705–725.

Zhang, Y-Y et al. (2008). 'LoCuSS: comparison of observed X-ray and lensing galaxy cluster scaling relations with simulations'. In: *Astronomy & Astrophysics* 482.2, pp. 451–472.

Zhang, Yuanyuan et al. (2019a). 'Dark Energy Surveyed Year 1 results: calibration of cluster mis-centring in the redMaPPer catalogues'. In: *Monthly Notices of the Royal Astronomical Society* 487.2, pp. 2578–2593.

Zhang, Yuanyuan et al. (2019b). 'Galaxies in X-ray selected clusters and groups in Dark Energy Survey data–II. Hierarchical Bayesian modelling of the red-sequence galaxy luminosity function'. In: *Monthly Notices of the Royal Astronomical Society* 488.1, pp. 1–17.

Zuhone, J A and J Sims (2019). *TESTING EMERGENT GRAVITY WITH OPTICAL, X-RAY, AND WEAK LENSING MEASUREMENTS IN MASSIVE, RELAXED GALAXY CLUSTERS*. Tech. rep. URL: https://arxiv.org/pdf/1905.03832.pdf.

Zuntz, Joe et al. (2018a). 'Dark Energy Survey Year 1 results: weak lensing shape catalogues'. In: *Monthly Notices of the Royal Astronomical Society* 481.1, pp. 1149–1182.

Zuntz, Joe et al. (2018b). *IM3SHAPE: A maximum-likelihood galaxy shear measurement code for cosmic gravitational lensing*. Tech. rep. 0000, pp. 0–000. URL: http://www.darkenergysurvey.org.